

Time Resolved Imaging Calorimetry

Dissertation

zur Erlangung des Doktorgrades

des Fachbereichs Physik

der Universität Hamburg

vorgelegt von

Sebastian Piet Laurien

aus Hamburg

Hamburg

2018

Gutachter der Dissertation:

Prof. Dr. Erika Garutti
Dr. Katja Krüger

Datum der Disputation:

06. September 2018

Vorsitzender des Prüfungsausschusses:

Prof. Dr. Dieter Horns

Dekan der Fakultät für Mathematik,
Informatik und Naturwissenschaften:

Prof. Dr. Heinrich Graener

For Karl

Abstract

Excellent detectors are needed for a future lepton collider like the international linear collider project (ILC) to exploit their full physics potential. Within the CALICE collaboration, several concepts based on the particle flow reconstruction approach for the hadronic calorimeter are studied. The prototype designs offer unmet spacial resolution as well as the option for hit time reconstruction in the ps regime. After having demonstrated the capabilities of the measurement methods in physics prototypes, the focus now lies on improving their implementation in engineering prototypes, that are scalable to the full linear collider detector. The Analog Hadron Calorimeter (AHCAL) concept is a sampling calorimeter of tungsten or steel absorber plates and plastic scintillator tiles read out by silicon photo-multipliers (SiPMs) as active material. The front- end chips are integrated into the active layers of the calorimeter and are allowing the prototype to be equipped with different types of scintillator tiles as well as SiPMs.

The first part of this thesis covers the development of a new readout option with scintillating tile and novel SiPMs. Four layers with 576 units each, have been equipped with a novel design of scintillator tile. The development and detailed characterization of this new design as well as a first approach to a mass characterization of hundreds of detection units is presented. Different operation modes are discussed based on the results from the characterization and test beams. The most promising modus of operation is presented.

The second part of this thesis focuses on the time resolution capabilities of the Spiroc2b readout chip to measure the hit time of a signal. The hit time reconstruction in the ns range offers new opportunities to validate and improve current simulations of the development of hadronic showers. The focus lies on the hit time reconstruction and the highest possible time resolution achievable. The calibration strategy to achieve the highest possible resolution with the Spiroc2b chip is presented. Test beam data from different test beams with electrons and 50 GeV pions and 180 GeV pions of an prototype version of one AHCAL layer with the Spiroc2b readout chip is analyzed. The results provide insight into the time structure of hadronic showers which are compared to Geant4 simulations with different physics list.

Zusammenfassung

Für einen zukünftigen Leptonen Kollider wie den International Linear Collider (ILC) werden Detektoren mit exzellenter Auflösung benötigt, um das gesamte physikalische Potential der Maschine ausschöpfen zu können. Im Rahmen der CALICE Kollaboration werden verschiedene Konzepte, basierend auf dem Particle Flow Rekonstruktionsansatz für das hadronische Kalorimeter untersucht. Die verschiedenen Prototypen der hadronischen Kalorimeter bieten eine bisher unerreichte räumliche Auflösung sowie die Möglichkeit der Rekonstruktion der Trefferzeit im ps Regime. Nachdem die Fähigkeiten des Particle Flow Ansatzes mit mehreren Prototypen validiert wurden, liegt der Fokus der Entwicklung nun auf der Verbesserung der Detektionseinheiten und ihrer Implementierung in technische Prototypen, die auf ein vollständiges HCAL für einen Detektor am ILC skaliert werden können. Das AHCAL Konzept (Analog Hadron Calorimeter) ist ein hadronisches Kalorimeter mit Absorberplatten aus Wolfram oder Stahl und Kunststoffszintillatorkacheln, die von Silizium-Photomultipliern (SiPMs) ausgelesen werden als aktives Medium. Die Front-End-Chips sind in die aktiven Schichten des Kalorimeters integriert und ermöglichen die Ausstattung des Prototyps mit verschiedenen Arten von Szintillatorkacheln und SiPMs. Der erste Teil dieser Arbeit behandelt die Entwicklung einer neuen Option von Ausleseeinheiten aus Scintillatorkachel und SiPM. Vier Lagen des neuesten AHCAL Prototypen wurden mit einem neuartigen Design der Universität Hamburg ausgestattet. Die Entwicklung und detaillierte Charakterisierung dieses neuen Designs werden beschrieben. Ein Messaufbau zur Massencharakterisierung von Hunderten von Detektionseinheiten wird vorgestellt. Basierend auf den Ergebnissen der Charakterisierung werden verschiedene Betriebsmodi diskutiert und der vielversprechendste Betriebsmodus wird ermittelt.

Der zweite Teil dieser Arbeit beschäftigt sich mit den Fähigkeiten der Zeitmessung des Spiroc2b Auslesechips. Die Rekonstruktion der Trefferzeit im ns Bereich bietet neue Möglichkeiten, Simulationen der räumlichen und Zeitlichen Entwicklung hadronischer Schauer zu validieren und zu verbessern. Der Fokus dieser Arbeit liegt auf der Rekonstruktion der Trefferzeit und der höchstmöglichen erreichbaren Zeitauflösung. Eine Kalibrierungsstrategie, die alle bekannten Effekte des Spiroc2b berücksichtigt, wird vorgestellt. In verschiedenen Teststrahlen mit Elektronen am DESY und 50 GeV und 180 GeV Pionen am CERN wurden Daten mit einer Lage des Prototypen der neuen Ausleseoption mit 567 Kanälen genommen. Die Analyse der Daten ermöglicht Einblicke in die Zeitstruktur hadronischer Schauer. Die Daten werden mit Geant4 Simulationen, basierend auf unterschiedlichen Physiklisten, verglichen und bewertet.

Contents

Abstract	iv
Zusammenfassung	v
	Page
1 Introduction	1
2 The Physics at ILC	5
2.1 Lepton colliders	5
2.2 International Linear Collider - ILC	6
2.3 Physics Program at the ILC	7
2.3.1 Higgs Boson	8
3 Hadronic interaction and Calorimetry	11
3.1 Particle Interaction with Matter	11
3.1.1 Electromagnetic Showers	12
3.1.2 Heavy Charged Particle Interaction	14
3.1.3 Muon Interaction	15
3.1.4 Hadronic Showers	16
3.1.5 Time development of Hadronic Showers	18
3.2 Calorimetry	20
3.2.1 Sampling Calorimeter	20
4 Photon detection	23
4.1 Detection media for Hadronic Calorimeters	23
4.2 Photomultiplier tube (PMT)	24
4.3 Photodiode	25
4.4 Avalanche Photo-diode (APD)	25
4.5 Geiger mode APD	26
4.6 SiPM	27
4.6.1 SiPM characterization parameters	28

5	Particle Flow	31
5.1	Particle physics detectors	32
5.2	Particle Flow Algorithm	34
5.3	The ILD detector	35
5.4	Spacial optimization for an ILD HCAL	38
6	Analogue Hadronic Calorimeter (AHCAL) Technology	39
6.1	Mechanical structure of the ILD barrel	40
6.2	HCAL base unit (HBU)	41
6.3	Readout ASIC - Spiroc2b	41
6.3.1	Internal adjustment of SiPM bias voltage	43
6.3.2	Trigger	43
6.3.3	Energy measurement	44
6.3.4	Time measurement	45
6.3.5	Readout of the analogue memory cells	45
6.4	SiPM and Scintillator system	46
6.4.1	SiPM	47
6.4.2	Scintillator	47
6.4.3	Wrapping	47
7	Tile and SiPM system of the University Hamburg	49
7.1	Mass testing setup	49
7.1.1	SiPM measurements	50
7.1.2	Tile response measurement	54
7.1.3	Optical crosstalk measurement	58
7.2	SiPM for Production	59
7.3	Characterization of Scintillating Materials	60
7.3.1	Temperature dependency of the detector after calibration	65
7.4	Wrapping and Surface Treatment of Scintillating Tiles	66
7.4.1	Photon containment in scintillating Tiles	66
7.4.2	Comparison of wrapping / coating alternatives	67
8	SiPM voltage adjustment with the Spiroc2b	69
8.1	Functionality and Precision of the Power Board	70
8.2	Spiroc2b internal voltage adjustment	72
8.2.1	Unstable channel	73
8.2.2	Voltage stability	73
8.2.3	Single channel calibration	73
8.3	Detector calibration and precision	77

9	Commissioning and Calibration Validation at the DESY II Test Beam	79
10	Operation Voltage Optimization	83
10.1	Spiroc2b restrictions on the operational parameters	85
10.2	Methodology of the Optimization	85
10.3	Optimizing strategies for setting the bias voltage	85
10.4	Optimization with fixed voltage (I)	87
10.4.1	MIP efficiency	88
10.4.2	Noise over threshold	89
10.5	Operational parameters for 18 px per MIP response	91
11	Time measurement with the Spiroc2b	93
11.1	Hit timing measurement in the Spiroc2b	95
11.2	TDC calibration	98
11.2.1	Ramp extraction $f_{i,j}$	99
11.2.2	Memory-cell Offset $P_{i,j,k}^{off}$	102
11.2.3	Time slew correction	106
11.2.4	Trigger per chip dependency $P_S^{TDC}(N)$	107
11.2.5	Trigger surge	108
11.2.6	Summary TDC calibration	109
12	Hit time measurement in a Hadron Test Beam	111
12.1	Setup of the Detector in the SPS Area	111
12.1.1	The W-DHCAL main detector	111
12.1.2	One layer setup and data taking	112
12.2	Geant4 Simulations of the Test Beam	114
12.2.1	Energy calibration	116
12.3	Validation of Timing Calibration with Muons	119
12.3.1	Validation of $P_S^{TDC}(N)$	119
12.4	Response to Pions	121
12.4.1	180 GeV pions	122
12.4.2	50 GeV pions	123
12.4.3	Radial Hit Time Dependency	125
13	Conclusion	127
	Bibliography	130
	Acknowledgements	139

Chapter 1

Introduction

The standard model of particle physics ([1], [2], [3]) has for the better part of a century been the most successful model to describe the physical world of quantum physics. It is a relativistic quantum field theory with local gauge invariance described in a unitary product group $SU(3) \times SU(2) \times U(1)$. Though it has continual success in experimental predictions with high precision, it cannot explain all observed phenomena in physics and fundamental proven concepts like general relativity and gravitation. It can also only explain about 5% of the energy content in the universe. Around $\frac{1}{4}$ of the universe is dark matter [4] that has been first measured by observing the rotation of galaxies in 1933 [5], whilst the remaining energies is attributed to dark energy [6] by observing e.g. the cosmic microwave background [7]. It is therefore considered an effective field theory providing excellent predictions in a broad range of energies. The SM is usually represented as the Lagrangian density function consisting of four quantum fields. The quantum fields are the fermion fields ψ accounting for matter particles (leptons and quarks), the electroweak boson fields (W_1, W_2, W_3 , and B), the gluon field G_a , and the Higgs boson field φ . The massless electroweak bosons acquire mass through the Higgs mechanism caused by spontaneous electroweak symmetry breaking. The W_1 and W_2 fields mix to form the charged W^\pm bosons and the W_3 and B field mix to form the neutral Z^0 boson and the massless photon (γ). Following Wigner's classification [8] particles are irreducible unitary representations of the Poincaré group, which have sharp mass eigenvalues of non negative energy. Those particles are called elementary particles. The SM consists of leptons, quarks in three generations, gauge bosons and the Higgs boson. Figure 1.1 shows the known particles in the so called particle zoo. Every particle also has its antiparticle. Fermions are the known particles with rest mass (mediated by the Higgs boson) of which matter consists of. The gauge bosons mediate the electroweak and strong interactions between particles. Figure 1.2 summarizes the forces and their relations within the SM. Photons (γ) mediate the electromagnetic force between charged particles as described in quantum electrodynamics. The weak interactions are mediated by the W^\pm and Z^0 bosons between all leptons and quarks and is responsible for radioactive decay. The strong force is mediated by gluons acting on quarks

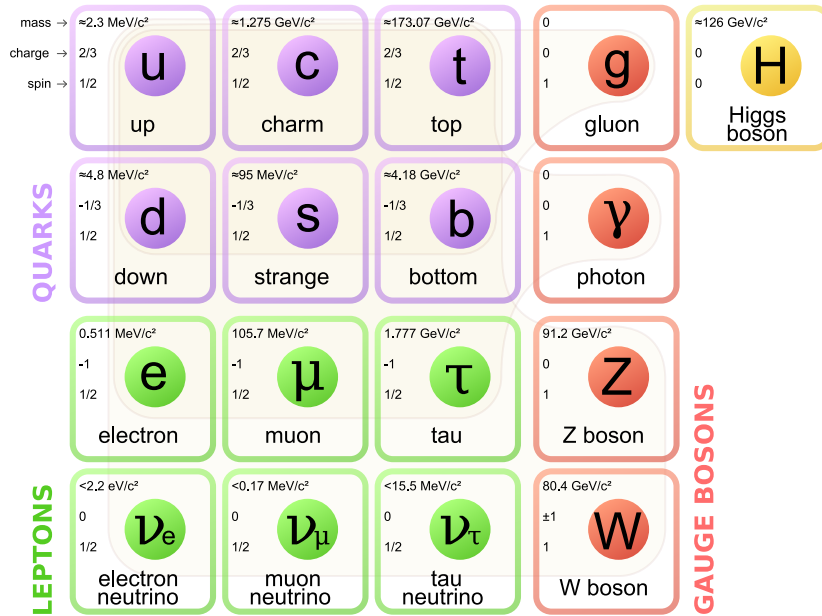


Figure 1.1: The Standard Model (SM) of particle physics
 leptons and quarks exist in three generations with increasing mass and declining half life time. The fourth column are gauge bosons that mediate the forces of the standard model (relations see Figure 1.2) and the Higgs boson in the fifth column that gives fermions and the W[±] and Z⁰ their rest mass.
 figure by MissMJ / CC BY

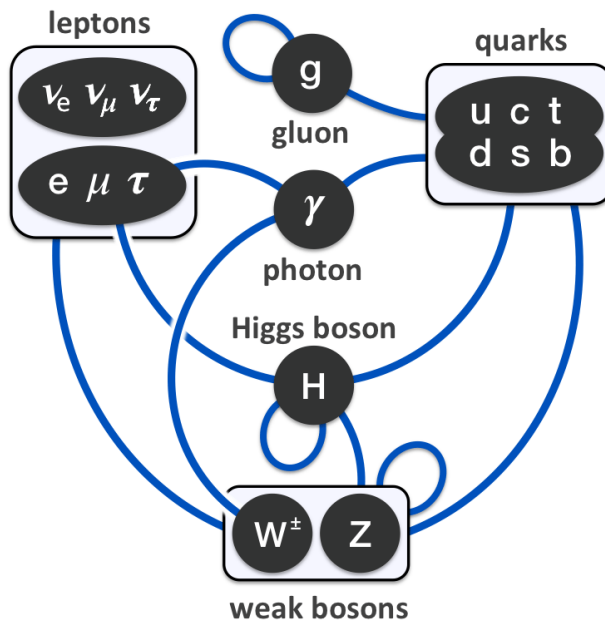


Figure 1.2: The forces and their relation of the standard model.
 Figure by MissMJ / CC BY

and gluons themselves and is responsible for the formation of composite matter like protons

and neutrons. Particle physics accelerators are the experimental method of choice to test the predictions of the standard model. They provide a controlled initial state with high energies necessary to test the regimes of the standard model and beyond. Through predicted but sometimes also surprising discoveries, the SM has been validated and extended to describe the physical world at high precision. The Large Hadron Collider (LHC) at CERN is the world's largest accelerator with collision energies up to 13 TeV. Apart from validating and measuring SM model properties with unmet precision and extending exclusion threshold for theoretical models, the biggest success so far was the recent discovery of the Higgs boson [9], [10] and many of its properties in 2012 that were predicted over 40 years ago [11], completing the SM by discovering the last predicted particle of the theory.

One of the main goals of the next years will be to fully measure all properties of the Higgs boson, like quantum numbers and specifically couplings to fundamental particles and self-coupling. Those properties are predicted with high accuracy in the standard model and precision measurements will enable the validation of the standard model or open up new fields of research.

The next steps to test those properties with unprecedented precision is a to the LHC complementary lepton collider with clearly defined initial states [12]. The reduced background and defined initial states of a lepton collision with elementary particles instead of composite particles like protons at the LHC will enable model independent determination of Higgs boson parameters [13]. The proposed international Linear Collider (ILC) is a $e^+ e^-$ collider with energies up to 250 GeV to 500 GeV center of mass energy. To exploit the full potential of such a machine, the detectors need to have an excellent resolution. They need to be capable of reconstructing the complete event structure and particle jet energies with great precision. One of the goals of the detector development is to achieve a hadronic jet resolution of $\frac{0.3}{\sqrt{E(\text{GeV})}}$. This target resolution cannot be achieved by a conventional feasible detector structure. A new approach to measuring particles and subcomponents of hadronic jets is the particle flow algorithm (PFA, Chapter 5). PFA imposes new requirements to the detector like being able to track single particles of a hadronic jet throughout the detector. This requires an unmet imaging capability in spacial resolution and new detector designs especially for the calorimeter system.

The CALICE collaboration [14] is developing particle flow calorimeters for the ILC and similar lepton colliders. Among different prototypes is the analogue hadronic calorimeter that tests several readout concepts based on plastic scintillator read out by silicon photo multipliers (SiPMs). To prove the concept and feasibility of an imaging calorimeter, a 1 m^3 prototype has been commissioned and tested in test beam campaigns from 2009-2012. The focus of the AHCAL research now lies on fully scalable designs for prototypes to fulfill all requirements for an ILC HCAL. This thesis is structured in two parts and the first part focuses on the development of the design of those cells. The design is driven by a detailed characterization

of the current detector readout chip Spiroc2b, see Chapter 6 through 10.

Another focus of the CALICE collaboration is to provide detailed shower data for validation and improvement of the simulation of hadronic showers in particle physics simulations with Geant4. Current hadronic shower models deviate especially in the prediction of timing inside the hadronic showers. During test beam campaigns at different accelerators, data with high spacial resolution became available. The time resolved simulation of particle showers can be validated now with time resolved imaging calorimetry. This opens a new way of simulation comparison as well as detector operation in high background environments. This is particularly interesting for future projects like the Compact Linear Collider (CLIC) with a high pile up and high collision rate where hadronic showers in the calorimeter will overlap.

Part two of this thesis focuses on the exploitation of the timing capabilities of the Spiroc2b to compare hadronic shower data with physics simulations. First the capabilities of the timing section of the Spiroc2b are evaluated for 4D hadronic calorimetry. Chapter 11 focuses on a possible calibration scheme for the time to digital converter of the Spiroc2b and Chapter 12 validates the achieved resolution in test beam at the CERN SPS with muons. Chapter 12 analysis pion data taken at 50 GeV and 180 GeV. The result is compared to different Geant4 simulations.

Chapter 2

The Physics at ILC

Many different physics processes make the ILC a compelling machine to study the standard model and extension to it in detail. The impressive amount of possible measurements are shown e.g. in the ILC technical design report (TDR, [15] and [13]). In this Chapter a quick illustration of the accelerator concept of the ILC will be presented, followed by a selection of possible physics cases in light of the recent discovery of the Higgs boson.

2.1 Lepton colliders

The LHC is up to date with a design center of mass energy of 14 TeV, the most powerful accelerator build. Searches for new particles at high energies and the long expected Higgs were a main motivation for the design of this machine. Hadrons are relatively easy to accelerate to high energies due to their high rest mass (compared to leptons). Synchrotron radiation limits the collision energy that can be achieved by a ring accelerator like the LHC. The radiation losses,

$$P_{sync} \propto \frac{E^4}{r \cdot m^4} \quad (2.1)$$

scale in the forth power of the achieved energy E depending on the mass of the accelerated particles m and the radius of the ring r . Lepton masses are three orders of magnitude lower than hadron masses, therefore the radiation losses are significantly higher in a ring accelerator. The predecessor of the LHC was the LEP (**L**arge **E**lectron - **P**ositron collider, [16]) at CERN with a circumference of 27 km and a maximum center of mass energy of 209 GeV. Due to the composite nature of hadrons, a well defined initial state of the collisions cannot be achieved. Unknown is the exact energy or identity of the colliding quarks as constituents of the accelerated hadron, and other parameters like their spin orientation. By colliding leptons instead of hadrons those shortcomings can be overcome with a collision of elementary particles that have well defined parameters, since the initial state of the colliding leptons is known from machine parameters. Polarized beams would provide an amount of control over

the spin orientation prior to collision. An $e^+ e^-$ collider is therefore the logical follow-up project for precision measurements of the discoveries made at the LHC. The next lepton accelerators will therefore most likely be linear accelerators in the TeV region. The most advanced project is the international linear accelerator (ILC). The Japanese government is considering hosting the ILC in northern Japan.

2.2 International Linear Collider - ILC

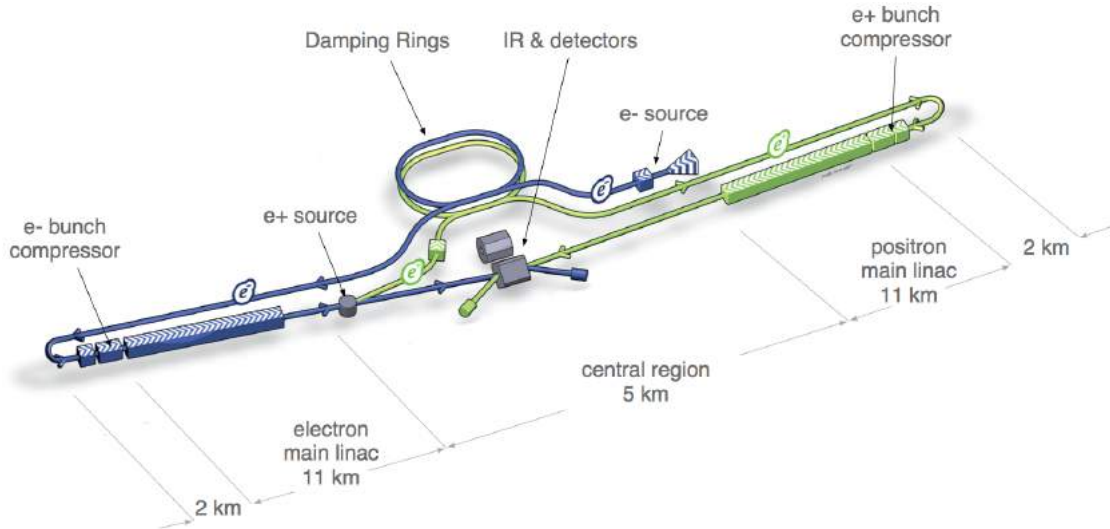


Figure 2.1: ILC Layout (not to scale) [15]

Figure 2.1 shows the planned layout for the ILC. The electron positron collider has a center of mass energy of 500 GeV with a possible upgrade to 1 TeV designed to have a luminosity of $1.8 \times 10^{34} \text{ cm}^{-2} \text{ s}^{-1}$ at 500 GeV. Polarized electrons generated via a laser in the electron source are accelerated to 5 GeV and accumulated to a full ILC bunch train in the damping ring. The main acceleration process starts in the main linear accelerator (linac) after reorienting the beam and bunch compression in the beam delivery system. The main linac consists of up to 16000 cryo modules (Figure 2.3), depending on the final design of the ILC. The main part of the accelerator components are the superconducting niob cavities. This well established technology is already in use at the X-Ray laser facilities FLASH and XFEL at DESY. A gradient of $31 \frac{\text{MeV}}{\text{m}}$ accelerates the electron to their final energy. Part of the beam is guided through an undulator to emit photons. Pair production on a target produces positrons that are fed into a separate damping ring. Through a similar set of components, they are accelerated to their final energy and brought to collision with the electron beam in the detector area. The ILC is expected to collect in integrated luminosity of 500 fb^{-1} at 500 GeV, 200 fb^{-1} at 350 GeV, and 500 fb^{-1} at 250 GeV. Luminosity upgrades are foreseeable for the future as well. As can be seen in Figure 2.2, every 200 ms a bunch train is produced. Each train consists

- **Time Structure: 5 Bunch-trains per second**

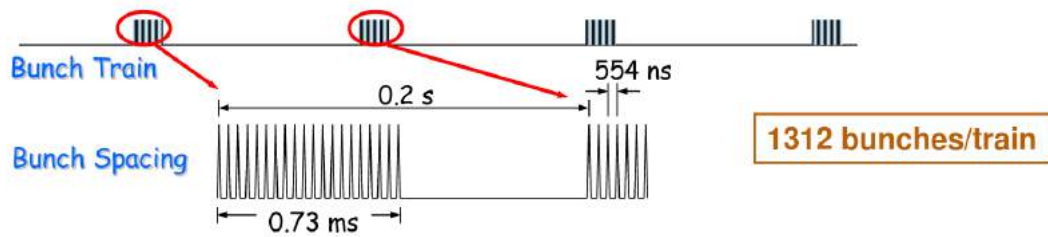


Figure 2.2: ILC Bunch structure [15].

of 1312 bunches with 554 ns spacing. This beam structure is owed to the operation mode of the super conduction cavities. The challenges for the detectors are given by the short spacing between collision and the long dead time between the trains. Two detectors at the collision point will operate in a push pull operation allowing for maintenance of one detector while the other takes data. The detectors are the SiD (All Silicon Detector, [15]) and the ILD which is described in more detail in Chapter 5.



Figure 2.3: ILC cryo module with superconducting cavity. ©Rey.Hori/KEK

2.3 Physics Program at the ILC

All decay modes of heavy particles that are studied at the ILC can be observed with errors on the permille level. Event selection at the ILC will yield high purity over background. The main topics for research at the ILC will be the complete characterization of the newly discovered Higgs boson with high precision and top quark properties.

2.3.1 Higgs Boson

Before the theoretical integration by Steven Weinberg and Abdus Salam [17] of the Higgs mechanism into the SM, particles within the SM showed no rest mass. In its simplest form, the Higgs mechanism introduces a new quantum field ϕ to the SM. Below an extremely high temperature the field causes spontaneous symmetry breaking during interactions. After symmetry breaking ($SU(3) \times SU(2) \times U(1) \rightarrow SU(3) \times U(1)$) three components (out of four) of the Higgs field mix with the gauge bosons W^\pm and Z^0 that acquire rest mass. The unbroken part of the symmetry is represented by γ that remains massless. Through a Yukawa mechanism [18] with unknown (and therefore to be experimentally measured) couplings, the chiral gauge invariance of the Lagrangian is restored. This results in the coupling to fermions and they acquire mass proportional to the vacuum expectation value of the Higgs field. With an precise estimate on the Higgs mass, all further parameters of the Higgs boson are fixed within the Standard model within uncertainties. Any observation deviating from those predictions is an indicator of Physics beyond the standard model. Deviation from the Higgs coupling to other particles (see Figure 1.2 in Chapter 1) and the nature of the deviation, hint towards different theories like composite Higgs or super symmetric extension to the standard model. Not all decay channels can be observed at the LHC and only a lepton collider will be able to measure all decay channels down to the percent level. Figure 2.4 shows the main Higgs

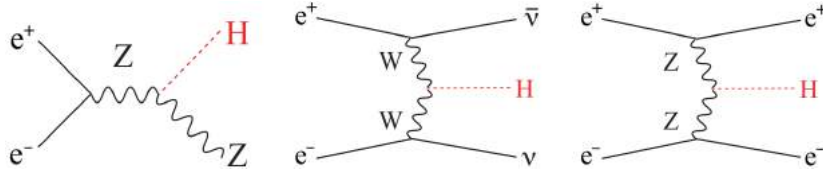


Figure 2.4: Feynman diagrams of the main Higgs production processes at ILC. Higgs strahlung $e^+e^- \rightarrow ZH$ (left), WW -fusion $e^+e^- \rightarrow \nu\bar{\nu}H$ in the middle, and ZZ -fusion $e^+e^- \rightarrow e^+e^-H$ on the right. [19]

production processes at ILC. The Higgs decays to Z^0Z^0 and $W^\pm W^\pm$ have been measured at LHC at their SM predictions. The proposed running in several stages and the possibility to polarize the beams of the ILC will access the different production modes at different cross-sections as can be seen in Figure 2.5. It enables detailed measurements for the different modes. The known initial state at ILC allows for a measurement of the inclusive cross section of $e^+e^- \rightarrow Z^0H$. The measurement of the Z^0 decay to two leptons $Z^0 \rightarrow l^+l^-$ is the most precise way to reconstruct the invariant Higgs mass (M_X) to around 30 MeV precision. The only constraint is to find two leptons with the Z^0 mass. This leads to the coupling g_{HZZ} of the Higgs to Z^0 and can be calculated exactly without model dependency. This measurement can be performed already at a center of mass energy of 250 GeV at the ILC. The coupling to the W^\pm can be measured indirectly model independent through $e^-e^+ \rightarrow \nu\bar{\nu}H$. The neutrinos cannot be detected so a decay mode with a high branching ratio into measurable particles like $e^-e^+ \rightarrow \nu\bar{\nu}H \rightarrow \nu\bar{\nu}b\bar{b}$ can indirectly measure the decay. The Higgs self coupling λHHH

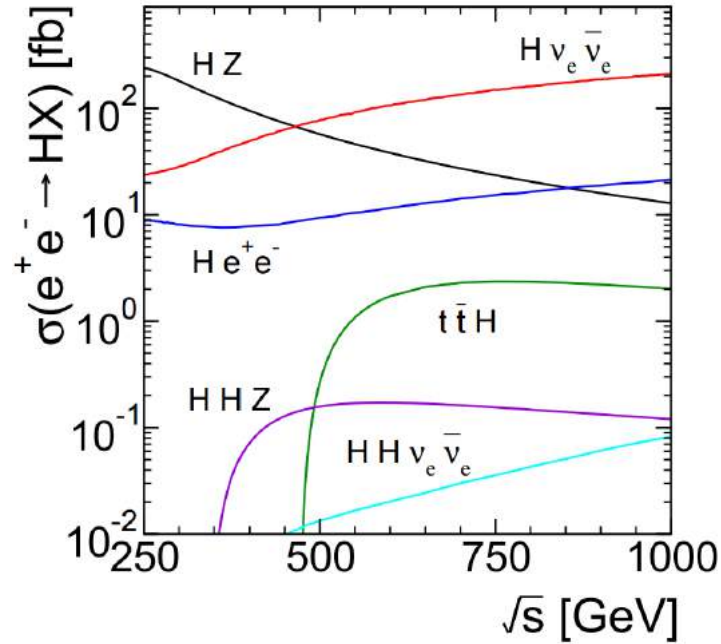


Figure 2.5: Cross section of Higgs production processes at the ILC as a function of the center of mass energy of the collision. The advantage of threshold scanning for different production modes and detailed measurements at different energies for a staged ILC is apparent. The measurement of rare processes motivated the planned ILC update to 1 TeV. Note the logarithmic scale. [20]

can be determined via $e^+e^- \rightarrow \nu\bar{\nu}HH$ and $e^+e^- \rightarrow Z^0HH$, which have a rather small cross section as can be seen in Figure 2.5 and lead to a more challenging analysis. Figure 2.6 shows the projected precision on the Higgs couplings for a model dependent fit. The projection does not only include the two stages of the planned ILC, but also a planned upgrade of the LHC to the High Luminosity LHC (HL-LHC). As a hadron collider, the LHC cannot access all Higgs coupling modes independent so for the comparison this Figure is for model dependent coupling estimates only (SM is assumed without any additional decays that would hint to super symmetry or similar). The ILC can measure coupling independently of the model, making a correct selection between different extensions to the SM more precise. The light green and dark green bar show the best and worse estimations from a CMS study for the projected HL-LHC published in [21]. The staged running of the ILC in red and yellow shows the increased precision with which the Higgs coupling could be measured. The decay $H \rightarrow \gamma\gamma$ is a rare process at the ILC and thus the combination plot from HL-LHC and ILC is shown. In summary the ILC in combination with a HL-LHC could measure the Higgs boson couplings to precision under 1% for most channels. It will make distinguishing different Higgs models possible.

Other research areas will be the search for new particles and dark matter candidates that are predicted in many super symmetric models. They have small masses under 20 GeV which is under the detection threshold for the LHC due to the hadronic background. Top quark strong

and electroweak couplings can also be measured with high precision. The ILC will extend and complement the measurements done by LHC and a possible HL-LHC upgrade to exclude or proof different Extensions to the SM that could open completely new fields of physics in the future.

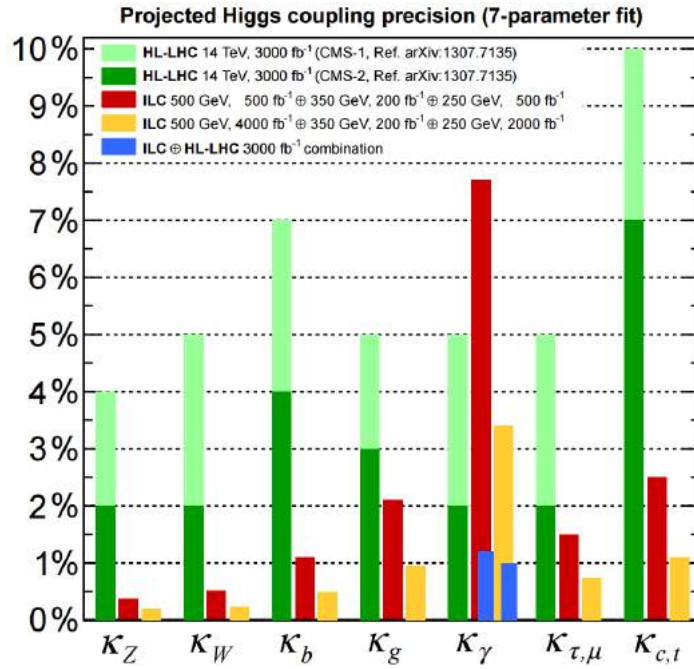


Figure 2.6: Precision prediction for different stages of the ILC compared to a HL-LHC (CMS worst and best case scenarios). In red the projection for the first stage running of the ILC and in yellow the dataset from the second stage. In blue the combination plot for HL-LHC and ILC. [22]

Chapter 3

Hadronic interaction and Calorimetry

For the understanding of the Particle Flow Method, first an introduction to standard calorimetry and the relevant processes for the development of hadronic showers is given. Calorimeters have historically provided the measurement of the energy of an object by heat transfer. In Particle Physics it refers to the measurement of the energy of a single particle or atomic object. The particle must (in most measurements in calorimetry) come to a complete stop and deposit its kinetic energy in a measurable way into the detector. Particle physics calorimeters are therefore dense objects. The transferred heat or recoil of a single particle is too small to be measured. The energy is characterized by measuring deposited energies from secondary particles instead. They are produced on impact with the detector and interact via different physics processes. The first part of this Chapter focuses on the electromagnetic (3.1.1) and hadronic (3.1.4) interactions of particles with matter. The time development of processes occurring in a calorimeter are discussed in 3.1.5. Design and functionality of calorimeters in particle physics, especially sampling calorimeters are described in 3.2.

3.1 Particle Interaction with Matter

Interactions of matter depend on the particle type. Especially hadrons can undergo a variety of different processes to lose their kinetic energy. Of the variety of particles produced in a particle collision in an accelerator only $(e^\pm, \mu^\pm, \gamma, \pi^\pm, K^0, K^\pm, p^\pm, n, \nu)$ ever reach the detector. Muons (μ) pass matter mostly without producing showers. Neutrinos (ν) almost never interact with matter and generate no signals in the detectors. The rest can be divided into two groups: firstly, $(e^\pm$ and $\gamma)$ which induce electromagnetic showers through the electromagnetic force and secondly $(\pi^\pm, K^0, K^\pm, p^\pm, n)$ which induce hadronic showers. Most detectable signals are left by charged particles. Electromagnetic interactions produce dense showers in matter undergoing only a few processes. Hadronic interaction undergoes more complex struc-

ture and processes including electromagnetic interaction which is therefore described first in the next section.

3.1.1 Electromagnetic Showers

Figure 3.1 shows the different processes leading to energy loss of an electron or positron passing through matter. High energy electrons lose their energy almost exclusively to Bremsstrahlung. The charged particle interacts with the Coulomb field of nuclei and radiates photons. The other dominant process is energy loss by ionization of the atoms of the medium. The radiation length X_0 is defined as the mean distance over which an electron loses $\frac{1}{e}$ of its energy via Bremsstrahlung and approximated with

$$X_0 \approx 180 \frac{A}{Z^2} \left[\frac{g}{\text{cm}^2} \right]. \quad (3.1)$$

Divided by the density of the material X_0 can also be expressed in cm. The critical energy ϵ_c is

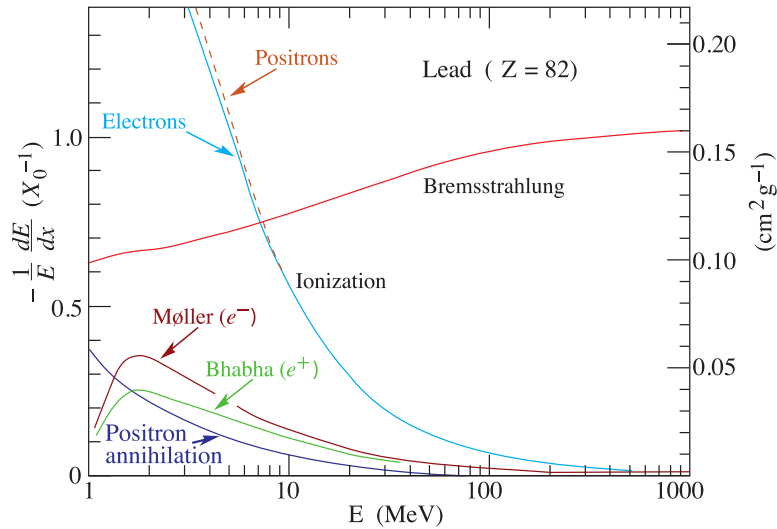


Figure 3.1: Processes for electron or positron collision in lead. Shown is the fractional energy loss per radiation length as a function of the electron energy for the different scattering processes. [23]

the energy at which the ionization loss per radiation length equals the loss in Bremsstrahlung. It can be approximated with

$$\epsilon_c \approx \frac{550 \text{ MeV}}{Z}. \quad (3.2)$$

for absorber with $Z > 13$. In calorimetry materials, the typical critical energy is around 10 MeV. The trajectory of the electron in matter changed to due Coulomb scattering on the nuclei but does not contribute to the energy loss. At lower energies electrons also lose energy via Møller scattering ($e^-e^- \rightarrow e^-e^-$), Bhabha scattering ($e^+e^- \rightarrow e^+e^-$), and positron annihilation ($e^+e^- \rightarrow \gamma\gamma$). Figure 3.2 shows all processes that lead to energy loss of photons in lead as an example. Low energy photons lose energy in matter mostly through the photoelec-

tric effect ($\sigma_{p.e.}$). This process involves a photon that is absorbed by an atom and an electron ejected consequentially. Compton scattering (σ_{Compton}) is the major process in the medium ($\approx 1 \text{ MeV}$) energy range. At high energies ($E_\gamma \geq 2 \cdot m_e c^2$) pair production becomes the dominant process. It can occur either in the nuclear field (κ_{nuc}) or in the field of atomic electrons (κ_e). Rayleigh scattering (σ_{Rayleigh}) and the giant dipole resonance ($\sigma_{\text{g.d.r.}}$) play minor roles

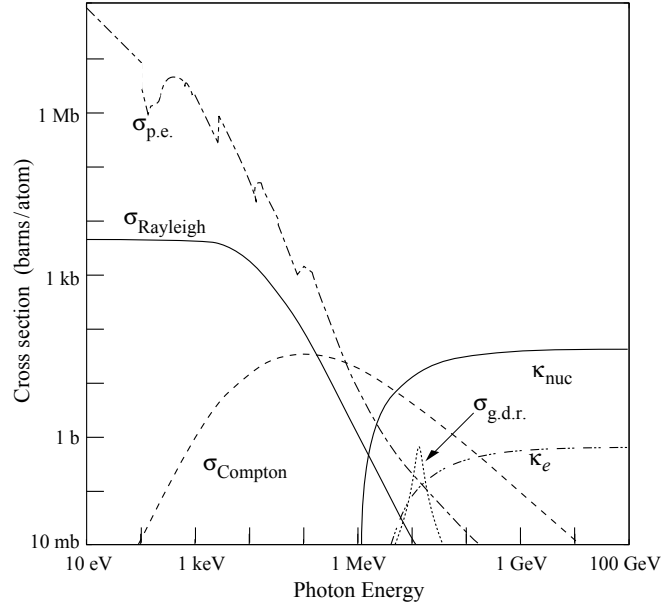


Figure 3.2: Possible processes for photon collision in lead. Shown is the cross section of different scattering processes depending on the photon energy over several order of magnitude. [23]

in photon absorption. The cross section of the dominant processes of Bremsstrahlung and pair production are almost energy independent for high energies. High energy photons and electrons transversing matter trigger the production of further electrons and photons with sufficient energy to undergo particle production themselves. An avalanche of electrons and photons as depicted in Figure 3.3 is created. This is called an electromagnetic shower (EM shower). The cascade reaches a maximum of particle production when the average electron energy is $\approx \epsilon_c$. The scale to describe such an electromagnetic cascade is the Radiation length X_0 . An electron immediately starts to emit γ through Bremsstrahlung. A photon entering a medium will travel a distance unobstructed before it is absorbed and generate a e^-e^+ pair. The mean free path of a Photon is related to X_0 via

$$L_\gamma = \frac{9}{7} \cdot X_0. \quad (3.3)$$

The Moliere radius describes the lateral extension of the shower.

$$R_m = \frac{21 \text{ MeV}}{\epsilon_c} \cdot X_0 \quad (3.4)$$

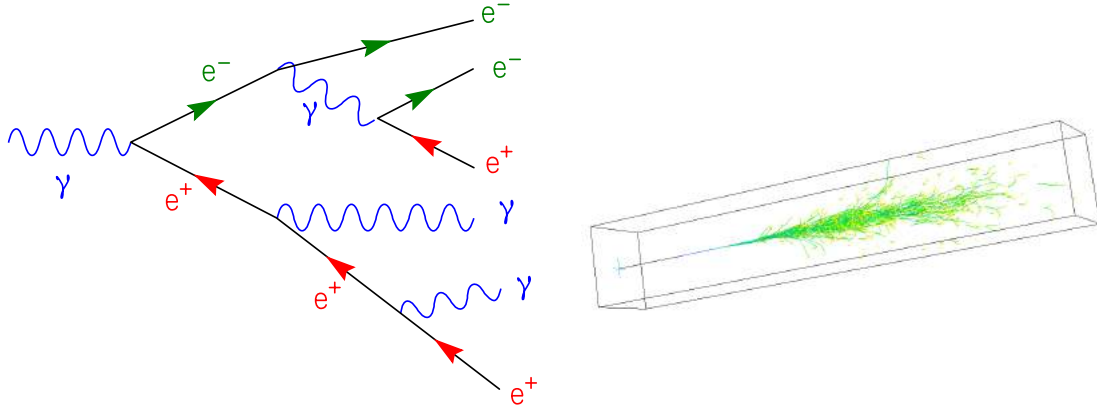


Figure 3.3:

Left: Depiction of the start of an electromagnetic shower cascade.

Picture by SCZenz / CC BY

Right: Simulation of a EM shower induced by a 24 GeV e^- in an iron absorber of $5 \times 5 \times 30 \text{ m}^3$.

Picture by the EM shower simulator (ELSS) from the MPI Munich.

A cylinder with the Moliere radius R_m contains 90% of the energy of the cascade, $3.5 R_m$ contain 99%. Note that R_m refers to the energy of the cascade, not the topological lateral extension that can be much larger. Electromagnetic showers are quasi instantaneous showers. This circumstance will be used for detector calibration in this thesis, see Chapter 11. In very rare cases depending on the material nuclear isomers [24] can be created through gamma or electron interaction. Those semi-stable states can have a decay time longer than 10 μs and can create low energy hits in a detector that are delayed.

3.1.2 Heavy Charged Particle Interaction

For heavy charged particles the energy loss via Bremsstrahlung is suppressed with the particle mass as $\frac{1}{m^4}$. For charged hadrons and muons the main electromagnetic process for energy loss is ionization. The losses are well described by the Bethe Bloch equation [23]

$$\left\langle -\frac{dE}{dx} \right\rangle = K \cdot z^4 \cdot \frac{Z}{A} \cdot \frac{1}{\beta^2} \cdot \left[\frac{1}{2} \cdot \ln \frac{2m_e c^2 \beta^2 \gamma^2 W_{max}}{I^2} - \beta^2 - \frac{\delta(\beta\gamma)}{2} \right] \quad (3.5)$$

With W_{max} the highest energy that can be transferred to an electron in a single collision. I is the mean excitation energy, and $K = 4\pi N_A r_e^2 m_e c^2$ is a normalization factor. The material has the atomic number Z and atomic mass A . $\delta(\beta\gamma)$ takes the relativistic correction occurring at higher energies into account. Figure 3.4 shows the energy losses of muons in copper as an example. In Particle Physics detectors, the ionization of a detection material generates either directly a detectable electronic signal or is transformed via scintillation (see Chapter 4) into detectable photons.

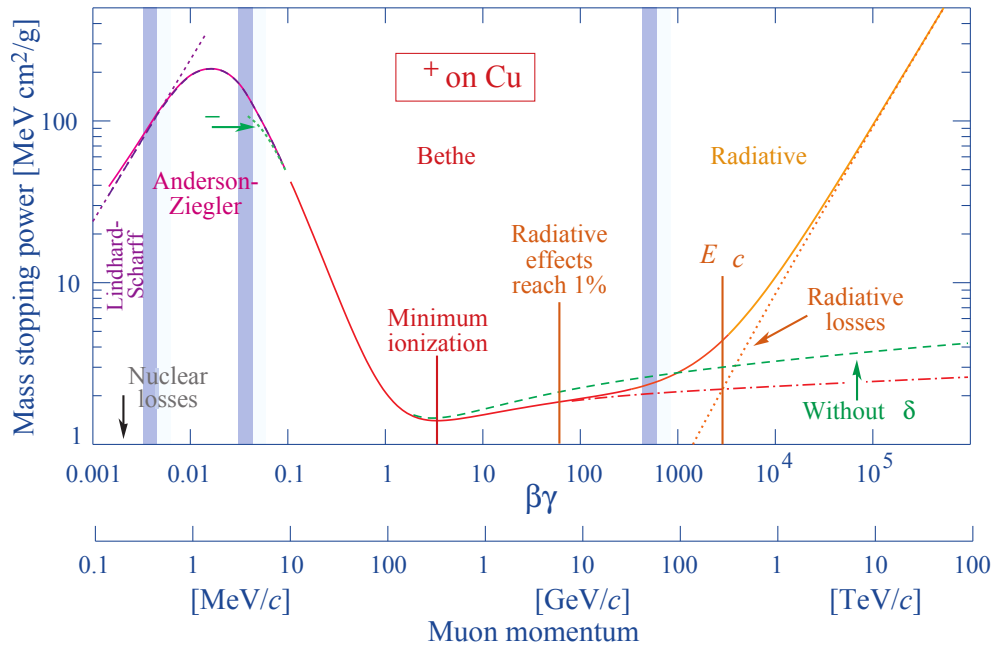


Figure 3.4: Stopping power of μ^+ in copper plotted against the velocity of the particle $\beta\gamma = \frac{p}{Mc}$. The horizontal lines indicate different regions of theoretical models. [23]

3.1.3 Muon Interaction

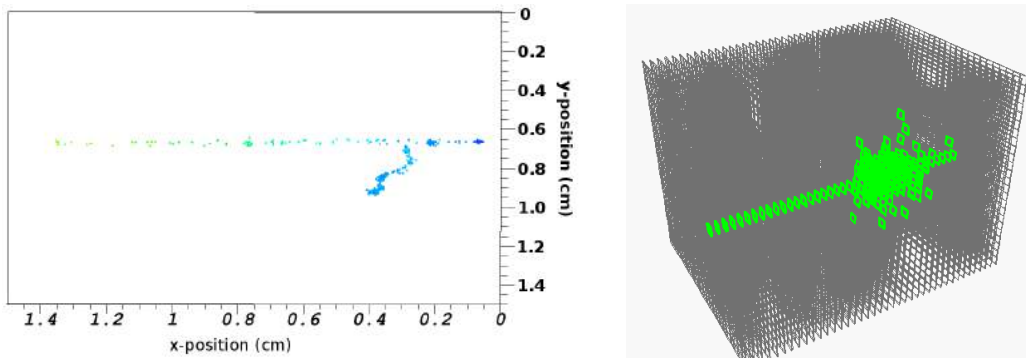


Figure 3.5:
 Left: A 3D representation of a delta electron knocked out by a 180 GeV muon, measured with a GridPix detector at the SPS at CERN. The color indicates the height.
 Picture by Wilcokoppert / CC BY
 Right: Simulation of a 180 GeV μ in a 1 m^3 iron sandwich calorimeter with 40 layers. The green boxes show the hits in the absorber. A shower from delta electrons produced by the muon unfolds while the Muons continues straight through the detector. (Simulation done with Geant4 by Marco Ramilli)

Muon energies are usually not measured in the normal calorimeter system due to their low energy losses in matter. They are measured in calorimeter tail catchers and muon systems that do not fully contain all Muons but estimate their energy. Muons primarily lose energy via Ionization. They can penetrate long distances in materials and have a long life-time making

a decay inside the detector not probable. The broad energy range in which a muon shows a minimum in the energy losses around (100 MeV to 1 GeV) provides a standard candle for energy calibration of a detector. The energy loss depends only weakly on the material. A muon at the minimum energy loss with 370 GeV is called a Minimal Ionizing Particle (MIP). Detector energy calibrations are carried out (via cosmic muons) or referred to the MIP. The produced electrons through ionization in equation 3.5 are following a Landau distribution with tails to high energies. For muons, that usually do not generate showers it is possible in rare cases to generate very high energy electrons (delta electrons) that have sufficient energy to produce electromagnetic showers of their own. Figure 3.5 on the left shows the measurement of such a delta electron shower in test beam. Especially in test beams (see Chapter 12), this can generate unexpected hits in the detector like the shower simulated in Figure 3.5 on the right. Nuclear isomers with late decays can also be created by delta electron inducing EM showers.

3.1.4 Hadronic Showers

Opposed to EM showers hadronic showers are dominated by strong interaction. Hadrons are not elementary particles but consist of quarks and gluons. Each of those constituents can interact via the strong interaction with quarks and gluons in matter that the hadron is passing. The scale to describe hadronic showers is the nuclear interaction length, approximated by

$$\lambda_I = \frac{k\sqrt{3}N}{\rho} \quad (3.6)$$

where N is the number of nucleons, ρ is the density of the material and $k = 35 \frac{g}{cm^3}$ is a constant. λ_I is the mean length for a hadron to travel through material without nuclear interaction with a $\frac{1}{e} = 37\%$ probability. The multitude of processes involved in hadronic showers leads to a complex structure that is subject to strong statistical fluctuation and different energy depositions in media. Figure 3.6 on the left shows the general processes involved in hadronic showers. The different processes lead also to a very uneven distribution of the energy throughout the detector as can be seen in Figure 3.6 on the right in simulation. The processes through which hadrons lose energy in a medium and the processes developing hadronic showers are listed below in chronological order.

Ionization

Charged hadrons lose energy in a medium as heavy charged particles following equation 3.5. The ionization in a medium produces low energetic electrons that can be used to detect the path of the particle. Following the Landau distribution of the transferred energy, high energetic delta electrons can also be produced, inducing small EM Showers.

Inter-nuclear cascade

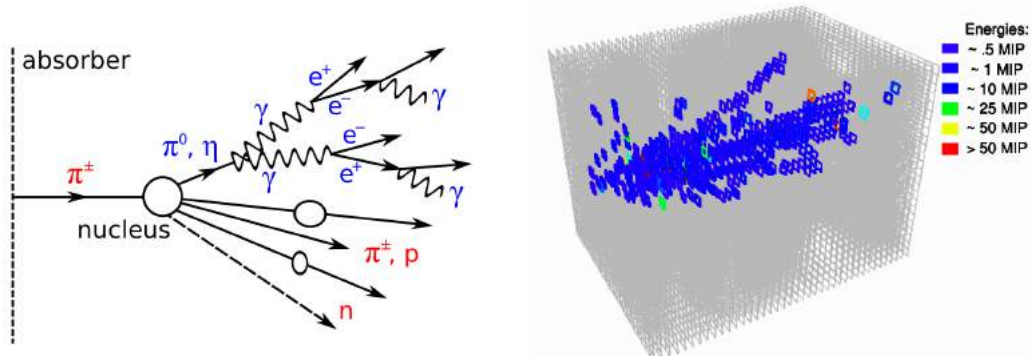


Figure 3.6:

Left: Depiction of different processes occurring during hadronic interaction leading to hadronic shower cascades. In red all hadronic interactions and in blue electromagnetic interactions. A once triggered EM cascade cannot lead to further hadronic interaction [25]. Over 90% of the produced particles are pions, of which the neutral pions decays into $\pi^0 \rightarrow \gamma\gamma$ to develop EM showers [26].

Right: Simulation of a 180 GeV π^- in a 1 m^3 iron sandwich calorimeter with 40 layers. The colored boxes show the energy of the hits in the detector. (Simulation done with Geant4 by Marco Ramilli)

Following a hard collision between an incident hadron and a nucleus of the absorber, forms a inter-nuclear cascade through strong interaction. Energy is transferred for the breakup of the nucleus. This energy is called invisible energy since is cannot be detected in any way. Through the fragmentation of the nucleus and breakup of $q\bar{q}$ pairs, a cascade of particles is produced leaving the nucleus focus around the original path of the incident particle. Compound nuclei are emitted slower after 10^{-18} s from the initial collision. This forms the very fast shower component that traverses the medium with almost the speed of light [27].

Nuclear Evaporation and Fission

The nucleus is highly excited after a collision and loses its energy through evaporation (or evaporation followed by fission) of particles (Neutrons, Protons, α , γ) through the lower energy states of the unexcited nucleus. The produced particles are emitted isotropically. Nearly all evaporated particles are soft neutrons produced in a great amount. The de-excitation can happen after sub ns to several μs . Those late soft neutrons can travel in the medium and eventually deposit energy through neutron capture ($\approx 1\text{ eV}$), inelastic scattering ($\approx 10\text{ MeV}$), and elastic scattering ($\approx 1\text{ eV}-1\text{ MeV}$) [26]. The amount of slow neutrons produced depends greatly on the material. The energies involved are generally in the order of 1 MIP.

Electromagnetic fraction of hadronic showers

A great portion of the energy is deposited in compact EM showers produced by secondary particles, mainly $\pi^0 \rightarrow \gamma\gamma$. EM shower components can only trigger further EM showers so once an EM shower is produced from one of the particles in the hadronic cascade it deposits all its energy in a compact portion of the material. The energy fraction attributed to pure EM showers is called the electromagnetic fraction of an hadronic shower, f_{EM} . It is greatly dependent on the energy and sort of incoming particle as well as the atomic number Z of

the absorber material and subject to great fluctuations. The distinction of the energy into hadronic fraction and f_{EM} is important in hadronic calorimetry due to the distinctly different response function of calorimeters to both components, see section 3.2.1.

Hadron decay

Hadrons can undergo hadronic or leptonic decay via the weak force. The leptonic decay forms also neutrinos which are escaping energy since they are not interacting with the detector. The muon energy can partly be measured in the muon systems of detectors but does also account for escaping energy.

The ratio of the different energy depositions in two sample material is shown in Figure 3.7. The shower keeps on developing and the secondary particles undergo further inelastic collision until their energy falls below pion production threshold. Hadronic showers are complex processes and undergo huge statistical fluctuation. This changes the energy deposition for same particles greatly per event. The multitude of different processes involved further complicates the measurement of the energy of an hadronic particle.

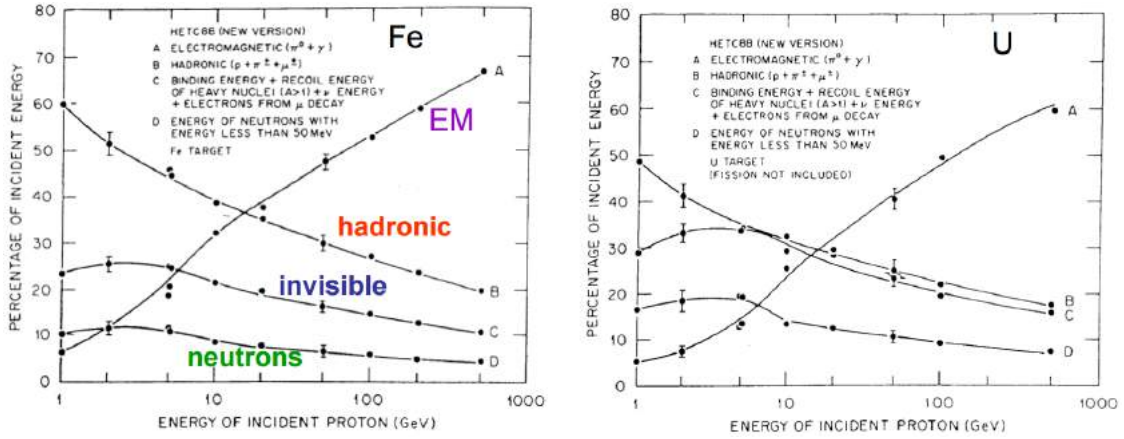


Figure 3.7: Deposited energy fraction for a proton of different energies in lead (left) and uranium (right) absorbers. The fraction of energy deposited in the different processes differs greatly from material to material. Especially for higher energies the EM fraction is the dominant energy deposition. [28]

3.1.5 Time development of Hadronic Showers

The understanding of the time regimes involved in the complex hadronic showers has been a field of research for a long time. The timing capabilities of a detector like the spaghetti calorimeter of the LAA project at CERN [29] or the ZEUS calorimeter at DESY [30] have been used for this process. Only recently efforts within the CALICE collaboration to disentangle the complex time structure of hadronic showers have led to dedicated setups like T3B [31], that research this field. The excellent time resolution of the CALICE detectors make further measurements possible. In Chapter 12 this topic is described to a greater extend. This

section only introduces the general time evolution of hadronic showers. An excellent thesis looking into details can be found in the thesis from Christian Soldner [32]. As a sample

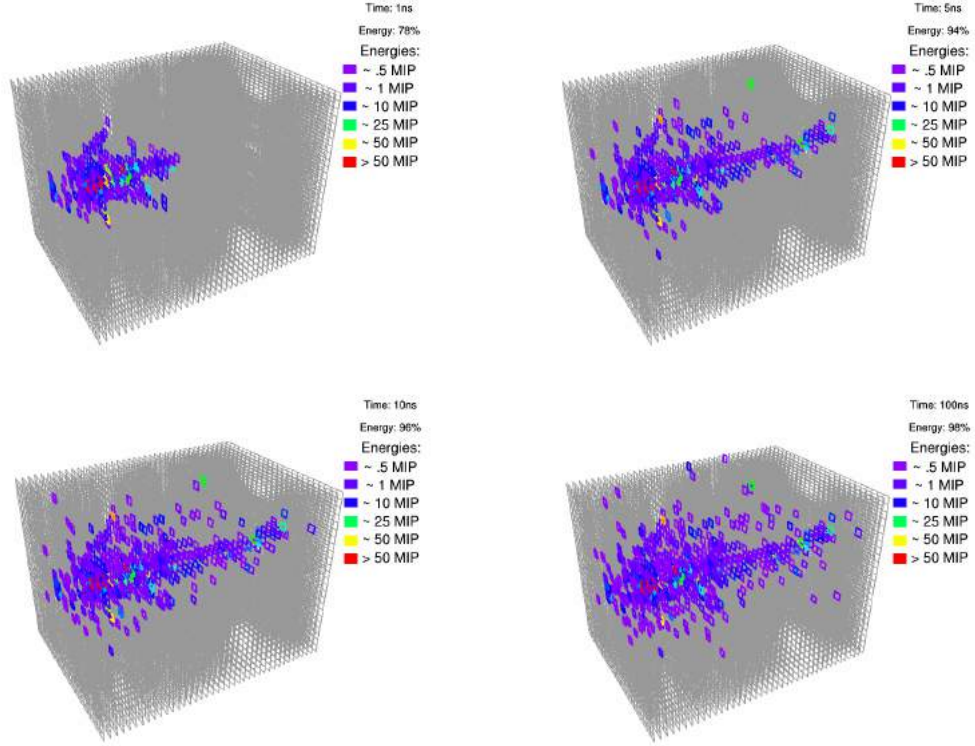


Figure 3.8: Hadronic shower from a 180 GeV π^+ in simulated 1m^3 sandwich calorimeter with tungsten absorber. The four pictures show the development at 1 ns, 5 ns, 10 ns, and 100 ns after the first hard interaction. In the first interaction, dense EM showers are produced and 78 % of the energy is already deposited within the first ns. After 3.3 ns a speed of light particle traverse the detector. The 5 ns picture shows that the quasi instantaneous reactions and secondary particles are already produced, depositing 94 % of the energy. 5 ns later only small energy deposition are made from slow neutrons that continue to evolve over time and form a uniform detector halo eventually depositing all energy.

Energy percentages refer to the total deposited energy in the active layer for $t \rightarrow \infty$.

(Simulation done with Geant4 by Marco Ramilli)

one π^- shower event is shown in Figure 3.8. Four different time steps in the evolution of the shower are shown. Most of the energy in a hadronic shower is deposited within one or a few ns, coming from charged hadrons or particles in f_{EM} . Low energetic and non-relativistic neutrons produced in the shower deposit their energies with delays up to several μs . Around 10 % of the shower energy is carried by those neutrons [26]. Depending on the rate of the incident particles, those delayed energy contribution can produce a constant background of hits in the calorimeter system that becomes indistinguishable from random hits in the calorimeter produced by electronic noise or cosmic showers [30].

3.2 Calorimetry

Calorimeter systems are usually divided into an electromagnetic calorimeter that measures the energy of incident electrons and photons and an hadronic calorimeter system that measures the energy of heavy particles. Most systems are followed by a muon and or tail catcher system with limited energy resolution to estimate the energy of escaping hadronic showers or muons. This part of the thesis focuses on hadronic calorimeters since the detection principle is equivalent apart from the greater mass of the absorber and different materials used. A more detailed look into the resolution of EM calorimeters is given in Chapter 5.

3.2.1 Sampling Calorimeter

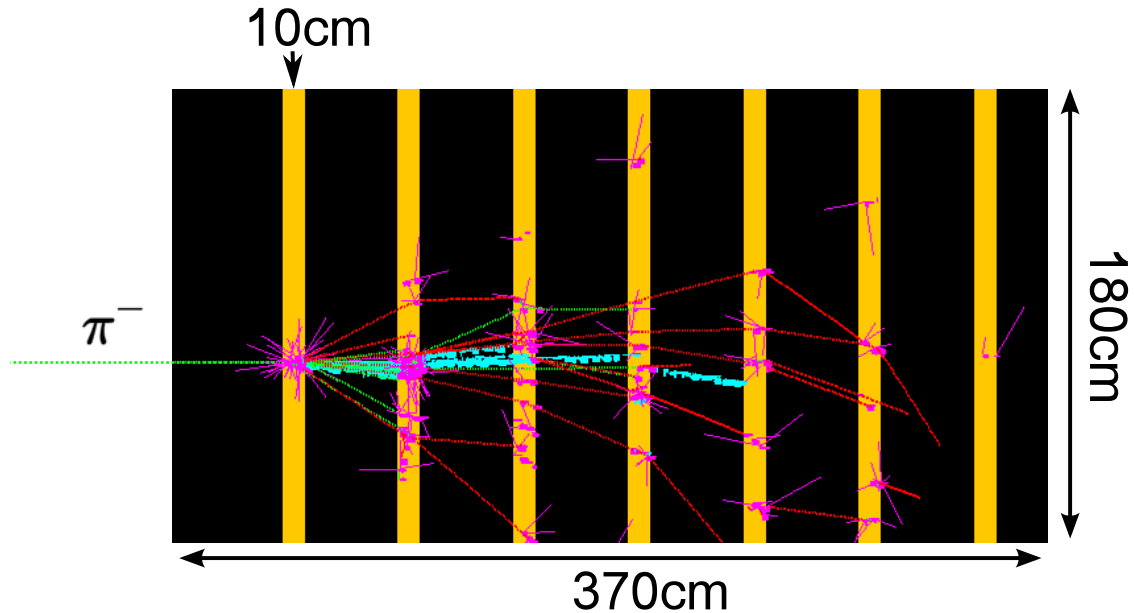


Figure 3.9: Simulation of a 180 GeV π^- entering a sandwich calorimeter. Tracks through ionization are shown in color-coding to distinguish the produced particles. The 10 cm thick absorber layers are Iron while the detection medium is simply air to demonstrate the evolution of the shower. Pink are core fragments following a nuclear interaction. Green are charged pions. Cyan neutral pions that induce EM showers while protons are red. Singled out pink nuclear reactions are induced by neutrons that do not leave traces through ionization. GHEISHA Simulation by www.harfesoft.de

The general purpose of a calorimeter is to measure the full energy of a particle. To achieve this goal, the whole energy of the particle deposited in showers need to be measured. Therefore all produced particles need to be contained so that they can deposit their energy inside of the detector. This makes the calorimeter a mostly thick and dense object to provide enough interaction length for the incident particles contributing to the energy measurement and keep costs of the detector at acceptable levels. Materials have a different response signal to f_{EM} and the hadronic fraction. Since f_{EM} is depending on the energy of the incident particle this leads to a non-linear response of calorimeters. Efforts to overcome this non-

linearity is called compensation. The compensation problem is fought in HCALs by choosing the right mixture of materials for the absorbers or using software compensation, estimating the energy of the particle and correcting it iteratively [33]. For event reconstruction it is important to not only reconstruct the energy of the particle but also the complete four-vector. Neutral particles leave no trace in other detector components. Only the calorimeter system can reconstruct the four-vector, which is important to determine missing energy from e.g. ν . Spacial resolution is achieved by segmenting the detector. Especially important is a fine segmentation for the Particle Flow method as described in detail in Chapter 5. In homogeneous calorimeters the whole volume consist of one high Z materials (or mixtures) for absorption and detection. Examples are the CMS Crystal Calorimeter [34] and the Liquid Krypton Calorimeter at NA48 [35]. Fundamental restriction make those types of calorimeters suitable for EM calorimeters, achieving an unmet energy resolution, but would result in a huge volume for HCALs for high energy hadron detectors. To achieve a dense object and good spacial detection capabilities many HCALs are build as inhomogeneous sampling calorimeters with the depicted principle in Figure 3.9. Passive dense absorption layers and active detection layers are alternated. Only a fraction of the produced energy can be measured [36] since the energy deposited in the dense absorber is invisible to the detector. This is called the sampling fraction f_{samp} . Inhomogeneous calorimeters also pose a chance to overcome the problem of compensation by tuning the response to the different fraction with materials in the absorber or detection layers. This has been demonstrated by the self-compensating ZEUS calorimeter build out of Uranium [37].

Energy resolution

The uncertainty of the energy measurement σ_E related to the actual energy E is the resolution of the calorimeter,

$$\frac{\sigma_E}{E} = \frac{a}{\sqrt{E}} \oplus \frac{b}{E} \oplus c. \quad (3.7)$$

Three contributions are generally parametrized. The stochastic term $\frac{a}{\sqrt{E}}$ decreases with particle numbers $N_p \propto E$ that contribute to the measured energy. With higher energy E more particles are produced. $\frac{a}{\sqrt{E}}$ is expressing the sampling and quantum fluctuations of the hadronic showers. a is an individual constant for each device. $\frac{b}{E}$ is mainly influenced by the noise of the calorimeter. With higher energy, the noise of the calorimeter contributes lesser to the energy resolution. Radioactivity in the detector material also contributes to the noise term. The constant term c addresses all sources of error independent of the energy like inhomogeneities either from hardware (imperfections in the structure) or calibration (also non-linearity of the readout) deteriorating the energy resolution. Dead material and the lost energy due to leakage of showers outside of the calorimeter contribute as well.

Chapter 4

Photon detection

A large variety of technologies can be found to detect shower particles in calorimeters. The collection of ionized charges through gas or silicon, Cerenkov light detection or detection of light from different kinds of scintillators are the most common technologies used. Many processes in high energy Physics to detect particles and measure their energy use very small amounts of visible light. For example Cerenkov light from changing the speed of light through use of different materials as well as fluorescent light from crystal and plastic scintillators. Those processes produce from single photons up to several thousand photons per passing particle. Those small light amounts need to be transformed into an electrical signal corresponding at best linearly with the amount of photons. Photomultiplier tubes (PMT) have been the detector of choice for over 80 years, combining single photon resolution with high dynamic range. Their handling and complex manufacturing process makes them an expensive and complex photon detector. High voltage power supply, costs, sensitivity to magnetic fields, and bulky dimensions are limiting factors for their use. Efforts by Hamamatsu in miniaturizing PMTs [38] met a fundamental threshold with the size of a fingertip. Recent developments in semiconductor technologies made it possible to combine benefits of PMTs (single photon detection and dynamic range) with the advantages of silicon based photon detectors like the easy handling, size and cost efficiency. Evolving from photo diodes and Avalanche photo diodes (APD) detectors on the sub-millimeter scale with single photon detection up to several magnitudes of light intensity have been made possible with the development of Silicon photo multipliers (SiPMs, [39] and [40]).

4.1 Detection media for Hadronic Calorimeters

Scintillation is a property of photoluminescence. The material emits photons when excited by ionizing radiation. The emittance of photons can range from instantaneous to delayed for hours by Pauli principle. Long term scintillation is called phosphorescence. Scintillators are grouped into Inorganic and organic scintillator as well as gases. Gases scintillate through

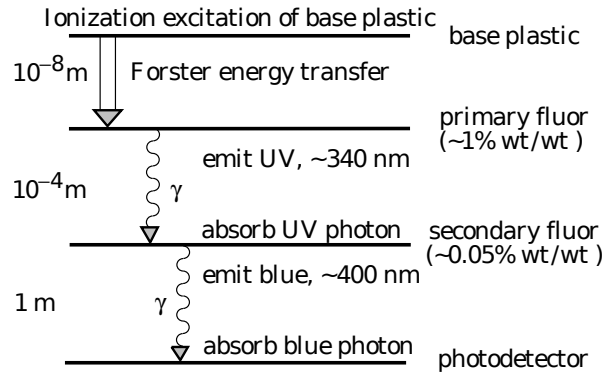


Figure 4.1: The scintillation “ladder” of an organic scintillator. The excited base plastic transfers its energy via Förster energy transfer [41] to the primary fluor. Photons emitted through fluorescence reach the secondary fluor which undergoes fluorescence, shifting the wavelength further down to detectable wavelengths. Approximate fluor concentrations are shown.[23]

the de-excitation of single atoms in a rapid process (<1 ns). The scintillation process in inorganic scintillators is not molecular in nature, but is due to the band structure of a grown crystal. An incoming particle excites an electron from the valence band to the conduction (or exciton) band and the electron emits photons through relaxation to ground state. Inorganic scintillators need to be grown in large crystals e.g. BaF_2 or $PbWO_4$. In principle the photon production process is the same in organic crystal scintillators which are seldom used. The scintillation process of organic scintillator is shown in figure 4.1. They produce photons through ionization of a base medium that follows photon relaxation. Fluorescence of several materials, usually fluors are used to shift the wavelength via Stokes shift. Plastic scintillators have embedded fluors in a base substance like Polystyrene (PV) or Polyvinyltoluen (PVT). The concentration of the primary fluor is chosen to minimize the atomic distance to the base material to under the emitting wavelength. The primary fluor is then excited via Förster energy transfer [41] to speed up the process and efficiency. The fluor then emits photons through fluorescence, usually in the high UV region. A secondary fluor is used as a wavelength shifter to emit UV or blue photons through fluorescence to shorten the decay time of the primary scintillator but also to enlarge the attenuation length. PV and PVT have a longer attenuation length for lower wavelength and the efficiency of photon collection is increased. The produced blue and UV photons are either collected and shifted further to the green region through fluorescence or detected directly by blue sensitive photo detector.

4.2 Photomultiplier tube (PMT)

Single photon detection is needed to measure the small amounts of light produced by scintillating detector. PMTs are photon detectors with a sensitivity down to single photons. An incident photon produces a photo electron on the photo-cathode of the photomultiplier tube which is multiplied via avalanches into a usable electronic signal. The operational principle

is depicted in figure 4.2. Through a series of dynodes an avalanche of secondary electrons are produced. The high voltage between the dynodes accelerates the electrons to energies high enough to produce secondary electrons on impact with the dynodes. An Anode at the end of the PMT collects the signal that can be several million electrons from a single photon. Single photoelectrons up to the several thousands can be detected this way. PMTs are sensitive and expensive photon detectors with several shortcomings for operation. A high voltage source of 10^2 V to 10^4 V is needed. Their macroscopic dimensions of several cm and strong sensitivity to magnetic fields make an operation inside a strong magnetic field complicated.

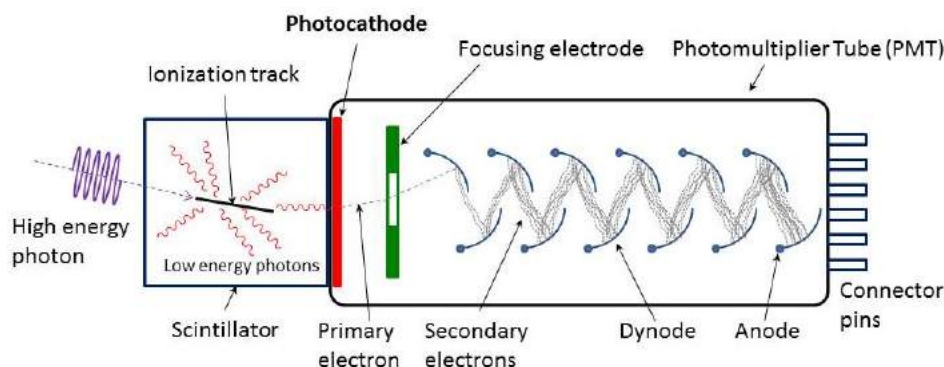


Figure 4.2: Principle of the PMT: low energy photons produced by a detection crystal form primary electrons on impact on the Photocathode. High voltage between the dynodes accelerate electrons which produce a cascade of several thousand electrons on impact on the dynode.¹

4.3 Photodiode

Photo detectors based on silicon take advantage of electron hole pair generation from incident photons. Reverse biasing a p/n diode depletes the region between the p and n junction, see figure 4.3. If a photon hits the depletion zone it generates an electron/hole pair if its energy is bigger than the difference between the conduction and valence band (1.2 eV in silicon). The electron and hole travel to opposite sites of the semiconductor and generate a current. A silicon based Photodiode is cheap in production and easily handled even in strong magnetic fields. In a Photodiode no amplification is involved. Small light quantities do not produce an electronic signal that can be detected. A higher reverse voltage only leads to a prompter pulse and smaller chance of recombination of the electron hole pairs.

4.4 Avalanche Photo-diode (APD)

Figure 4.4 shows an avalanche Photo-diode. They are PIN diodes ([43] and [44]) with an additional highly-doped multiplication area. The doping concentration is modeled to create

¹Picture by Qwerty123uiop / CC BY

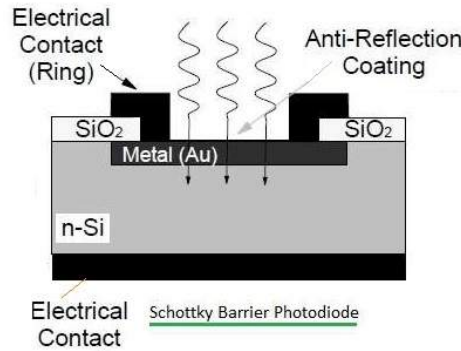


Figure 4.3: Schottky-Barrier-Photodiode. Photons with energies over the band-gap (1.2 eV in silicon) create electron hole pairs in the absorption region leading to a detectable current over the diode. Picture from [42]

a high field region for acceleration of electrons to energies sufficient to create several electron hole pairs in a multiplication region due to impact ionisation. An electron avalanche develops that amplifies the signal generated by photon by 100-500 times. The signal generated by an APD is proportional to the incident photons. The amplification of an APD has a strong temperature and voltage dependency that needs to be closely monitored during operation.

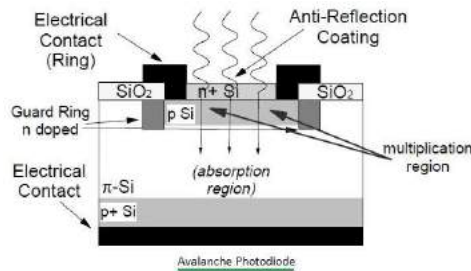


Figure 4.4: Avalanche photo diode. Photons create electrons carriers in the absorption zone which drift towards the p implant. The high electric field building up in the p implant accelerates electrons to energies high enough to produce several electrons and generate a self sustaining avalanche. Picture from [42]

4.5 Geiger mode APD

Figure 4.5 shows the characteristics of an APD operated in different voltage ranges. At low voltages no amplification takes place since the acceleration energy of the electric field in the amplification region does not pass the electron hole pair production threshold. At higher voltages, electron hole pairs create amplifying avalanches. The breakdown voltage V_{bias} is the voltage at which the acceleration energy surpasses this threshold. An APD shows a linear amplification of up to ≈ 500 for operation with voltages below the breakdown voltage (V_{BD}). Above breakdown voltage, every electron hole pair can generate an avalanche of electrons that becomes self-sustaining and would destroy the diode with high currents (Geiger avalanche [45]). Such avalanches are triggered by single photons or thermal excitation creating

electron hole pairs. The avalanche can be stopped by lowering the voltage below breakdown after each avalanche (quenching). APDs operated in Geiger mode are quenched passively or actively with integrated circuits. Passive quenching is achieved by setting a resistor in series with the APD. This forms a voltage divider. An avalanche lowers the almost infinite resistance of the APD to a very low value, causing the voltage to drop over the resistor instead of the APD. The APD recovers to its previous state and the voltage over the APD raises over breakdown voltage again. Every Geiger discharge depletes the whole APD and delivers always the same amount of charge no matter how many photons hit the APD at the same time. Due to their high quantum efficiency (QE) in visible light of over 90% silicon or gallium arsenide APDs operated in Geiger mode are widely used in single molecule spectroscopy, counting single photons released by a molecule one at a time.

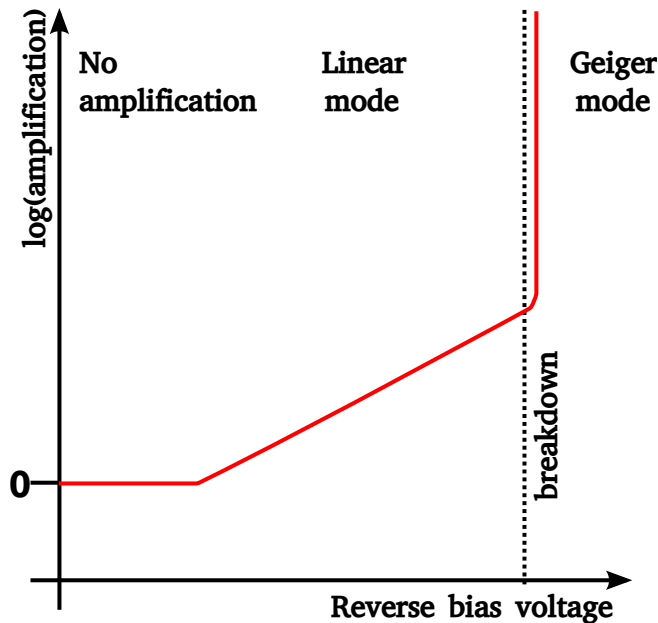


Figure 4.5: APD amplification versus voltage. Avalanches are generated from electron hole pairs over the generation threshold. In Geiger mode [45], each electron hole pair can generate a self-sustaining avalanche in the diode.

4.6 SiPM

Combining the single photon resolution of PMTs and the compact (and cheap) form factor of a silicon based integrated circuit, SiPMs have been developed. A Silicon photo multiplier (SiPM) is an array of passively quenched APDs in Geiger mode on the same silicon device. Hundreds or thousands of APDs are connected in parallel (see figure 4.6) and reversely biased with the same voltage source. The single APDs are referred to as pixels. The pixels of a SiPM are uniform and their signals identical. If several pixels are hit by photons, the signals add up as can be seen in the left side of figure 4.7. On the right side the integration and the charge

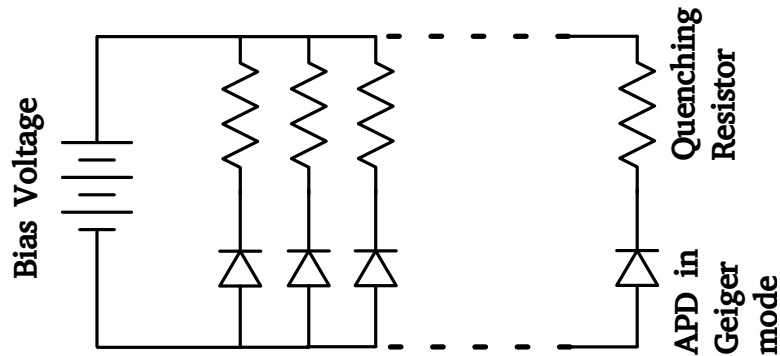


Figure 4.6: A SiPM is an array of passively quenched APDs connected in parallel adding up their signals. All are reversely biased in Geiger mode with the same bias voltage.

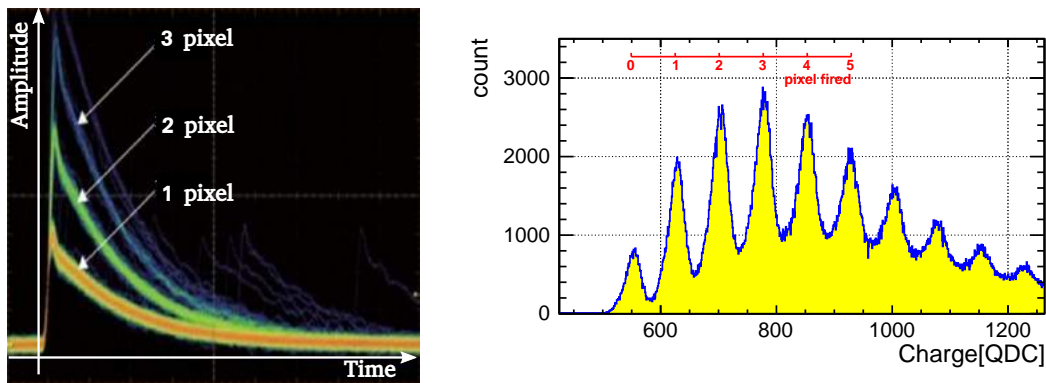


Figure 4.7: SiPM signal

Left: SiPM signal voltage versus time on a persistent oscilloscope screen. Each pixel fired provides the same amount of charge and the waveforms add to each other for several pixels fired at the same time

Right: The same signal integrated over time with a QDC in arbitrary units. In red the fired pixel scale. Taken with Tektronix 7540 on a Hamamatsu S10400 SiPM without light.

of the signal is shown. Each pixel discharges the same amount of charge. The gain of a SiPM is the charge of one pixel. Several pixels firing at the same time give the sum of multiple charges. The size of a pixel is in the μm range, enabling hundreds or thousands of pixels on a sub-millimeter scale. The quenching resistors are built-in on the silicon wafer, making it a very compact and easy to use device. Depending on the specific design of the SiPM, green light, and recently also blue light as well as UV light sensitive SiPM are produced by various manufacturers.

4.6.1 SiPM characterization parameters

Breakdown Voltage

The single pixels operated in Geiger mode for voltages over breakdown, see figure 4.5. The breakdown voltage is unique for each SiPM and depends on the temperature. All figures of

merit are usually described in terms of excess bias voltage or over voltage,

$$\Delta V(T) = V_{\text{bias}} - V_{BD}(T) \quad (4.1)$$

.

Gain

The charge generated from a single avalanche process of a single pixel (one APD) is the Gain G . In approximation the SiPM gain depends on the pixel capacity,

$$-G = \frac{C_{\text{pixel}} \cdot \Delta V}{e} \quad (4.2)$$

with e being the elementary charge. The gain thus depends on the temperature and the excess bias voltage which can be expressed as

$$\frac{1}{G} \cdot \left(\frac{\partial G}{\partial T} \right) = -\frac{1}{\Delta V} \cdot \left(\frac{\partial V_{BD}}{\partial T} \right) \quad (4.3)$$

.

Dark Count Rate

Randomly discharging pixels leading to the dark count rate (DCR) of a SiPM are triggered by thermal excitation or tunneling of charge carriers through the band-gap. Only single pixels are discharged at a time. Typical values of DCR for a SiPM are 100 kHz- 1 MHz.

Pixel Crosstalk / After-pulse / Correlated Noise

After pulses are triggered by trapped charge carriers in the silicon lattice that are released after a certain amount of time. When the pixel recovered from the discharge, a new avalanche is triggered by those charge carriers, leading to correlated noise. Optical photons are released during the Geiger discharge inside a pixel due to coulomb interaction and Bremsstrahlung. Those photons can trigger a discharge in neighboring pixels. Both pixel crosstalk and after-pulses are correlated noise and are almost indistinguishable if the waveform is not sampled. For simplification in this work XT_{corr} combines after-pulses and crosstalk as correlated noise.

Photon Detection Efficiency

The fill-factor (FF) of a SiPM is the ratio of active (sensitive to light) versus the passive areas (resistors, lines). With the quantum efficiency (QE) defined as in section 4.5 and the probability of creating an avalanche depending on the excess bias voltage as AP, the photon

detection efficiency (PDE) is defined. The PDE determines the probability of one photon incident on the SiPM triggering a signal as

$$PDE = QE \times AP \times FF \quad (4.4)$$

Saturation response function

With higher light signals a majority of the pixels are already fired when they are hit with photons and do not discharge. This leads to a non linearity with higher light intensities and saturation for high light intensities. Figure 4.8 shows a detailed simulation developed by Chen Xu of a SiPM including all previously mentioned properties. Up to 10% fired pixels the deviation from linearity stays under 1%.

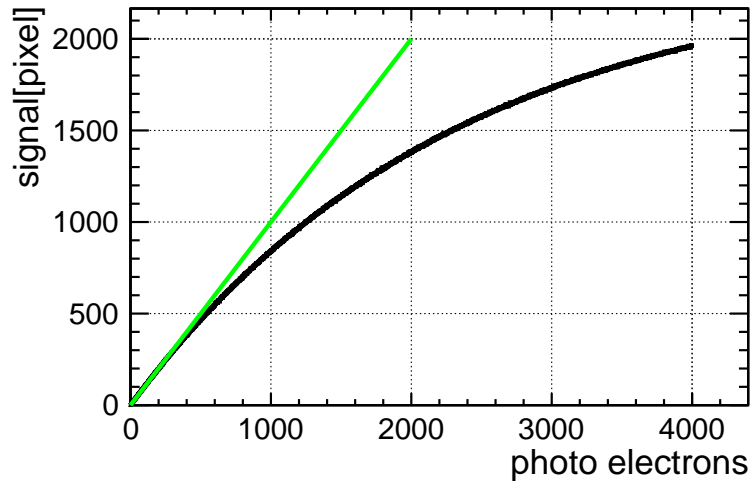


Figure 4.8: Saturation of a SiPM with DCR = 200 kcps, XT=3%, 2304 pixel. A noticeable deviation from linearity over 1% occurs when more than 10% of the pixel are hit (green linear line for guidance). ROOT SiPM simulation package from Chen Xu [46].

Chapter 5

Particle Flow

The hadronization of quarks and gluons following a hard scattering produce a narrow cone of boosted hadrons and other particles. These objects are called Jets. Many processes in ILC will include multi-jet final states. Physics analysis at the ILC could involve hadronic decays into 8 jets and more [47]. Of particular interest are the full hadronic decays of W^\pm ($W^\pm \rightarrow q\bar{q}$) and the Z^0 ($Z^0 \rightarrow q\bar{q}$) bosons. They have been set as a benchmark for detectors at the future linear collider. Figure 5.1 shows possible production and decay. The bosons produce each jets with a multitude of hadrons. The goal is to measure the resulting jet energies as the sum off all contributing particles well enough to separate both processes. The natural width of the separation measured with a detector with perfect energy resolution is 3.1σ . A Jet energy resolution of $\frac{\sigma}{E} = \frac{\alpha}{\sqrt{E(\text{GeV})}} = 3.5\%$ gives a decent 2.6σ - 2.3σ level and has been set as the goal for the jet energy resolution of an ILC detector. The energy of a typical jet is

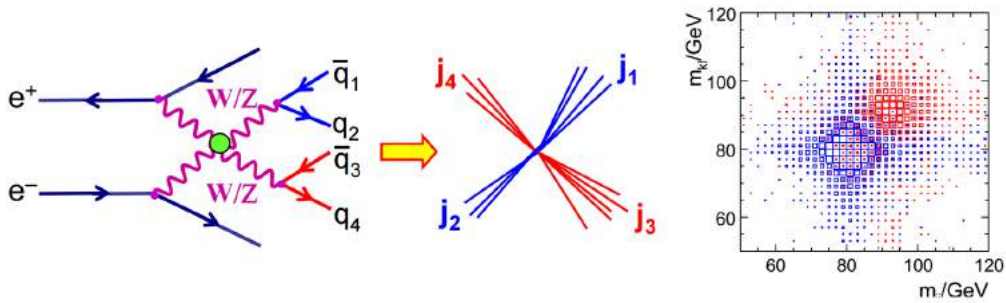


Figure 5.1: Production and full hadronic decay into four jets from W^\pm and Z^0 at the ILC. The middle Figure shows the emission of the four back to back jets, for the W^\pm W^\pm in blue and the Z^0 Z^0 in red. The rightmost Figure shows the resulting mass measurement. A resolution of 3.5% on the energy is sufficient to separate both processes.

Picture by Mark Thomson

distributed as $\approx 60\%$ charged particles, $\approx 30\%$ photons, and $\approx 10\%$ neutral hadrons. At a 500 GeV ILC the primary interest is in 4-6 fermion final states e.g. $e^+e^- \rightarrow Z^0 H \rightarrow q\bar{q}b\bar{b}$ and $e^+e^- \rightarrow t\bar{t} \rightarrow bq\bar{q}bq\bar{q}$. This sets the typical energy scale for jets at ILC to be from 60 GeV to 125 GeV (250 GeV in case of a 1 TeV ILC). Conventional Particle Physics approach to

measure jet energies purely with the calorimeter systems cannot achieve this resolution since the typical HCAL resolutions are bigger than $\frac{60\%}{\sqrt{E}} + c$. New approaches like dual readout [48], totally active [49], and particle flow [50] are necessary. The two proposed detector concepts at ILC (ILD and SiD) are both detectors specifically designed for the particle flow approach.

5.1 Particle physics detectors

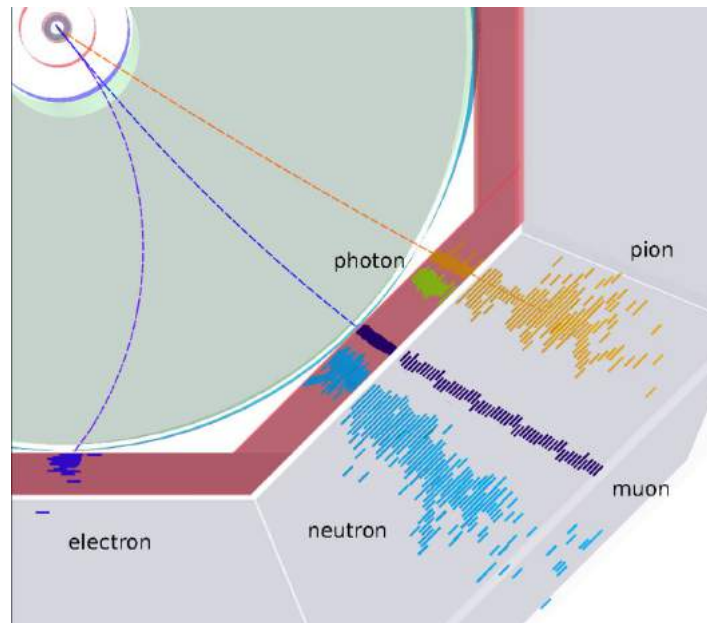


Figure 5.2: Conceptual depiction of signals of different particles in a detector (for better visualization no absorber in the calorimeters is shown):

From inside to outside: The tracking system consists of a silicon tracker (red blue and light green rings in the upper left) and a time projection chamber (TPC, green). The calorimeter system consists of an ECAL (red) and an HCAL (gray).

Different particles leave characteristic energy depositions. An electron (in blue) leaves a bend track and showers electromagnetically mainly in the ECAL with leakage into the HCAL. A neutron leaves no track and produces hadronic showers with lateral extension in the ECAL and HCAL. A muon passes all systems leaving mostly small energy depositions along its track. Photons mostly do not interact in the tracking system and shower in the ECAL. Charged hadrons like pions leave extensive hadronic showers in the ECAL and HCAL. They also produce a track in the tracker.

Picture by CERN[©]

All purpose detectors at high energy physics facilities like the ILC are hermetic detectors. They are called 4π detectors and cover all possible decays in all possible directions after a collision. They are designed to measure charge, momentum and energy of all escaping particles. Multiple specialized detector types cooperate as sub-detectors. ATLAS and CMS at the LHC are such detectors. They usually are cylindrical in shape due to the need of a strong magnetic field to identify and measure charged particles.

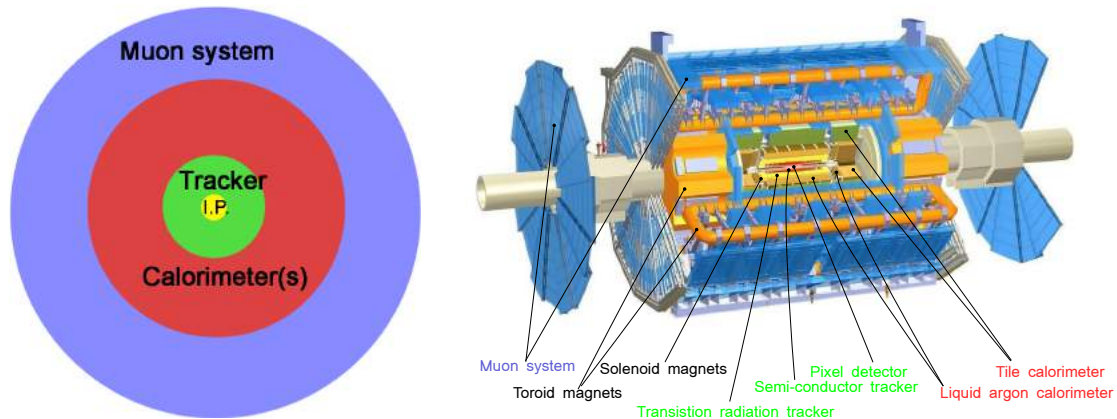


Figure 5.3:

Left: conceptual design of a standard particle physics detector with the tracker close to the interaction point (I.P.). The tracker has minimal material budget not to obstruct the path of the particles it is measuring. The dense calorimeters stop particles and measure their energy.

Right: The ATLAS detector with components. Colors indicate which subsystem belongs to the concept on the left.

figure on the right by Presbyterian / CC BY

Figure 5.3 on the left depicts the general layout of such a detector, while on the right an actual layout of the ATLAS detector can be seen. Conceptually the different subsystems can be divided into:

Trackers

The magnetic field of the detector forces charged particles into a rotation via the Lorentz force. The tracking system reconstructs the helix of the particle as it travels through finely segmented detectors. It deposits a minimal amount of energy through ionization. Trackers usually consist of several subsystems depending on the distance to the interaction point. Materials used for trackers are e.g. silicon (most commonly used, no external amplification needed), scintillating fibers, and gaseous detectors (external amplification needed).

Calorimeters

Calorimeters are dense detector sub-systems that absorb the energy of incoming particles. The absorbed energy is transformed into a measurable signal through different designs, e.g. scintillation, RPCs, and even silicon planes. Calorimeters are usually divided into two subsystems, the electromagnetic calorimeter (ECAL), measuring the energy of photons and electrons and the hadronic calorimeter (HCAL) measuring the energy of incoming hadrons.

Muon system

Muons and neutrinos pass through the calorimeter without losing most or any of their energy. Neutrinos cannot be detected through conventional methods and show up in the final sum as missing energy. Muons are measured and their energy estimated through muon calorimeters outside of the main coil of the detector.

Figure 5.2 shows the passing of different particles through the different detector components. The characteristic energy depositions of different kinds of particles are used to distinguish them. From left to right: Electrons leave due their charge a bent track in the tracking system. Dense electromagnetic showers are produced in the ECAL that also leak in the first part of the HCAL. Neutrons only deposit energy in the ECAL and HCAL, producing hadronic showers with big spacial extend. Having no charge, no track is seen. The shower topology points strait to the vertex where it was produced. Muons leave, due to their high mass at rest, only slightly bent tracks and pass the calorimeter system with little or no shower production. Electromagnetic showers produced by photons are mainly confined to the ECAL only pointing directly to the vertex. Charged pions leave a track in the tracking system and produce extensive hadronic showers in the ECAL and HCAL. The energy of a charged particles cannot only be measured by the calorimeter systems, but also by the tracking systems with higher resolution. Typical resolutions for different subsystems are listed in table 5.1.

Parton	Detector system	Energy resolution
Charged particles (X^\pm)	Tracker and vertex system	$10^{-4} \cdot E_{X^\pm}$
Photons (γ)	ECAL	$\frac{10\%}{\sqrt{E_\gamma}}$
Neutral hadrons (h^0)	ECAL / HCAL	$\frac{50\%}{\sqrt{E_{h^0}}}$

Table 5.1: Achievable parton energy resolution depending on the particle type. The best sub-system is chosen and the resolution is given. Taken from [51]

5.2 Particle Flow Algorithm

Hadronic calorimeters have, by nature, the worst energy resolution of all subsystems in a detector. The measured energy of a jet will be dominated by the uncertainties of the HCAL. As Figure 5.2 shows, particle energies of charged particles in a jet can be measured with higher precision in the tracker systems. Figure 5.4 illustrates the difference between classical calorimetry and PFA. The concept of the particle flow algorithm is to measure the energy deposition of each particle inside a jet. The detector subsystem with the highest resolution can be used to determine the energy of individual particles. The energy sum of the particle jet can be measured with higher precision than using only the calorimeter system. A high spacial resolution is needed to track each individual particle through the detector. e^\pm , μ^\pm , and h^\pm energies will be reconstructed already in the tracker which has a superior energy resolution, see table 5.1. The ECAL is mainly used for the reconstruction of γ and the ECAL + HCAL combination only reconstructs the energy of neutral hadrons h^0 . The energy of the jet is the

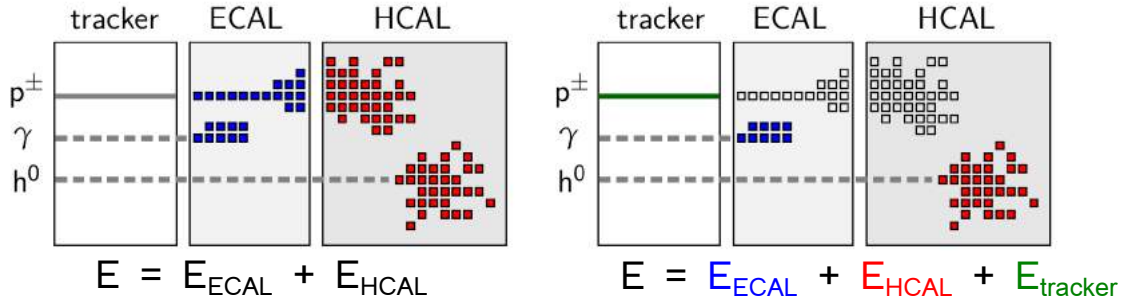


Figure 5.4:

Left: Classical calorimetry. E_{jet} is the sum of the energy measured in the calorimeter system.

Right: PFA approach. High spacial segmentation enables the separation of the energy deposits from particles showers and assign them to individual particles. The energy measurement from the subsystem with the highest energy resolution is used for the energy sum of the jet. [25]

sum of all particles reconstructed. The resolution can be parametrized as

$$\sigma_{jet} = f_{X^\pm} \cdot \sigma_{tracker} \oplus f_\gamma \cdot \sigma_{ECAL} \oplus f_{h^0} \cdot \sigma_{HCAL} \oplus \sigma_{conf} \oplus \sigma_{thr} \oplus \sigma_{loss}. \quad (5.1)$$

With the average weight f_X, f_γ, f_{h^0} of the particle type, σ_{conf} is the confusion term that deteriorates the resolution by wrongly assigning energy depositions to particles that have already been measured in another subsystem. σ_{loss} refers to energies from particles that are lost to detection. σ_{thr} are losses through energy depositions from particles under threshold that are not accounted for. To minimize σ_{conf} , a very high spacial resolution and imaging capability of the detector is needed. σ_{loss} is minimized by avoiding gaps and dead areas in the detector while a low threshold of ≈ 0.5 MIP insures a low σ_{thr} . Since only 10% of the particles are measured with the HCAL, σ_{conf} can dominate the detector resolution. A high spacial imaging capability can be more important than a high energy resolution in the HCAL. This idea has been already realized by the ALEPH detector [52] and been used in the e.g. CMS detector [53]. The spacial resolutions of the calorimeter systems were not high enough for tracking each individual particle. An Energy Flow Algorithm (EFA) has been implemented, subtracting for example all charged particle energies that were measured by the tracker from the deposition in the calorimeter. That way the impact of the bad energy resolution of the calorimeter on the overall energy resolution could be minimized. The EFA has been implemented only after the design and construction of these detectors. The goal of the ILD collaboration is that the PFA guides the design of the detector, especially the calorimeter subsystems developed by the CALICE collaboration.

5.3 The ILD detector

The ILD detector for the ILC project has been specifically developed to fullfill the requirements for PFA. A high imaging capability enables tracking of all particles in a jet. The layout

follows a classical detector design [15]. Figure 5.5 on the left shows a realistic view of the detector, while Figure 5.5 on the right depicts the single components.

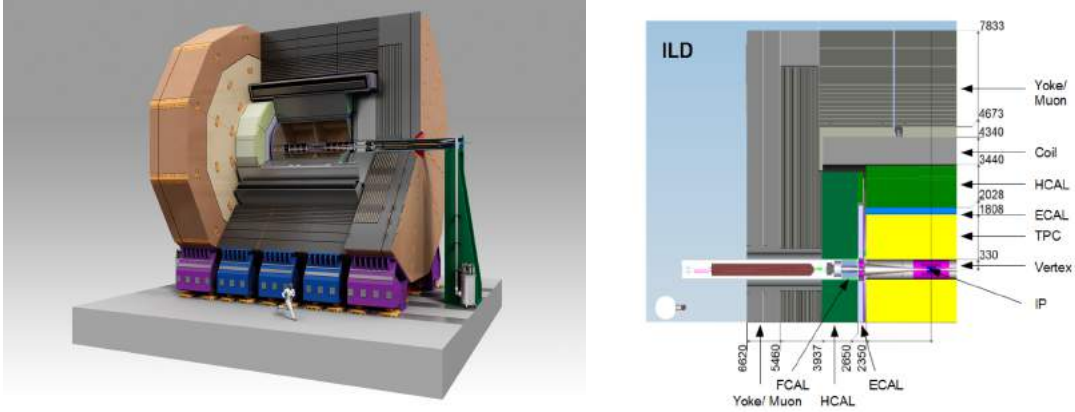


Figure 5.5:

Left: 3D picture of the ILD detector with a human Figure for size comparison.

Right: Quadrant view of the ILD. In the lower right with the interaction point (I.P.). Dimensions in mm [15]

The tracker system in the ILD consists of a high resolution vertex system close to the beam line and the combination of a silicon tracker and a **T**ime **P**rojection **C**hamber (TPC) that stretches to the calorimeter system. The ECAL and AHCAL are completely inside the large solenoid coil that provides a 3.5 T field. The iron return yoke is instrumented and doubles as a muon tracker and tail catcher for the calorimeter system.

In the following, each subsystem is presented shortly while a complete review can be found in the ILC TDR [15].

The vertex detector (in dark blue close to the I.P. in Figure 5.5 right) will be a 5 or 6 layered pixel detector in barrel geometry. The pointing resolution of the silicon pixel detector is designed to be $3\ \mu\text{m}$ to $6\ \mu\text{m}$ [54]. The main purpose is to pin-point the collision point and for heavy quark tagging. To distort the path and energies of the particles as little as possible, the material budget is aimed at $0.15\% X_0$ per layer.

The ILD silicon tracking system (in violet in Figure 5.5 right) is split into two parts: the inner tracker (SIT) and the outer tracker located outside of the TPC (see next paragraph), (SET). The silicon tracker forms a link between the Vertex detector and the TPC, providing precise space points, while also providing the link between tracking in the TPC and the calorimeter system. The tracking resolution will be ranging from $7\ \mu\text{m}$ to $50\ \mu\text{m}$ and the material budget per layer is $0.65\% X_0$.

The **T**ime **P**rojection **C**hamber (TPC, in yellow in Figure 5.5 right) is two large tubes filled with gas [55]. The ionized gas molecules produced from passing charged particles are accelerated with high voltages towards the ends of the chamber where their amplitude and time of hit is measured. TPCs transform the 3D position in space into a 2D + time space. An example for a TPC in use is the ALICE TPC [56]. The total material budget over the 1.8m of the TPC is 5% X_0 . The deposited energy can be measured with 5% and ≈ 0.1 mm in space.

PFA imposes new design strategies for the ECAL (in blue in Figure 5.5 right). Measuring only the contributions from γ and sometimes the beginning of showers from h^0 , the design has to focus on spacial resolution rather than energy resolution. It is designed as a sandwich calorimeter with an absorber providing small Moliere radius for better shower separation. Detection units smaller than the Moliere radius improve the separation further [57]. In the ECAL, tungsten ($X_0 = 3.5$ mm, $R_M = 9$ mm interaction length = 99 mm) is the choice for the absorber because it also keeps the ECAL small enough to fit inside of an affordable coil. It is planned to have 30 layers resulting in a thickness of $34 X_0$. The spacial resolution is 5×5 mm². Two main technologies are investigated: silicon based pads [58] and plastic scintillator strips [59]. To avoid dead areas the readout system is integrated into the active layers. The high density of channels require active cooling of the ASICs.

The design of the AHCAL (in green in Figure 5.5 right) is lead by the demands of PFA. The steel absorber is interlaced with either scintillator or gaseous detector based active layers. This thesis focuses on the scintillator option. The ratio of $\lambda_i = 17$ cm and $X_0 = 1.8$ cm in iron allows for a fine segmentation in X_0 while keeping the detector volume compact. The analog hadronic calorimeter AHCAL of the CALICE collaboration uses plastic scintillating tiles of $3 \times 3 \times 0.3$ cm³ with full energy readout per element. The **D**igital **H**adronic **C**alorimeter (DHCAL) does not read out any energy information but is segmented more finely reaching an unmet spacial imaging capability. The energy is measured by counting the number of hits and identifying the electromagnetic cores. The Semi-DHCAL has three thresholds on the deposited energy while keeping the fine segmentation. All three technologies are being tested with engineering prototypes scalable to a full ILD HCAL. More details on the AHCAL are described in the following Chapter and details on the DHCAL can be found in Chapter 12.

The foreseen magnetic field for the ILD is 3.5 T in 6.88 m in diameter and a length of 7.35 m. The instrumented return yoke is also the main mechanical structure of the ILD detector. The superconducting coil is similar to the CMS system and a description can be found in [60].

The muon detector system (in gray in Figure 5.5 right) is instrumenting the return yoke of the magnetic coil. It consists of thick iron absorber layers and 14 active layers with either

gas detectors or scintillator strips. The system doubles as tail catcher for the HCAL. The first layers are relatively densely spaced while the rear part is more spaced out.

5.4 Spatial optimization for an ILD HCAL

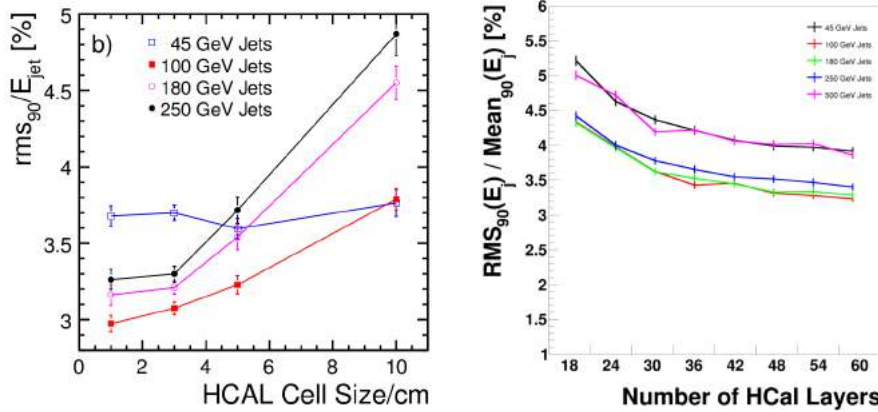


Figure 5.6: Particle Flow Jet energy resolution versus single cells size and number of layers Resolution versus cell size [15] Resolution versus number of Layers [61]

Detailed studies described in [61] and simulations in Figure 5.6 using the particle flow algorithm have been carried out in order to optimize the dimensions of the active material as well as the sampling in the z direction. A single cell size of $3 \times 3 \times 0.3 \text{ cm}^3$ resulting in the order of 10^6 channels for the whole system have been chosen. A finer structure will not provide significantly better resolution, whilst the greater amount of channels will affect greatly the overall system complexity and costs. The depth of the calorimeter was optimized for typical Jet Energies up to 250 GeV with a depth of 48 layers of stainless steel corresponding to $6 \lambda_i$.

Chapter 6

Analogue Hadronic Calorimeter (AHCAL) Technology

The Analogue Hadronic Calorimeter (AHCAL) is a concept for a highly granular hadronic calorimeter that seeks to fulfill the requirements that the Particle Flow Algorithm (PFA) reconstruction demands as formulated in chapter 5.4 and chapter 5.3. The concept of the sampling calorimeter is based on a stainless steel absorber in a sandwich structure with plastic scintillator tiles with individual SiPM readout. A physics prototype (operated 2006 - 2012) showed the feasibility of the concept and provided extensive studies of shower shapes and PFA benchmarks in data and simulations [62]. The physics prototype was not scalable to a full size ILD AHCAL. The second generation engineering prototype focuses on full compliance with the ILD specifications. A hadronic calorimeter for particle flow needs to sample hadronic showers and particles with high spatial resolution. Non instrumented areas and cracks inside the hadronic calorimeter need to be strictly avoided. This also demands the placement of the detector inside the magnetic coil and therefore a very dense calorimeter. For high energy resolution and good tracking efficiency, the calorimeter needs to sample deposited energies from single MIP to several 100 MIP in the dense electromagnetic showers. The AHCAL is designed as a sampling calorimeter with a stainless steel absorber and scintillating tiles read out by SiPMs as active material. The detection elements are designed to be transversally in the order of the Moliere radius in steel (1.7 cm) and longitudinal in order of the radiation length X_0 . Five interaction lengths (plus one from the electronic calorimeter) with a sampling ratio of 20:3 cm minimize leakage of shower while maintaining a realistic coil size. The scintillating tiles are read out with SiPMs which are insensitive to magnetic fields.

6.1 Mechanical structure of the ILD barrel

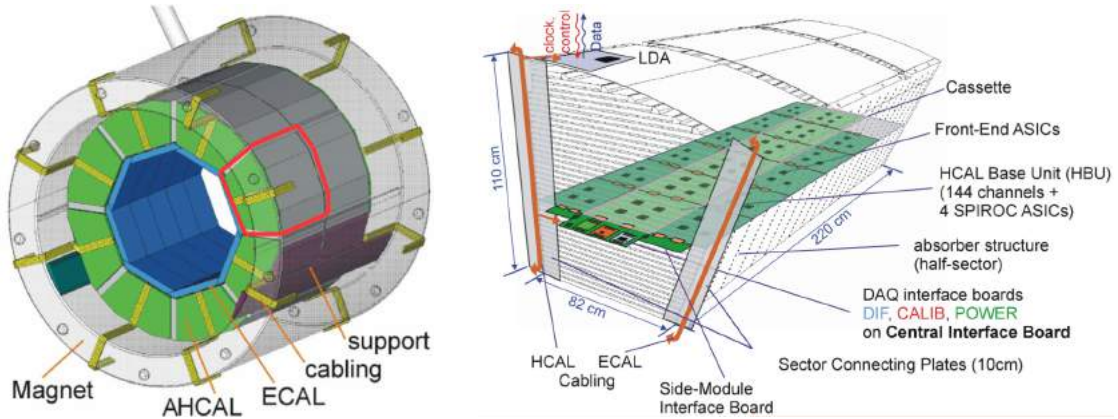


Figure 6.1: *Left*: The ILD barrel with the ECAL (blue), the AHCAL (in green), and the magnetic coil (gray). The yellow lines represent the foreseen cabling. The ECAL and AHCAL are situated inside the magnetic coil to minimize dead material. The barrel is segmented into 16 wedges.

Right: A half wedge of the AHCAL. 48 layers of self-supporting stainless steel absorber structure that host removable cassettes that contain the active material and electronics. A cassette contains 18 base units (HBU).

The AHCAL barrel is divided into two rings, each 2.16 m long divided in 16 Modules as shown in figure 6.1 left. The steel absorber allows to build a self-supporting structure. Each wedge (Figure 6.1 right) is a sampling structure with 48 layers of 16 mm thick steel absorber and 9.9 mm gaps for the active material, electronics and their support. The gap between the steel absorber in each layer contains a 5 mm thick removable cassette. Inside the cassettes are 18 single HCAL base units (HBU, see section 6.2) with a size of $36 \times 36 \text{ cm}^2$ each. The cassettes are removable and can quickly be repaired or replaced during maintenance. The HBUs are grouped into single slabs. A lab prototype of a complete slab can be seen in figure 6.2. HBUs contain the active material, a $3 \times 3 \times 0.3 \text{ cm}^3$ scintillating plastic tiles read out by SiPMs. The single tiles are optically isolated from each other to prevent scintillating light to pass from one tile to another. This improves the single particle tracking and shower separation. Clip-on flex-lead PCBs connect each HBU inside a slab with 6 HBUs. Three slabs are inside a cassette [15].

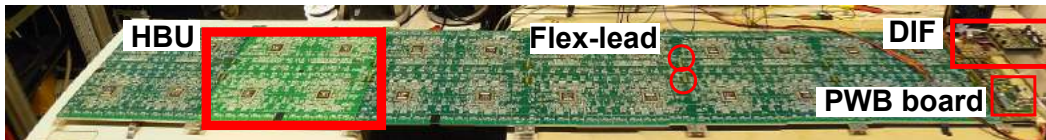


Figure 6.2: AHCAL slab:

Six base detector units form a 2.16 m long AHCAL slab. The 24 chips are read out sequentially by the DIF board in the right end of the picture. The single base units are connected with flex-lead connectors plugged into ultra thin push connectors.

6.2 HCAL base unit (HBU)

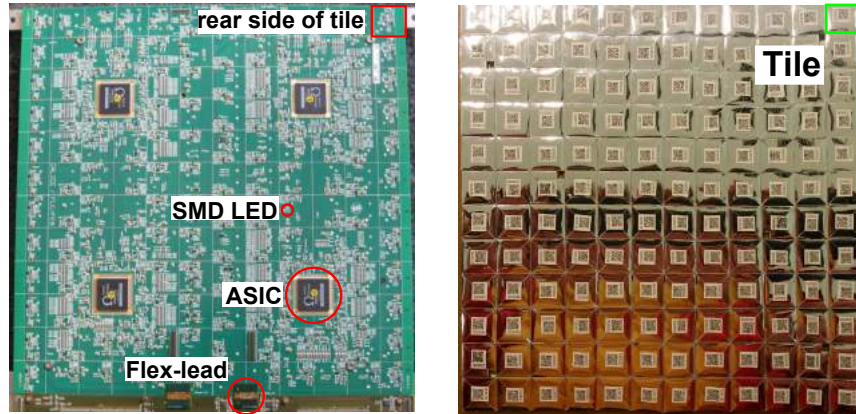


Figure 6.3: A single HCAL base unit (HBU):

A single PCB with $36 \times 36 \text{ cm}^2$ with four ASICs form an HBU.

Left: All components needed for operation including LEDs for calibration are mounted directly on the PCB. The flex-leads in the bottom of the image are the only connection for power supply, slow control, and readout. *Right:* Rear side of an HBU with 144 (36 per chip) wrapped scintillating tiles from the University of Hamburg. The tiles are mounted directly on the HBU and form a complete detector unit that is easy to remove and handle.

The HCAL Base Unit (HBU) is a $36 \times 36 \text{ cm}^2$ PCB equipped with 4 readout chips, each one reading the output of 36 calorimeter channels, for a total of 144 channels per HBU. Each channel has an LED for calibration of the SiPM on each detection unit with a programmable light intensity. The PCB can be cut in half to leave no non-instrumented areas in the wedges. A special 6 layer PCB construction of 0.8 mm with a sink for the 1.4 mm high ASIC has a thin profile to fit in the gaps. The HBU is currently used in revision HBU2 and HBU3 with the changes addressing only an improved LED driver and extended features for power management. No difference in the quality of the recorded data could be seen. The rear side in figure 6.3 of the HBU is equipped with 144 scintillating tiles read out via SiPMs directly attached to the tile and soldered to the HBU.

6.3 Readout ASIC - Spiroc2b

The Spiroc2b is a dedicated very front-end ASIC for the AHCAL designed by Omega [63]. The chip was designed specifically for SiPM operation and low power consumption (Aim: $25 \mu\text{W}$ per channel) as well as a package to take up minimal space inside the detector, see figure 6.4. It is a versatile 36 channel chip meant to provide auto-triggered channel-wise energy and time measurements. The readout of an ILD-like calorimeter requires an integrated readout for thousands of channels to avoid a large amount of cables and dead space inside the detector volume. The electronics need to accommodate for a variety of different batches



Figure 6.4: The Spiroc2b readout chip, a dedicated very front end readout chip designed by Omega [63]. The chip is hosted in a low profile casing. A ditch in the PCB of the HBU lowers the overall height of the HBU to 5.4 mm.

and a variety of SiPMs. The ILD baseline is a completely self-triggered detector. The electronic need self-triggered single channels. A 2 ms bunch train from ILC will have several thousand collisions and can cause subsequent hits in the same channels. A readout between the collisions is not feasible so analogue storage is needed. Covering energies from single MIP depositions to track muons to 100 MIP for shower cores requires a huge dynamic range. The Spiroc2b provides channel-wise bias voltage adjustment and readout for 36 SiPMs with an adjustable amplifier. A low voltage CMOS technology and intelligent power management make a power consumption of $25 \mu\text{W}$ per channel possible. Figure 6.5 gives an overview of the signal processing in the Spiroc2B. The ASIC is self-triggered with a channel-wise adjustable threshold and provides time stamps with a design resolution of 100 ps. The dynamic range for energy measurements is 12 bit. Two readout lines with different pre-amplification gains (factor 10) ensure the required dynamic range. A 16 cell deep analogue memory stores events during a bunch crossing before digital readout. Operational voltages for the ASIC and the global bias voltage are provided by external electronics: the CALIB board and Power Board (PWB) which are discussed in chapter 8.

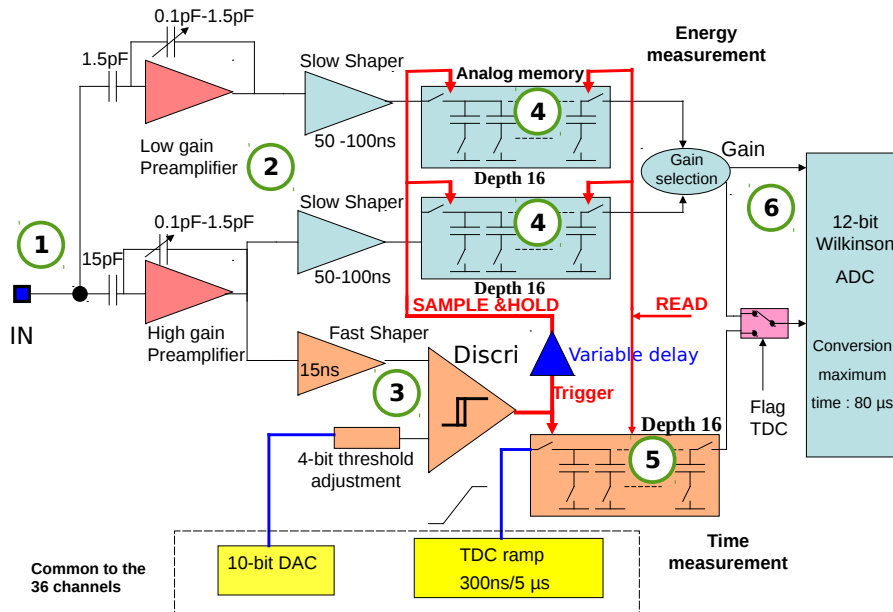


Figure 6.5: Block diagram of the Spiroc2b readout chip

- 1: The capacitively decoupled signal from the SiPM is split between high and low gain amplification (factor of 10). The amplifiers of all channels can be set from 0.1 pF to 1.5 pF with 8 bit resolution.
- 2: Both signals are passed through a slow shaper with a variable integration time of 50 ns-100 ns.
- 3: The high gain signal is additionally fed into a fast shaper (15 ns integration time). This signal is compared with an adjustable (4 bit) threshold discriminator which provides the trigger for the channel.
- 4/5: The integrated signal of the slow shapers are stored into three 16 16 units deep analogue memory cells with an adjustable sample and hold time (25 ns-175 ns).
- 6: Digitization with a Wilkinson ADC. Two of the three memory cell arrays can be selected for readout.

6.3.1 Internal adjustment of SiPM bias voltage

The bias voltage for all 36 channels of an ASIC is provided by an external power board, see chapter 8.1. Additionally, the Spiroc2b features individual channel wise 8 bit voltage adjustment. A design voltage from 0 V - 5 V can be subtracted by the chip from the global voltage. Every channel shows a different behavior and voltage, for further details see section 8.

6.3.2 Trigger

The ILD concept features self-triggered detector units. A signal over threshold trigger starts the signal acquisition and provides a time stamping for the event. The detector can be triggered externally with a trigger signal for all channels or with an internally generated pulse, when an analogue signal passes the trigger threshold. For normal operation, the detector is running in a self-triggered mode. During a full train with collisions of 2820 bunches, the same chip is rarely hit multiple times so a memory buffer of only 16 cells can be used. The trigger signal needs to be generated before the actual energy measurement. If the energy signal fed

to a fast shaper with 15 ns integration time passes a given threshold, the channel triggers and starts the actual energy measurement. Every trigger saves the current selected values into the memory cells and increases the pointer to the next memory cell. If all memory cells are written, the Spiroc2b passes a signal to the DIF which triggers a detector wide readout.

Auto triggering (AT) In normal detector operation, the Spiroc2b is internally triggered (AT) via a logical OR between all 36 channels. The signal for each channel is split into two amplifiers (see **1** in figure 6.5). After the high gain amplifier the signal is split further. One line goes to a separate fast 15 ns shaper (see **3** in figure 6.5). A threshold discriminator provides the trigger signal. It is important to note that chip does not trigger on the recorded signal which is passed through a different shaper. Each channel passing the threshold carries a hit bit flag in the data. If any of the channels has a signal over threshold, all channels are saved to the memory buffer. This is an intermediate feature of the Spiroc2b and will be changed to only save the value of the triggered channel in the next generations of the Spiroc2b ASICs. The threshold can globally be set for all channels with a 8-bit register, and additionally, can be regulated via a channel-wise 4 bit register. Using the single-channel register in the current chip design influences the operation of the neighboring channels, causing baseline shifts, see [64] (section 5.4).

External triggering (ET) In external triggering mode (ET) all 36 channels can be triggered from an external signal on the DIF. In this mode, the AT is not disabled but can be disabled by setting a high threshold. This mode is mainly used for calibration purposes like pedestal runs or SiPM gain calibration using the LED system.

External validate In test beam environments the detector will not always run synchronous with the beam. Noise from the system would fill up all available memory and trigger time consuming readouts. The data taking efficiency would be severely limited. A separate signal from the DIF can prohibit the increase of the memory cells pointer if provided within the same cycle (same Bunch Crossing ID). Triggered events without an external validate signal are overwritten with the next event. The external validate system has a dead time of around 200 ns at the end of each cycle. All triggered events are validated regardless of a present external validate signal. In order to use this feature of the ASIC and accommodate for low events rates like CERN and DESY test beams, the clock is reduced from 5 MHz to 250 kHz.

6.3.3 Energy measurement

The deposited energy of a particle passing through the scintillator is measured by the charge of the SiPM signal generated by scintillating light. In a self-triggered detector, a trigger signal must be provided before the energy is measured. To provide a higher dynamic range

the signal is split into two amplifiers: a low gain amplifier and a high gain amplifier with roughly 10 times higher amplification. If a channel triggers, then the information is stored in a digital memory. The signals from both amplifiers pass into slow shapers that transform the charged pulse into a 150 ns long signal. On each signal a sample and hold circuit ([65], page 220) with variable hold time after the provided trigger transfers the signal into the analogue memory. After each trigger the pointer to the memory cell is increased. A variable threshold discriminator on the signal stores a so called gain-bit per signal. It is later used to select the appropriate memory cell either of the high or low gain amplifier for readout.

6.3.4 Time measurement

The time of a hit is measured using an analogue voltage ramped during a chip cycle. Chapter 11.1 provides a more detailed description of the function and only a short introduction is given here. With each cycle of the Spiroc2b, a voltage is ramped up. Two voltage ramps with different characteristics are produced to avoid dead time in a new cycle. If a trigger occurs in a channel, a sample and hold transfers the actual voltage into a memory cell array. The cells are read out the same way as the energy information. A channel triggers only on the first hit over the threshold produced during the 15 ns shaping time in the fast shaper. Consecutive hits during the delay of the slow shaper are added up for the energy information. The energy measured in a triggered channel is therefore the sum of all hits that occurred during the sample and hold time. With the 12 bit ADC the theoretical resolution is 100 ps. In order to use all features of the ASIC and accommodate for low events rates like CERN and DESY test beams, the clock is reduced from 5 MHz to 250 kHz. This reduces the theoretical time resolution to 0.5 ns.

6.3.5 Readout of the analogue memory cells

If the memory buffer is full or an external trigger is provided, the memory cells are read out. The three memory cell arrays, two from the energy measurement and one for the timing information, are read out via the same path. Only two of the three memory cell arrays can be digitized during readout. A selector is programmed when the chip is initialized. If only one energy measurement is digitized the gain bit flag determines which amplification path was used. The analogue content of each memory cell of an array is digitized sequentially via one Wilkinson ADC [66, p. 315] per array. A Wilkinson ADC discharges a memory cell over a resistor and measures the time over threshold. 32 ADCs convert charges simultaneously and depending on the charge, the readout can take up to $100\mu s$ for one memory cell. If the memory is full, 32 runs or 3.2 ms are needed for the readout of two memory cell arrays.

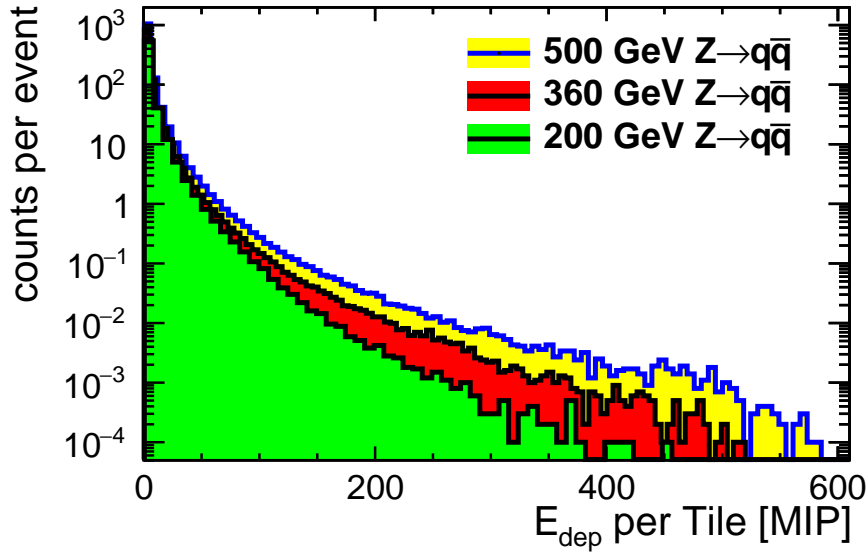


Figure 6.6: Full ILD barrel simulations done by Lan Tran.

Hit energies per event in $3 \times 3 \times 0.3 \text{ cm}^3$ plastic scintillator tiles normalized to the number of Events.

100 GeV hadronic jets in green.

180 GeV hadronic jets in red.

250 GeV hadronic jets in yellow.

6.4 SiPM and Scintillator system

The single detection units in the AHCAL are based on $3 \times 3 \times 0.3 \text{ cm}^3$ plastic scintillator tiles read out by a SiPM. To estimate the dynamic range of hits, the occurring hit energies per tile in a full ILD simulation are shown in figure 6.6. In 500 GeV hadronic jets, energies over 70 MIP per cell occur less than once per jet. Truncation of the higher energies have also almost no impact on the single particle resolution as described in [67]. A dynamic range up to 100 MIP is sufficient to achieve the required energy resolution for hadronic jets. To track single muons through the calorimeter, a high efficiency for MIPs over 95% is needed as well as low noise at a threshold around 0.5 MIP. The tiles should show a reasonable homogeneous response over the whole surface. In [68] it is demonstrated that the impact of gaps between the tiles (up to 1.5 mm) and inhomogeneities in the 30% level, over 10% of the surface are irrelevant with respect to the energy resolution. The detector is foreseen to be not actively cooled. For a simple operation, environmental changes like temperature should not have a big influence on the detector operation. The production of the units need to be affordable and feasible on the scale of the needed 10^6 units.

6.4.1 SiPM

The scintillation light produced by plastic scintillators is in the blue region [69]. In order to avoid additional wavelength shifting components a blue sensitive SiPM is favored. The noise at half a MIP response (in a typical $3 \times 3 \times 0.3\text{cm}^3$ scintillator 5 - 40 pixel) has to be low. The combination of low single pixel DCR and correlated noise XT_{corr} (afterpulse probability and pixel crosstalk) should result in a sub Hz noise rate. The Spiroc2b ASIC has additional requirements for a SiPM to be met. A signal of at least $500000 e^-$ per photo electron and a setting for 20 ADC channel as a gain result in a reasonable signal to noise ratio for single pixel spectra. The desired 100 MIP resolvable energy needs to be outside of the saturation region of the SiPM. All parameters of the SiPMs need to have a low spread in order to simplify the calibration and settings of the detector.

6.4.2 Scintillator

Plastic scintillators should have a fast scintillation time (to provide an accurate time-stamp) and long attenuation length (to avoid inhomogeneities over the surface). A fast scintillator assures a fast, high peak on the measured signal from the SiPM. A long attenuation length much greater than the tile dimensions enables a uniform response over the whole tile. The tile has to be coupled to the SiPM in way to ensure the uniform response over the whole tile area. The assembly needs to be optimized for industrial production.

6.4.3 Wrapping

The plastic tiles need an enclosure to prevent light from passing from one tile to the other. The smaller the optical crosstalk (XT_{opt}), the better the separation of the energy hits. An enclosure will need to be feasible for industrial production of tiles and ensure an easy mounting on the HBU. The material choices range from paints and evaporated metal to plastic and paper wrappings.

Chapter 7

Tile and SiPM system of the University Hamburg

In 2014 the CALICE collaboration has started the production of a new prototype of the AHCAL aiming to test the time development of hadronic showers. The University of Hamburg has produced about 2000 tiles-SiPM detector units to equip four layers of the prototype. This chapter describes the novel design developed and investigates various method of coupling the SIPM to the tile and the wrapping of the tile. The goal was to establish a technology and production method suitable for mass production of several thousand units.

7.1 Mass testing setup

A mass testing setup for measuring the main features and figures of merit of the University Hamburg tile and SiPM system has been commissioned. The response signal of the tile to minimal ionizing particles as $R = \frac{MPV}{G}$ with MPV being the signal response and G the gain of the SiPM, see chapter 4.6.1. The breakdown voltage V_{bd} , DCR and correlated noise XT_{corr} of the SiPM are measured with a high precision of 1% as well as the optical crosstalk. XT_{opt} . A motor driven sledge with six tile holders seen in figure 7.1 moves the tiles sequentially under a ^{90}Sr source. Each holder features a decoupling circuit (detail of the circuit in section 7.1.2, figure 7.8) and a glass fiber with blue/UV light from LEDs with a peak wavelength of 405 nm. All tiles are connected to a common programmable power supply (Keithley 6517B, 10 mV precision). The setup is in a temperature controlled box which can slowly regulate the temperature from 16°C - 30°C with a precision of 0.3° to measure the breakdown voltage shift in $\frac{mV}{\text{C}}$ for a few samples. The measurements of tiles also served as calibration reference for a large scale tile calibration setup from the University of Heidelberg based upon a Laser system described in [70]. The signals of the six SiPM are simultaneously measured with 10 times amplification (CAEN N412) with a QDC (CAEN V965, 16Ch dual-range QDC) charge to digital converter with an integration window of 180 ns as depicted in

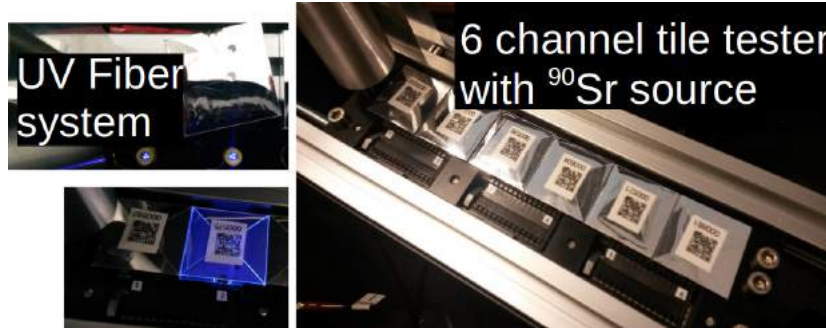


Figure 7.1: High precision mass testing setup.

Left: UV/Blue light fiber system with 6 channels for gain and optical crosstalk measurements.

Right: Motorized sledge that moves the tiles sequentially under a ⁹⁰Sr source for tile response measurement.

figure 7.2, which results in a 98% fraction of the total charge. A trigger logic generating the integration gate switches automatically between measurements with the ⁹⁰Sr source and a pulse generator (SRS DG645) controlling the LEDs. For details of the ⁹⁰Sr trigger system with two triggers see section 7.1.2. The timing of the trigger system is shown in figure 7.2 on the right. The electronics that generate the integration window delays the trigger signal around 40 ns with respect to the triggered tile. To achieve an effective gate of around 140 ns the tile under test signal is delayed for 80 ns after the gate pulse with 16 m of RG-50 cables separately for each channel. The gate has to precede the actual windows by 20 ns for the operation of the Caean QDC. Another 20 ns were added to account for the substantial trigger jitter caused by the time slew effect (see figure 11.16 in chapter 11.2.3).

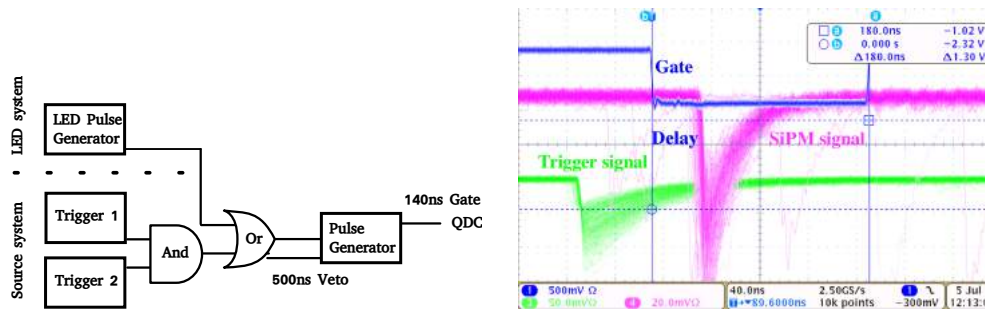


Figure 7.2: *Left:* Trigger-system of the mass testing setup

The coincidence of the source trigger (details see section 7.1.2) or the pulse generator driving the LEDs can trigger the main pulse generator via a logical OR. A 180 ns gate is generated to operate the QDC while a 500 ns veto gate prohibits consecutive triggers from after-pulses and unstable states in the QDC.

Right: The timing of the trigger signal measured by a scope. In violet the SiPM signal from the measured tile. The 180 ns long integration gate in blue is triggered by the trigger tile in green.

7.1.1 SiPM measurements

The figures of merit are measured in parallel on all six SiPMs for fast characterization. For the Ketek PM1125 SiPM the scanned voltage range of 32 V-29.5 V. A temperature of 22°C

was chosen as the reference temperature for all measurements.

Gain and Breakdown Voltage

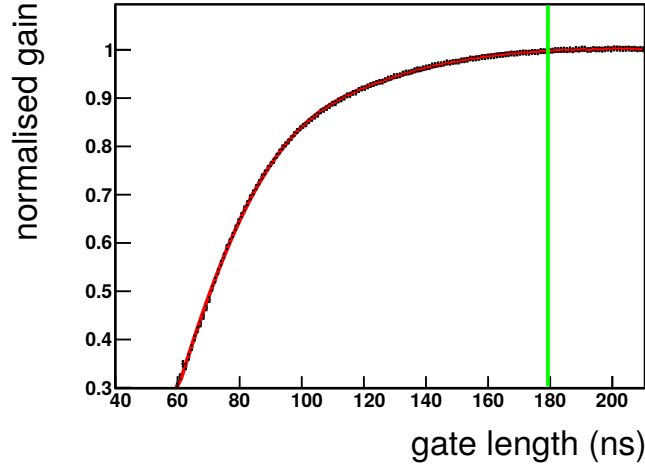


Figure 7.3: Scan of the integration window to determine the true pixel charge (gain) of the SiPM). A gate of 180 ns was chosen as a compromise for good signal to noise and insensitivity to trigger jitter. 98% of the true charge is measured this way. The conversion from ADC units to units of elementary charge is 1.56×10^{-4} (QDC and amplifier manual).

To determine the gain of the SiPM in equation 4.2, a charge spectrum with at least 60.000 entries is measured. The single peaks correspond to the amounts of fired pixel of the SiPM, see the black curve in figure 7.4. The first peak refers to a charge of no pixel fired (electronic baseline, B_{C0}). To determine the gain slope and breakdown voltage V_{BD} , equation 4.1 spectra at 11 different voltages are fitted with a multi-Gaussian function to extract the peak-to-peak distance (gain of the SiPM).

$$F(x) = \sum_{i=0}^N A_i \times e^{-\frac{x - (\mu_0 + i \cdot G)}{2\sigma_i^2}}; \quad \begin{array}{l} \mu(0) = \text{Position of first considered peak} \\ N = \text{Considered peaks} \\ A_i, \sigma_i = \text{Free fit parameters} \\ G = \text{Gain} \end{array} \quad (7.1)$$

The single Gaussian peaks sigmas are left as fitting parameters to account for after-pulses distorting the Gaussian shape of the peaks. The distance of the peaks (gain) are fitted with one parameter. Only peaks over 20% of the highest peak are considered as shown in figure 7.4. To determine the temperature dependency the measurements were repeated at five different temperatures for a subsample of a the SiPMs. The voltage and temperature dependency of the gain can be parametrized as

$$G(V, T) = \frac{dG}{dV} \cdot (V - V_{bd}(T)). \quad (7.2)$$

The extrapolation of the gain versus bias voltage to zero yields the breakdown voltage $V_{bd}(T)$ with an accuracy of 30 mV.

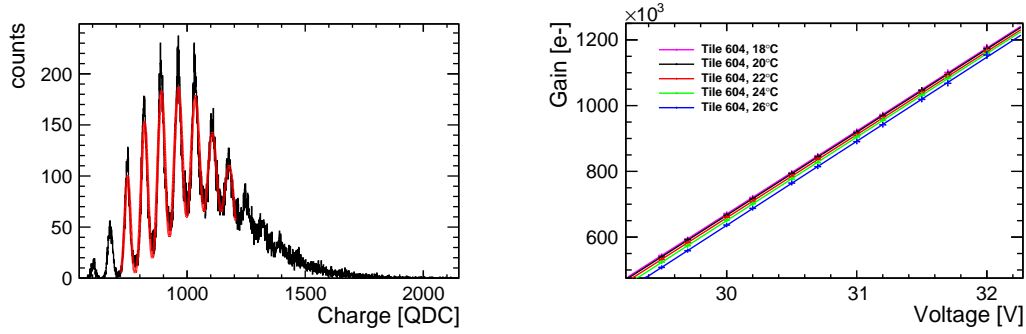


Figure 7.4:

Left: Multi-Gaussian fit of a the gain spectrum at 4.2 V over-voltage

Right: Measured gain at different temperatures for a sample SiPM (#604)

DCR and correlated noise XT_{corr}

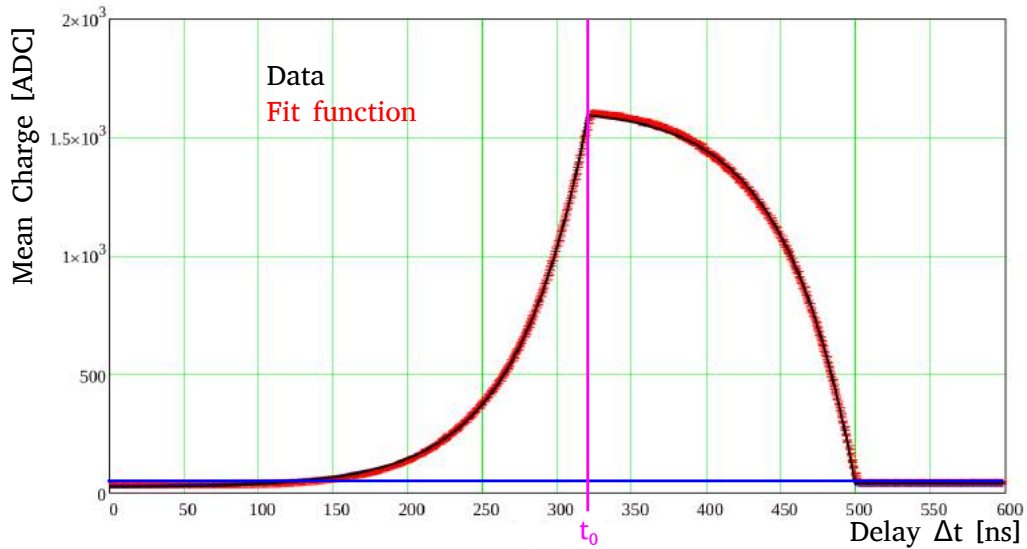


Figure 7.5: Delay time scan of the integration trigger to determine t_{gate}^{eff} . The integration window is moved in time with respect to the TuT signal. The TuT is illuminated with an LED power and the mean of the distribution plotted against the delay time of the integration trigger. In black the data and in red the fit. If the SiPM pulse precedes the gate (delay of 100 ns), a smaller mean value than the pedestal B is observed, which is caused by the AC coupling of the SiPM readout. The effect on the measurements is further discussed in section 7.1.2 with B_{C0} .

For the measurement of XT_{corr} it is important to determine the correct effective trigger window length used for the measurement. Partial discharges and incomplete signals that are partly measured within the integration gate have to be taken into account. Following the

definition in [71] the three functions

$$Q(\Delta t) = \begin{cases} Q_0 \cdot e^{\frac{\Delta t}{\tau}} \cdot (1 - e^{-\frac{t_{gate}}{\tau}}) & \text{for } \Delta t \leq t_0 \\ Q_0 \cdot (1 - e^{-\frac{t_{gate}-t}{\tau}}) & \text{for } t_0 \leq \Delta t < t_{gate} \\ 0 & \text{for } \Delta t \geq t_{gate} \end{cases} \quad (7.3)$$

are fitted to the mean amplitude versus the delayed signal in figure 7.5. The effective gate length for measuring the SiPM XT_{corr} at a threshold of 0.5 pixel fired is then defined as

$$t_{gate}^{eff}(0.5 \cdot MPV) = t_{gate} + \tau \cdot \ln(1 - e^{-\frac{t_{gate}}{\tau}}) \quad (7.4)$$

. The resulting t_{gate}^{eff} is $179 \text{ ns} \pm 1 \text{ ns}$. The dark count rate (DCR) and the correlated noise

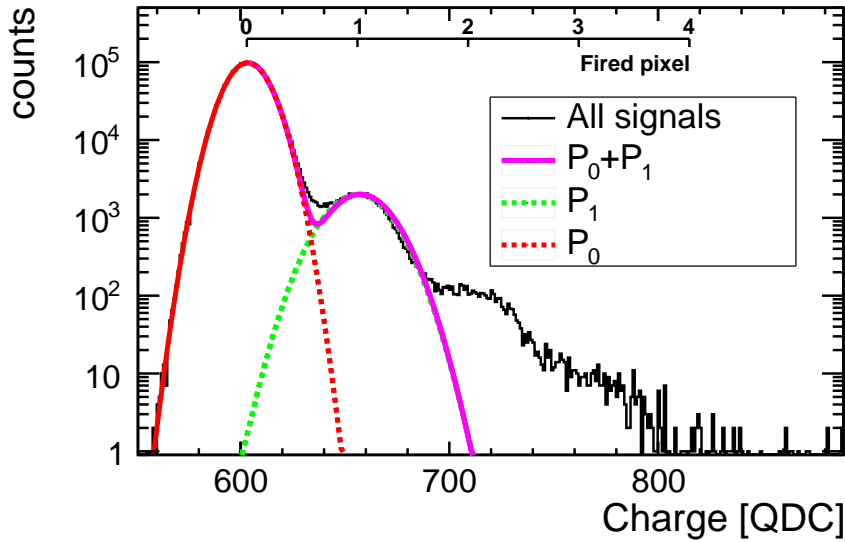


Figure 7.6: High statistics pedestal spectra with P_0 (red, no pixel fired) and P_1 (green, one pixel fired).

(XT_{corr}) is calculated from high statistics pedestal measurements. In this work XT_{corr} combines pixel crosstalk and after-pulses as correlated noise since they cannot be distinguished with the measurement method used. At different voltages the LED is switched off and data taken with a random trigger window. Assuming that the occurrence of dark counts can be described by Poisson statistics, $P_0^n(t_{gate}^{eff})$ is given by

$$P_0(t_{gate}^{eff}) = e^{-DCR \cdot t_{gate}^{eff}} \rightarrow DCR = -\frac{\ln(P_0^n(t_{gate}^{eff}))}{t_{gate}^{eff}} \quad (7.5)$$

for a gate length t_{gate}^{eff} . P_0^n is the normalised fraction of events with pulse charges corresponding

to no pixel fired. The correlated noise probability is obtained from

$$XT_{corr} = \frac{\sum_{k=2}^{\infty} P_k^n}{P_1^n} = \frac{1 - (P_0^n + P_1^n)}{P_1^n}; \quad \begin{array}{l} P_0^n = \text{Fraction of events with no pixel fired} \\ P_1^n = \text{Fraction of events with one pixel fired} \end{array} \quad (7.6)$$

as the ratio of events with more than one pixel fired to one pixel fired. This measurement will include after-pulses occurring during the integration window (correlated noise). Due to the low DCR of the SiPM and the high dynamic range of the setup, the electronics pedestal can not be separated well from the remaining spectrum. The method used in this work is shown in figure 7.6. The electronic pedestal and the one pixel fired distribution (pink line in figure 7.6) is fitted with the sum of two Gaussian functions at a peak to peak distance determined by the gain measurement (7.1.1). P_0 and P_1 are respectively the integral of the first and second Gaussian function from the fit.

7.1.2 Tile response measurement

The response is defined as the most probable value of a spectrum induced by MIP divided by the gain:

$$R(V, T) = \frac{MPV(V, T) - (B_{C0}(R) + P(V, T))}{G(V, T)}; \quad \begin{array}{l} R(V, T) = \text{Response to MIP} \\ P(V, T) = \text{SiPM pedestal} \\ G(V, T) = \text{SiPM gain} \\ B_{C0} = \text{electronic baseline (zero charge)} \end{array} \quad (7.7)$$

In this setup a baseline shift, B_{C0} has to be taken into account, depending on the rate and amplitude of the signal. In the following the complete method for determining the response is presented. Since the rate of MIP as cosmic muons is too low for the single tile calibration the setup has to mimic a minimal ionizing particle (Muon with 0.37 GeV/c) with a well defined energy deposition. The goal of the calibration setup is to mimic the behavior of a MIP particle using a ^{90}Sr source.

Electronic baseline B_{C0} shift

The SiPM signal is decoupled from the high voltage power supply via a blocking capacitor. The signal from the SiPM causes a significant baseline shift in the decoupling circuit (figure 7.8), depending on the event rate and amplitude. Capacitive decoupling transfers no energy so an infinite integral over the signal must be zero. This causes a microscopic, slowly decaying undershoot after a signal. The buildup of signals with higher rates causes a shift in the electrical baseline depending on frequency and amplitude of the signal over the 180 ns long integration window. This effect is observed in SiPM characterization studies with AC coupling like [71] when SiPM signals precede the integration gate by a short time interval (< 100 ns). The ^{90}Sr source with collimator (several 1000 events per second) causes a signifi-

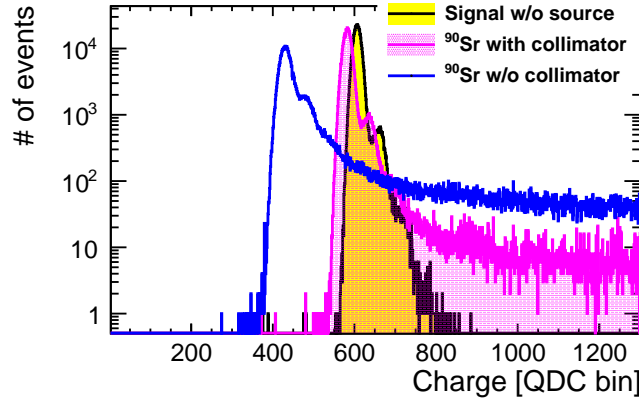


Figure 7.7: Charge spectra, randomly triggered with 1 MHz at different particle rates. The signals from β^- particles of the collimated ^{90}Sr source and collimator (pink) cause a significant baseline shift compared to a spectra without the ^{90}Sr source (black/yellow). The shift increases when the collimator is removed and therefore the particle rate is increased (blue).

cant shift as seen in figure 7.7. When the tile is positioned under the ^{90}Sr source a separate pedestal run with a random trigger is recorded. The main peak position corresponding to no charge is determined with a highly constrained Gaussian fit to account for this shift before each measurement of the response.

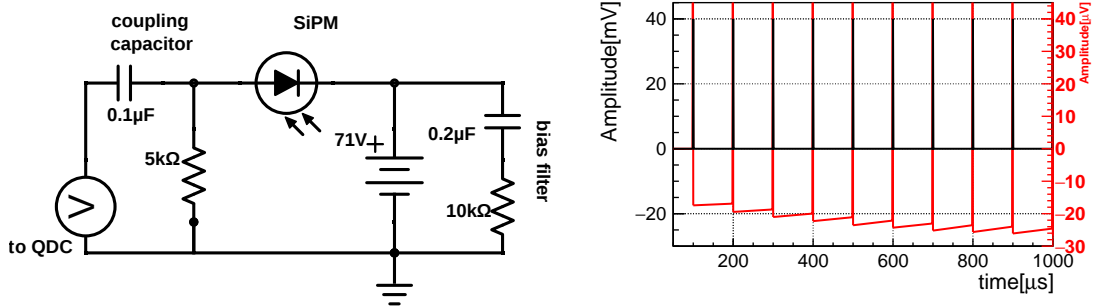


Figure 7.8: Simulation of the baseline shift with AC coupling. *Left:* The AC coupling circuit used in the setup is simulated with NI MultiSim. A pulsed current source mimics a 2 ns long SiPM pulse. The bias filter acts as a high pass filter for HF signals on the provided voltage. *Right:* A 40 mV pulse with 10 kHz repetition rate is simulated and the output (in black) to the QDC measured. The signal magnified 10^3 times (in red) shows a negative baseline shift per pulse which accumulates with consecutive pulses. The baseline shift is dependent on the rate and the amplitude of the signals.

Trigger system

For energy calibration in the lab a 7 MBq Strontium 90 source is used. ^{90}Sr and its decay products, ^{90}Yt and ^{90}Zr , show a broad energy spectrum with several peaks. The trigger setup used is shown in figure 7.10 on the left. An aluminum collimator of 4 cm length and a 3 mm hole constrain the angular distribution of the β^- particles on the tile under test (TuT). The

collimator also radiates photons via Bremsstrahlung into the TuT and broadens the energy spectrum. The energy spectrum does not fully follow a Landau Gaussian convolution. The

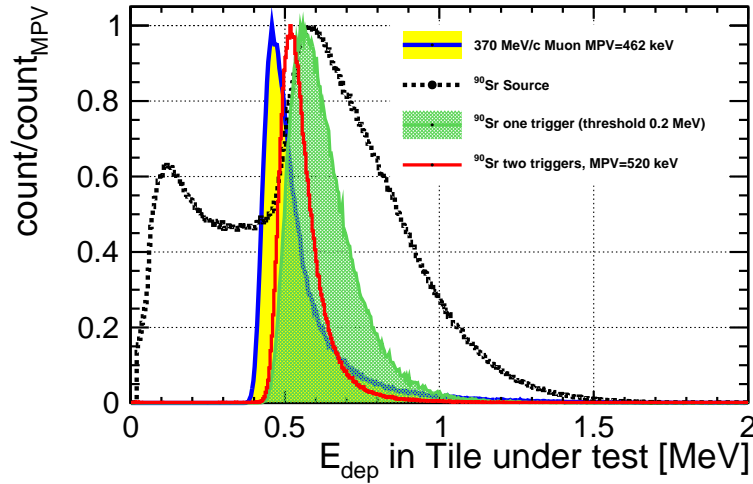


Figure 7.9:

Simulations done with Geant 4.10.p02

Comparison of energy deposition in a 3 mm plastic tile from a MIP (blue/yellow, 370 MeV/c Muon) and from a ^{90}Sr source with different trigger methods. The energy deposition from the ^{90}Sr source (in black) has a low energy component that together with electronic and SiPM noise could mask the main peak of the distribution and is not suitable. Even collimated electrons from a ^{90}Sr source will be deviated inside the tile and broaden the distribution. A setup with a single trigger tile (in green) is dependent on the threshold and the response of the trigger tile. A double trigger (in red) provides a well defined independent energy calibration using two trigger tiles.

trigger system consists of two 3 mm plastic tiles from the production line placed under the TuT. If the first trigger is used alone it excludes electrons that were stopped or deviated inside of the TuT and would lead to a broader distribution, see figure 7.9. In the past a similar setup was used to calibrate 5 mm tiles for the physics prototype where a smaller difference between the MPV was observed, see also [62]. The MPV of the deposited energy in the TuT depends on the threshold setting of the single trigger. Particles that stop in the single trigger deposit energies higher than the minimal ionizing value in the TuT. They are favored by a higher threshold setting. This threshold dependency does not provide a well defined energy deposition in the TuT without extensive calibration of the trigger system. The coincidence of the two trigger tiles provides a trigger threshold independent trigger. The usage of a second trigger also reduces dark count noise from the trigger SiPMs and gives tighter constraint on the angular distribution of the particles. The coincidence rate is 40 times lower than the single trigger rate at 0.2 keV threshold and it would take an hour to gather enough statistics on the TuT. In order to complete the calibration of a single tile in a feasible amount of time, only the first trigger is used (≈ 100 Hz rate). Using data with both triggers enabled are taken to extract the ratio of the MPVs. In order to extract a calibration constant the trigger threshold

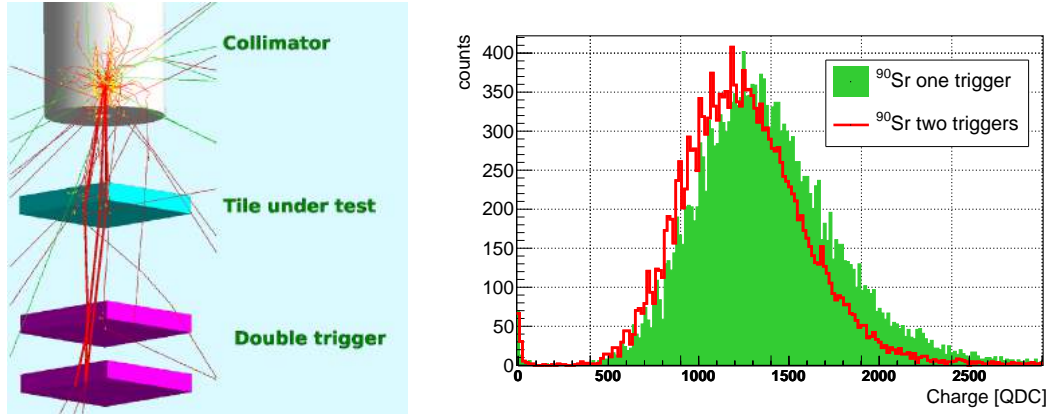


Figure 7.10: *Left*: 100 β^- particles from a ^{90}Sr source. At a distance of 5 cm the trigger selects only particles that pass straight through the TuT and filters photons (green). Only a small portion of the particles (in bright red) triggers a coincidence signal. The coincidence trigger rate is 40 times less than the single trigger rate. *Right*: Data taken with the setup at 30 mV threshold for the triggers. Resulting spectrum with one trigger in green and two triggers in red.

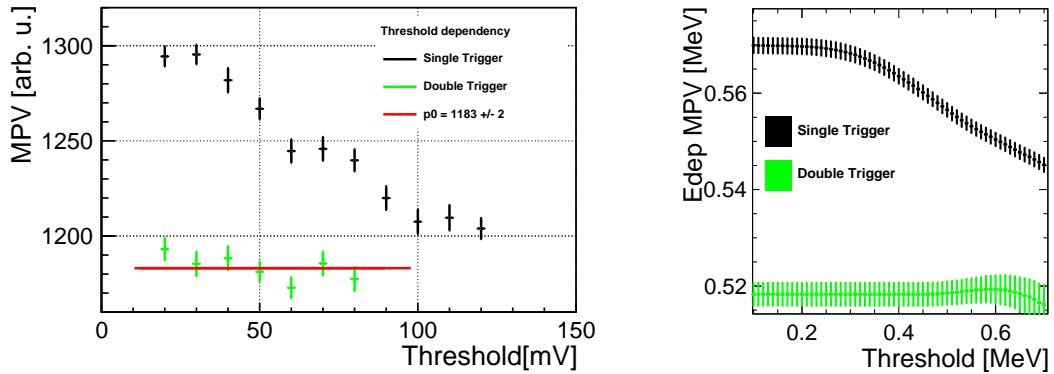


Figure 7.11: *Left*: Trigger threshold dependency of a single trigger tile placed under the TuT. The MPV of the pedestal subtracted data is shown (black). Using a single trigger the MPV is dependent on the set threshold of the first trigger. The coincidence of two triggers (green) is independent of the set threshold. Changing the threshold of the second trigger also has no effect on the MPV.

Right: Simulation of the effect with two triggers under the TuT. Low statistics in the double trigger (green) towards higher thresholds make a MPV extraction less precise.

Simulations done with Geant 4.10.p02

is set to 35 mV and the scaling between the mean double trigger MPV is determined to be: $MPV_{single} \cdot 0.92 \pm 0.03 = MPV_{double}$. Therefore the 35 mV corresponds to a threshold of 0.42 MIP on the single trigger.

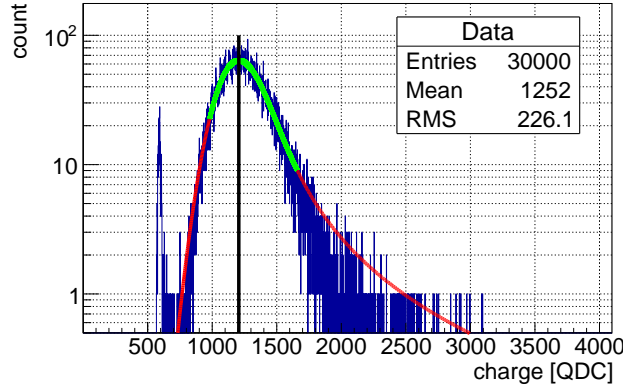


Figure 7.12: Raw data for the fit procedure. The most probable value is roughly estimated with a peak finder. Around this value a Gaussian landau convolution is fitted in the range of -1 RMS to 2 RMS . The resulting fit is shown in green and the MPV value from the fit marked by the black line. The red line shows the fit function extended over the whole range.

Most Probable Value Determination

Figure 7.12 shows the resulting spectrum from the standard measurement. The entries around 0 px are caused by loose contact to the SiPM and misfiring or shifted trigger signals. The most probable value of the spectrum, $MPV(V,T)$ has to be extracted with a reliable fit method. In order to have a reliable fit procedure a landau Gaussian convolution is fitted to the main distribution. As the simulations in figure 7.9 show, the resulting distribution from a ^{90}Sr source is not expected to follow a landau distribution. To counter this only the MPV from a partial fit (-1.0 RMS , $+2.0\text{ RMS}$ from the main peak position) is extracted, see the green line in figure 7.12.

7.1.3 Optical crosstalk measurement

The inter-tile crosstalk XT_{Tile} is defined as the fraction of the total energy that is induced into the four neighboring tiles.

$$XT_{Tile} = \frac{I_2}{I_1 + 4 \cdot I_2}; \quad \begin{array}{l} I_1 = \text{Signal in illuminated tile} \\ I_2 = \text{Signal in neighboring tile} \end{array} \quad (7.8)$$

One tile is illuminated by a UV LED source as can be seen in figure 7.13. The neighboring ones are in the dark. The light leaking from the first tile into the second (dark) tile is quantified. The induced signals by the source have a relatively low amplitude, hence the UV LED is used with high amplitudes to observe a measurable crosstalk. In order to exclude effects of saturation on the SiPM, this measurement is repeated at sixteen different UV light intensities. Due to the extremely low signals induced by inter-tile crosstalk, this measurement is time consuming and highly sensitive to small temperature variations.

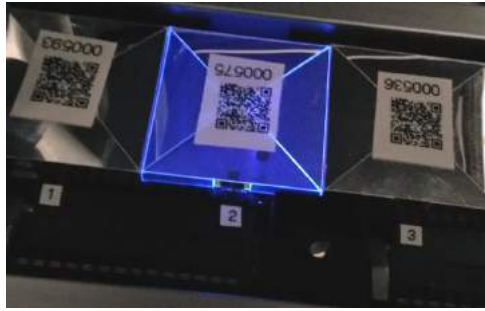


Figure 7.13: Only one LED is set to high intensities to provide light to tiles 2 and 5 to determine XT_{Tile} .

7.2 SiPM for Production

The Ketek PM1125 SMD SiPM was chosen for the production of the tile SiPM system of the University of Hamburg. Table 7.1 shows the technical specifications of this SiPM. The trenched technology promises low correlated noise leading to a low noise over threshold during operation. The SMD SiPM has been soldered on a Capton holder to meet the mechanical requirements of the HBU, see figure 7.14 on the left. The 1200 SiPMs characterized in the

Active Area	$1.2 \times 1.2 \text{ cm}^2$
Cell Pitch	$25 \mu\text{m}$
Fill Factor	48 %
PDE @ 420 nm	$\geq 30 \%$

Table 7.1: Ketek PM1125 technical specifications

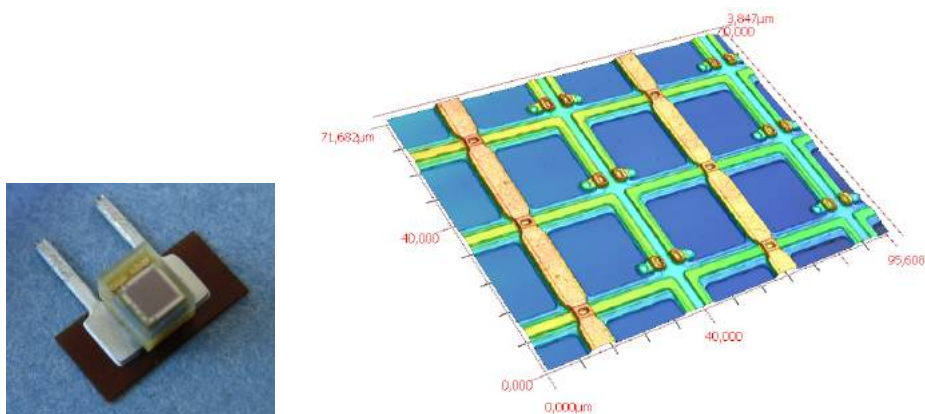


Figure 7.14:

Left: Ketek PM1125 soldered on the Capton holder.

Right: 3D Laser microscope picture of the SiPM with $25 \times 25 \mu\text{m}^2$ pixel (blue) and poly-silicon quenching resistor (orange).¹

setup show a narrow spread in breakdown voltage (table 7.2) and figure 7.15 of only 170 mV. The spread of the gain versus excess bias voltage slope is on the order of the measurement precision. The combination of a small temperature dependency and a moderate gain slope lead to negligible sensitivity to temperature changes during operation.

	Breakdown	Temp. dep.	Gain slope
Value	27.3 V	$17 \frac{mV}{^\circ C}$	$253 \times 10^3 \frac{1}{V}$
RMS	170 mV	30 %	0.8 %

Table 7.2: SiPM figures of Merit and spread at 22 °C. The RMS of the temperature dependency is dominated by errors of measurement uncertainties.

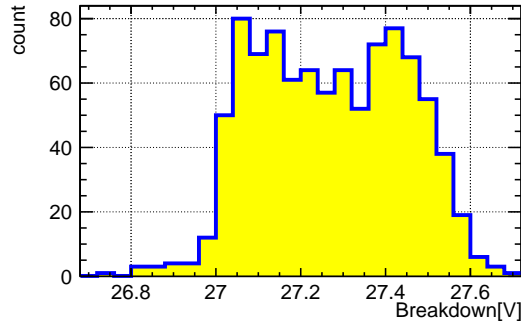


Figure 7.15: Breakdown voltage of 1200 Ketek SiPMs. The difference between two production batches from the manufacturer is visible.

When operating the SiPMs at the same excess bias voltage the spread in gain, DCR and correlated noise are also on the order of the measurement precision. Figure 7.16 shows the dependency of the gain and DCR from the voltage and the corresponding spread for all 1200 SiPM. See figure 7.17 for the correlated noise XT_{corr} for a subsample. With increasing excess bias voltage the spread decreases even further to the order of the precision of the measurement. As an example, the values for an operation voltage of ΔV 2.5 V above breakdown are reported in table 7.3 and the distribution in figure 7.18. The low DCR, in combination with the small XT_{corr} , will enable a nearly noise-free operation for thresholds of 5 fired pixels.

7.3 Characterization of Scintillating Materials

Three batches of different scintillating tiles with the KETEK PM1125 were produced, see table 7.4. Eljen EJ-200 has similar properties to the formerly used Bicron (BC-408). It

¹Picture made by Michael Nitschke

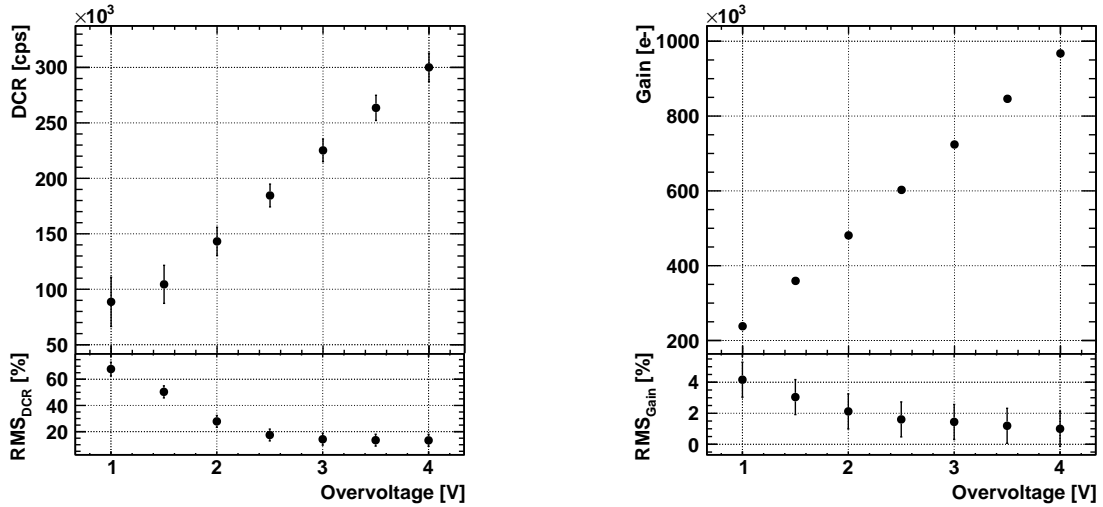


Figure 7.16: SiPM performance for all 1200 pieces

Left: Average DCR versus excess bias voltage. The DCR measurement itself has an error of up to around 30 % for low voltages. The spread of the distribution for all SiPM is depicted in the lower part as the RMS and its error.

Right: Average gain versus excess bias. With higher excess voltage the spread of the distribution equals the measurements precision of 1% and all SiPM are indistinguishable.

@ 2.5 V OV	Gain	DCR	XT_{corr}
Value	613×10^3	2×10^5 cps	0.03
RMS	1.4 %	16 %	43 %

Table 7.3: SiPM figures of Merit and spread at 2.5 V excess bias voltage and 22 °C

1	Bicron (BC-408) scintillator	300 pc (142 pc measured)
2	Eljen EJ-200 scintillator	276 pc (214 pc measured)
3	Eljen EJ-200 dried SiPM	576 pc

Table 7.4: SiPM / Tile batches produced

is an organic polyvinyltoluene plastic scintillator with a light emission in the low UV/blue light spectrum peaking at 430 nm matching the peak sensitivity of the PM1125 SiPM in table 7.1. As wrapping for the scintillating tile, 3M ESR foil (3M Vikuiti™ Enhanced Specular Reflector (ESR), 65 μm thick, 98 % reflectivity) was chosen, see chapter 7.4 for more details. The $3 \times 3 \times 0.3 \text{ cm}^3$ tile is machined from a large plate with a size of $500 \times 500 \text{ mm}^2$ and $30 \pm 0.2 \text{ mm}$ thickness. The plate is cut with a hard metal (Widia) diamond blade at low RPM into strips of $320 \times 500 \text{ mm}^2$. The strips are placed on a vacuum holding table and milled

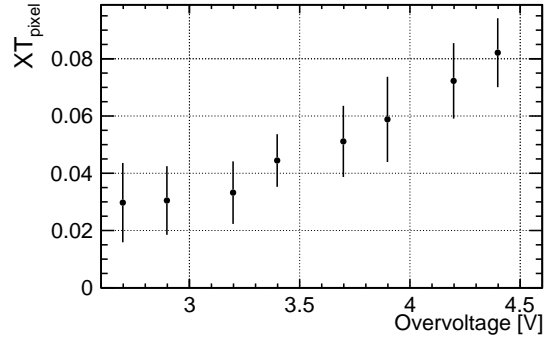


Figure 7.17: Average correlated noise XT_{corr} for all 1200 SiPMs. The spread of the distribution is below the measurement uncertainty and not shown.

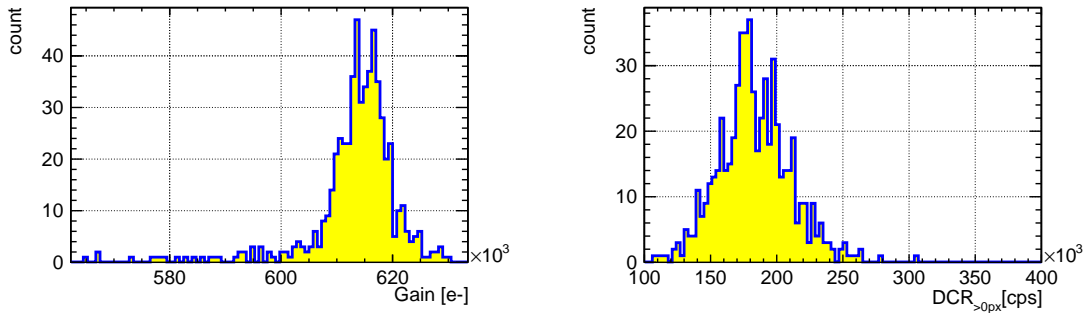


Figure 7.18: SiPM gain and DCR spectra @ 2.5 V excess bias voltage.

down with a 60 mm two head diamond reamer (2000 RPM) with a industrial diamond head for pre-milling and a natural diamond head for polishing to a thickness of $30 \text{ mm}^{+0.001 \text{ mm}}_{-0.2 \text{ mm}}$ in order to fit the detector tolerances. The strips are cut to $320 \times 320 \text{ mm}^2$ using the hard metal blade. A FP4 router with a fast-running Widia milling head and the polishing head of the diamond reamer as second step are used to perform the final cut to dimension of $29.8 \times 29.8 \text{ mm}^2$ with a precision at the $50 \mu\text{m}$ level. A pack of 10 raw cut tiles are pressed together in a custom made rotateable holder. The two opposing sides are milled down and polished to 29.8 mm. The high precision turn of the holder by 90° guarantees perpendicular angles of the tiles. In all steps of the procedure, high pressured air has to be applied to cool the scintillator material and remove chips from the tools. A cut out in front of the SiPM where the light collection is largest ensures a homogeneous response to MIP. The optimization of the cut out dimensions is based on a study performed by C. Soldner et.al [72], but simplified for faster machining. The step structure to hold the SiPM-Capton unit displayed in figure 7.19 on the left is milled via a CNC-router with a hard metal (Widia) end-mill. For the cut out in front of the SiPM, a 2 mm ball-nose end-mill is used. The cut is left unpolished. High pressured air has to be applied in this step as well to prevent the melting of the scintillator. The SiPM

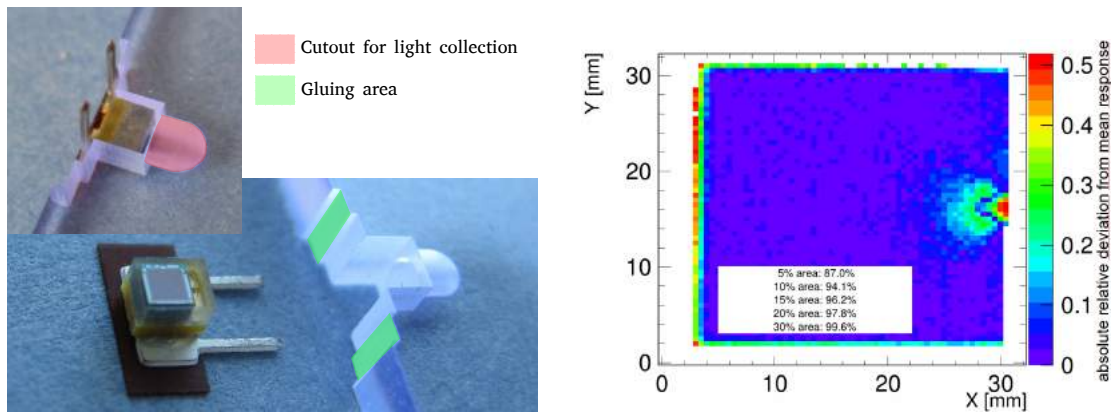


Figure 7.19:

Left: Optimized tile cutout. Epoxy glue is applied in the green area with a dispenser to fix the SiPM Capton holder to the tile and prevent glue from degrading the SiPM light collection. The red cutout with a single drill reduces the scintillating light produces close to the SiPM and acts a collecting lens to homogenize the overall response.

Right: Scan with ^{90}Sr source over the tile area. The deviation from the mean response is shown. The strong deviations on the tile sides are due to the limited focusing of the source and can be ignored. Scan done by MPI Munich (group of Frank Simon)

is glued to the tile using its Capton holder and the coupling in the cut out is through air. The 3M ESR foil is cut with a CO_2 laser cutter to 100 μm precision. Two cutouts for LED

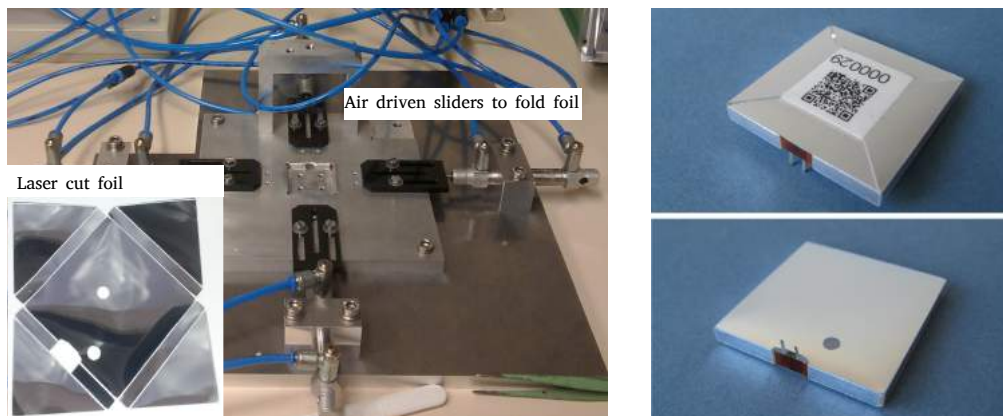


Figure 7.20:

Left: Laser cut foil with precut folding grooves and half automated wrapping machine. The foil is placed in the middle of the folding machine and the tile inserted on top. The four air driven sliders fold the foil over the edges and top of the tile. A QR code sticker is placed to close the tile.

Right: Wrapped preproduction tile with one LED calibration hole after gluing the SiPM and Capton holder.

calibration, one for the HBU LED and one opening for the Calibration setups are added as well as the SiPM cutout. A lower power setting on the cutting laser enables to pre-fold the foil for fast and precise wrapping. The foil and tile are placed in a half automated wrapping machine in figure 7.20. The four sliders simultaneously fold the foil over the tile which is closed with a QR code sticker for easy and automatic identification of the tile. Figure 7.22

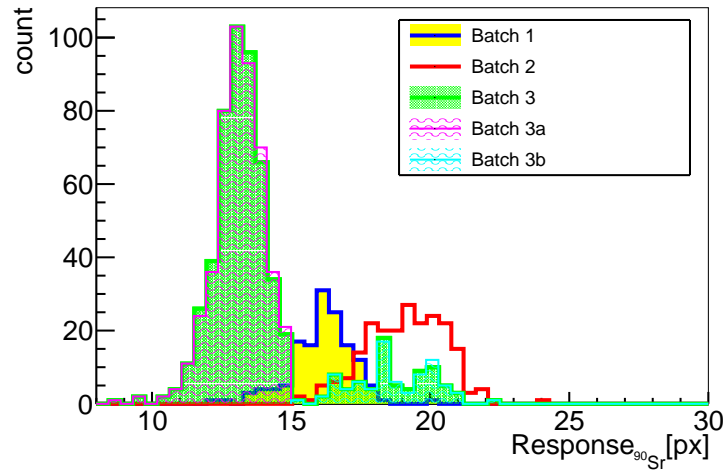


Figure 7.21: Response for all three batches at 2.5 V excess voltage. Batch 2 is expected to have a higher response than batch 1 due to the use of EJ-220 scintillator with higher photon yield in comparison to Bicron. For batch 3, the majority of SiPMs have been heated. The epoxy changed opacity and decreases the response and broadens the spread of response. Batch 3 is split into 3a and 3b to separate the untreated SiPMs

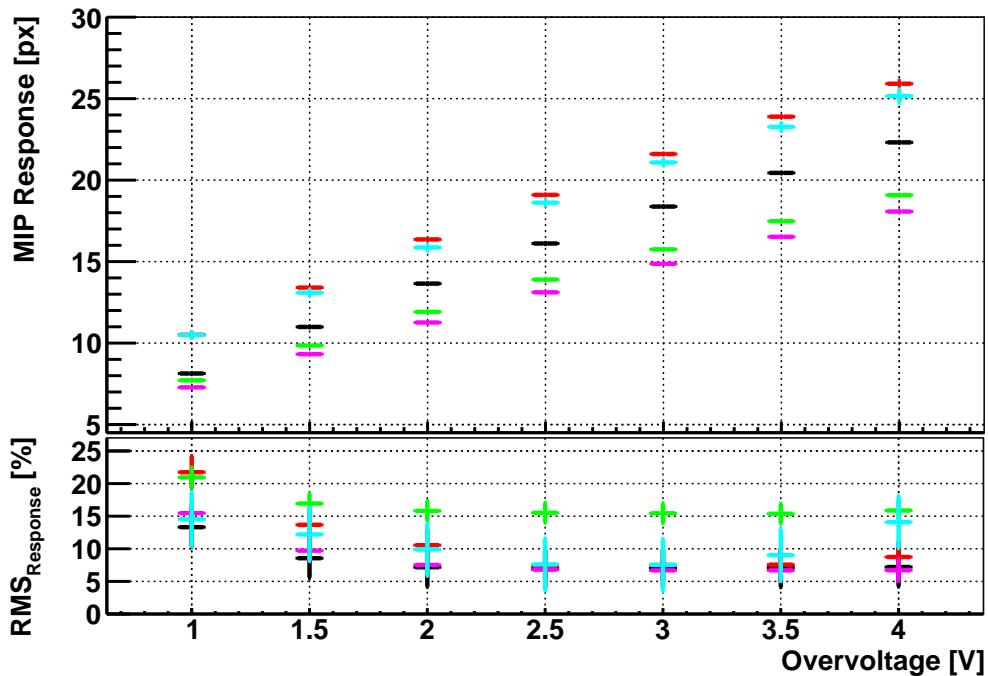


Figure 7.22: Mean response and corresponding spread for all three batches produced at the University of Hamburg. The worsened spread and response of batch 3 can clearly be seen. Batch 3 has been split according to the above separation at 2.5 V over-voltage into batch 3 and batch 3a.

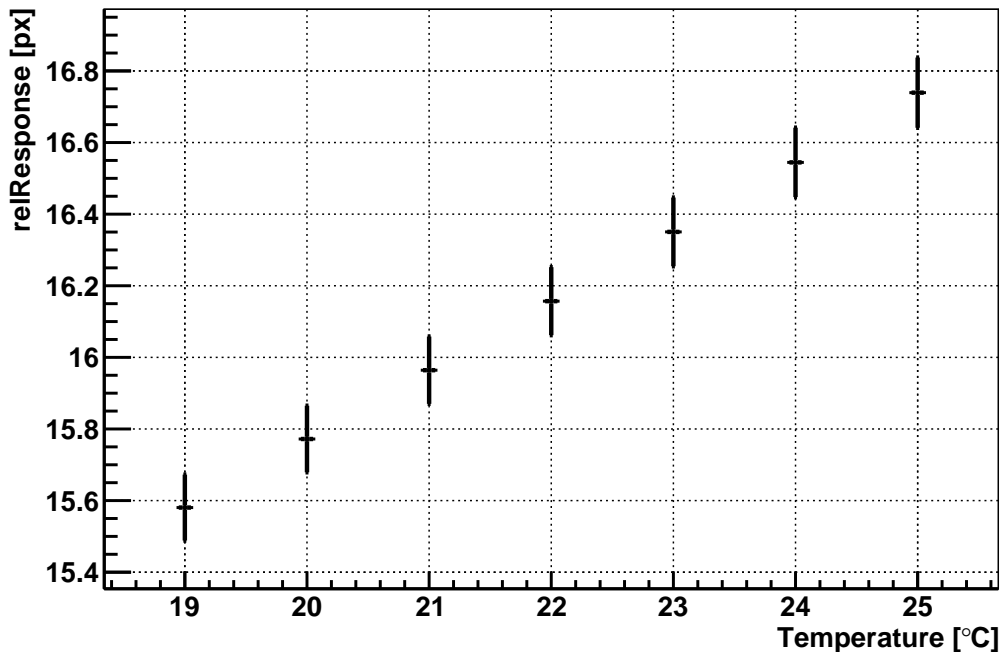


Figure 7.23: Mean response $relResponse$ for a scenario when the temperature of a detector changes after calibration at 22 °C, using batch 1

shows the responses and spread of the distribution for different over-voltages for all three batches. During the assembly of batch 1 and 2, soldering problems were experienced due to the so called popcorn effect [73]. The transparent epoxy enclosing the SiPM absorbs humidity from the air. When soldered, the vaporising water can rip the bonding off. Drying the SiPM at high temperatures diffuses the water out of the epoxy for a safer soldering. Most SiPMs for batch 3 had to be dried in 80 °C for four days before mounting on the tile. This procedure changes the SiPM casing opacity and thus the response is reduced and larger spreads are introduced. To separate this effect within the batch a cut at a response of 15 px has been introduced, splitting the batch into batch 3a and batch 3b. Figure 7.21 shows as an example the spreads at 2.5 V over-voltage and figure 7.22 the response and its spread dependency on the over-voltage.

7.3.1 Temperature dependency of the detector after calibration

With the complete characterization of SiPMs and tiles the behavior of a detector with changing temperatures can be investigated. To simulate the temperature dependency of all tiles, the effective over-voltage (and thus the operational voltage at 22 °C) has been changed according to table 7.3. Assume the following scenario with batch 2. The operational voltage of each SiPM is set to 2.5 V at 22 °C over-voltage ($2.5 V_{ov\ 22^\circ C}$). The detector has been

Surfaces	Sides	rel. Response	Error
3M ESR	3M ESR	1.0	1%
3M ESR	Air	0.40	3%
Air	3M ESR	0.62	1%
Air	Air	0.24	10%

Table 7.5: Impact of reflective foil wrapping on the light collection.

The surface and sides were covered with 3M ESR foil or left to the air to demonstrate the impact of the reflecting foil on the different surfaces and edges of the tile. Values are normalized to the completely covered tile.

calibrated at 22 °C. Figure 7.23 shows the change in response

$$relResponse(2.5 V_{ov, 22^\circ C}, T) = \frac{MPV(2.5 V_{ov, 22^\circ C}, T)}{G(2.5 V_{ov, 22^\circ C}, 22^\circ C)} \quad (7.9)$$

when the gain value $G(2.5 V_{ov, 22^\circ C})$ is used as reference without adaptation or recalibration at the different temperatures.

7.4 Wrapping and Surface Treatment of Scintillating Tiles

As an alternative to the 3M ESR foil, different wrapping and coatings applied to the surface were investigated.

7.4.1 Photon containment in scintillating Tiles

The baseline geometry of the tiles is a narrow plate out of polished plastic with a refractive index of 1.58. Most of the light produced anywhere in the tile undergoes total internal reflection on the surfaces of the tile due to the shallow incident angle. Total internal reflection on air gives a maximum angle of 39° inside of the tile. Most light produced will hit the surface with a smaller angle. On the sides, most of the light escapes the tile due to the steeper impact angles. Table 7.5 shows a comparison of the response for tiles partly wrapped with 3M foil. Since the loosely wrapped foil rarely touches the flat polished surface, most of the light undergoes total internal reflection and removing the foil from the surfaces reduces the response to 62%. Removing the foil on the sides reduces the response to 40% due to the higher incident angles of the light. Covering the tile surfaces with paint or similar materials (see figure) will only result in degradation of the reflection as can be seen also in table 7.5. This is consistent with previous studies [74] and [75]. Figure 7.24 shows two different mounting strategies. Mounting all tiles as a sandwich between two common 36 × 36 cm² foils is considered as a simplification for the assembly and wrapping procedure. An additional step for the edge treatment with paint, chemical treatment or side wrapping will be necessary. The tiles cannot be calibrated then before mounting with high precision as any movement or opening of the cassette will deteriorate previous calibrations. As described in chapter 5, containment of the

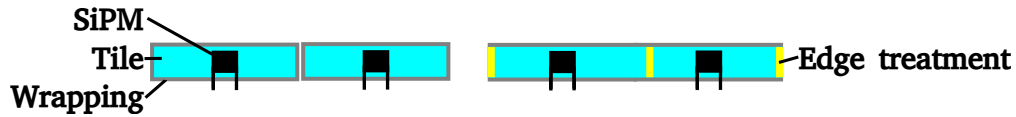


Figure 7.24: Sandwich (right) and single wrapping (left) mounting. In the Sandwich build the tiles have a common surface reflector foil and an edge treatment for reflexion and optical isolation. One side is mounted on the HBU, the other on the inner side of the cassette. Single wrapped tiles are optically and mechanically isolated.

	Material	Reflection	Application method	Response	Error
I	3M ESR	direct	wrapping	1.0	1%
II	Aluminum	direct	evaporation	0.17	20%
III	Paper (Mondi Maestro [®] 80 $\frac{g}{cm^2}$)	diffuse	wrapping	0.68	2%
IV	TiO ²	diffuse	80 μ m paint	0.30	3%

Table 7.6: Comparison of different surface treatments.

All responses are normalized to the completely wrapped tile with 3M ESR foil.

The value for the tile treated with evaporated Aluminum shows a very small signal of under five pixels fired.

energy contributions is important for a good particle flow performance. The crosstalk for the sandwich with 3 %-5 % is considerably higher then for the single wrapped tiles with <0.1 %, see chapter 7.1.3.

7.4.2 Comparison of wrapping / coating alternatives



Figure 7.25: Four different coatings for the tile design. From left to right:

I: 3M ESR foil wrapping with QR code for easy identification.

II: Evaporated aluminum.

III: Paper (Mondi Maestro[®] 80 $\frac{g}{cm^2}$) wrapping.

IV: TiO² paint with 80 μ m thickness

Three different wrappings or surface treatments were tested as alternative to the 3M ESR wrapping. Figure 7.25 and table 7.6 show the different wrappings and methods applied. Any surface treatment that prevents total internal reflection by diffusing the surface like TiO² paint (IV) or evaporated Aluminum (II) worsens the response of the tile. Paper (III) is a usable alternative to costly 3M ESR reflective foil degrading the response only mildly to 68% of the 3M ESR foil.

Chapter 8

SiPM voltage adjustment with the Spiroc2b

The Spiroc2b features a channel wise adjustable voltage. Separate voltages can be set for each SiPM using the internal voltage adjustment of the Spiroc2b. A shift in Voltage effective shifts the operational voltage over breakdown and changes important SiPM properties like gain and the photon detection efficiency. Consequently an offset in the calibration and an error of unknown magnitude can be introduced to the calibration deteriorating the energy resolution of the whole detector. In order to evaluate the error and feasibility of different operational strategies for the detector, the precision with which the bias voltage of the SiPMs can be set must be known to the mV level. The voltage stability after a power cycle and foreseen environmental changes for the detector operation must also be considered. The bias voltage of the SiPMs (HV_{SiPM}) are set by two components.

$$HV_{SiPM} = HV_{PWB} - (V_{min} \dots V_{max}); \quad \begin{array}{l} HV_{SiPM} = \text{SiPM voltage} \\ HV_{PWB} = \text{Power board voltage} \\ V_{min} \dots V_{max} = \text{Internal voltage adjustment} \end{array} \quad (8.1)$$

HV_{PWB} is a common voltage distributed by the power board for all Spiroc2bs. The voltage for each SiPM is adjusted channel-wise via the Spiroc2b's adjustable internal voltage setting in the range of V_{min} to V_{max} (in 8 bit resolution). V_{min} to V_{max} is subtracted from the power board voltage. The exact voltage set by a specific register setting is unique to all channels and chips. V_{PWB}^{max} is the maximal substractable voltage from HV_{PWB} , uniquely for each power board in revision three. A voltage drop occurs between the power board and the Spiroc2bs over the flex-lead connectors (V_{Drop}).

$$V_{max} = V_{PWB}^{max} - V_{drop} \quad (8.2)$$

The precision with which the voltages can be set is investigated separately for the power board (section 8.1) and the Spiroc2b (section 8.2). Figure 8.1 shows the setup used for the measurements. Two high-precision voltmeters are used simultaneously to decouple the contributions of the power board and the Spiroc2b. For all measurements presented in this thesis, the power board with the serial number 10108 00 2 was used.

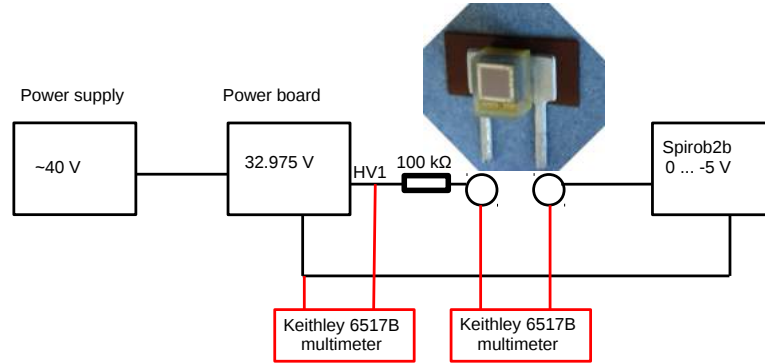


Figure 8.1: SiPM connection on the Spiroc2b and measurement setup.

One pin of the SiPM is connected to the global bias voltage HV_{PWB} provided by the power board. The other pin of the SiPM is connected to the Spiroc2b, which subtracts the internal voltage $V_{min} \dots V_{max}$ that can be adjusted via an 8 bit register. The maximum voltage in that range is determined by the voltage delivered by the power board V_{PWB}^{max} . Every channel shows a different behavior and dynamic range. In order to separate effects from the power board, the high voltage delivered from the power board and the high voltage on the Spiroc2b are measured separately with two Keithley 6517b multimeters (precision of less than 1 mV).

8.1 Functionality and Precision of the Power Board



Figure 8.2: Power Board (rev.3)

The power board can quickly be switched or replaced on the side interface board of a cassette. It provides all bias voltages needed for the Spiroc2b digital and analogue operation. Drop down voltage regulators set with high precision resistors provide the three high voltage lines for SiPM bias $HV_{PWB1..3}$ and the analogue voltage for the individual channel adjustment V_{PWB}^{max} . Because of the limited resistor precision ($\approx 0.05\%$), the voltages are unique to each power board.

The power board in Figure 8.2 generates several global voltages for chip operation. An external power module supplies three voltages, 12 V, 5 V, 3.3 V, and a common HV_{ext} voltage for the operation of all HBU based AHCAL systems. Out of equation 8.1 and equation 8.2, HV_{PWB} and V_{PWB}^{max} are generated by the power board. Three high voltage lines with separate voltages are available $HV_{PWB(1..3)}$. They can be routed to individual Spiroc2bs on the HBUs. The voltages are regulated by drop down voltage regulators. The voltage is defined via analogue voltage dividers set by high precision resistors. The resulting voltage deviates several 100 mV from the theoretical voltage since the analog resistors have an 0.05 % error. After setting the resistors the actual voltage on the high voltage lines have to be measured with a precision voltmeter.

The external supply high voltage for the power board, HV_{ext} must be at least 3 V over

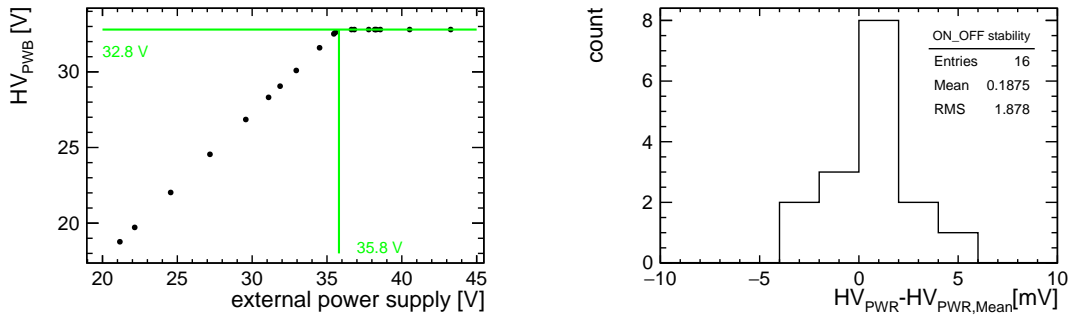


Figure 8.3:

Left: Turn on behavior. HV_{PWB} is produced via drop-down voltage regulators. HV_{ext} must be at least 3 V over the target voltage HV_{PWB} to reach a stable HV_{PWB} .

Right: Power cycling the power board results in a reset error of 1 mV. The deviation from the mean voltage is shown for 16 power cycles.

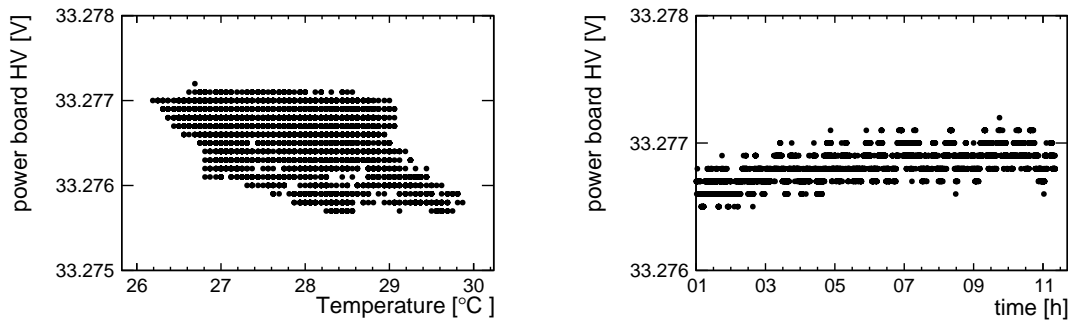


Figure 8.4:

Left: Stability of HV_{PWB} with temperature variation over 4°C.

Right: Stability of HV_{PWB} over time over 11 hours at the same temperature, measured with a DALLAS DB20 temperature sensor on the drop down regulator.

the target voltage HV_{PWB} to achieve a stable target voltage. Figure 8.3 on the left shows

PWB ID	V_{PWB}^{max}	error
10108 00 9	4.704 V	1 mV
10108 00 11	4.716 V	1 mV
10108 00 6	4.466 V	1 mV
10108 00 1	4.718 V	1 mV
10108 00 10	4.496 V	1 mV
10108 00 2	4.753 V	1 mV
10108 00 8	4.709 V	1 mV
10108 00 3	4.765 V	1 mV
10108 00 7	4.708 V	1 mV

Table 8.1: V_{PWB}^{max} for 16 power boards. V_{PWB}^{max} needs to be measured separately for each power board to determine HV_{SiPM}

HV_{PWB} while HV_{ext} is slowly ramped up. If HV_{ext} is much higher than HV_{PWB} the drop down voltage regulator give off excessive heat. In Figure 8.4 on the right the voltage stability when power cycling the power board is shown. HV_{PWB} is reproduced with 1 mV precision and a min - max spread of under 10 mV. The excellent long term stability in temperature and time leads to an error of less than 2 mV on HV_{PWB} (see Figure 8.4). The expected enviromental temperature range has been tested.

The bias voltage for the internal voltage adjustment V_{max} of the Spiroc2b is unique for each power board. Table 8.1 shows V_{PWB}^{max} for 9 different power boards with a difference of several 100 mV. V_{drop} has been measured for 24 channels on different parts of the HBU operated with minimal bias voltage (minimizing the errors, see next Chapter), $V_{Drop} = HV_{PWB} - HV_{SiPM} - V_{PWB}^{max}$ and found to be $39 \text{ mV} \pm 3 \text{ mV}$ (spread of measured values). In order to efficiently use the power board V_{PWB}^{max} needs to be measured individually for each power. The remaining uncertainty in the power board voltage due to environmental changes and reset is on average 1 mV precision and a min - max spread of under 10 mV.

8.2 Spiroc2b internal voltage adjustment

In order to take measurements with mounted SiPMs in light HV_{SiPM} can be limited to about 14 V which is well under the breakdown voltage of the SiPMs. As depicted in Figure 8.1, two voltage meters are used to decouple the influences of the power board. The result is the subtracted voltage depending on the register setting for each channel, see equation 8.3. Because of the high chance of damaging the Spiroc2b or a single channel during the measurement, all data presented in this Chapter was measured on only two chips and presumably represents the behavior of the whole detector. During calibration the Spiroc2b crashes frequently, delivering an unstable voltage and has to be reset. An extensive study of the internal voltage adjustment of the Spiroc2b was conducted on one ASIC without SiPMs mounted and full bias applied. To summarize the applied SiPM voltage as a function of the register setting 0..255

is

$$\begin{aligned} F(0\dots255) &= V_{min}\dots V_{max} \\ &= HV_{SiPM}(0\dots255) - HV_{PWB} + V_{Drop}. \end{aligned} \quad (8.3)$$

8.2.1 Unstable channel

About 2% of the investigated channels show an unstable behavior when ramping up the power board voltage as seen in Figure 8.5. The channel on the left behaves as expected by keeping his programmed voltage drop but the channel on the right drops to the maximum voltage independently of the register setting as soon as the high voltage is fully ramped up. This behavior can only be seen if the full HV is applied. It cannot be spotted during low voltage calibration.

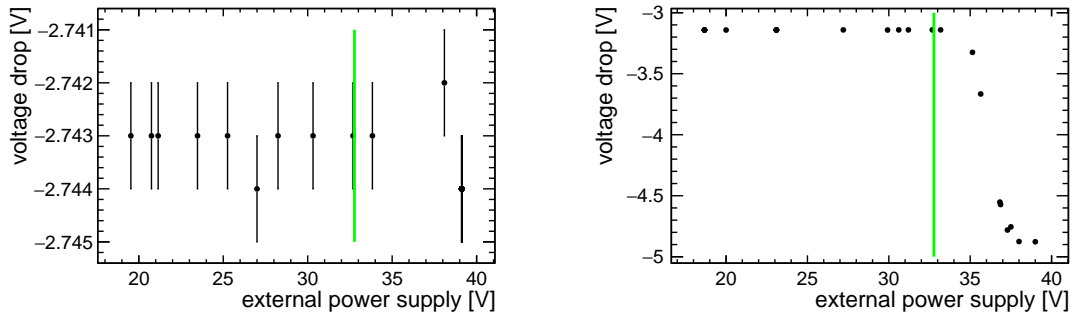


Figure 8.5: Channels during ramping the power board.

Behavior of $HV_{SiPM} - HV_{PWB}$ a broken (*left*) and a working channel (*right*) while ramping up the external supply voltage. In green the external voltage when the power board delivers a stable HV_{PWB} , see Figure 8.3

8.2.2 Voltage stability

To test the stability of the internal voltage adjustment, six points in the full register range were measured on each channel. They were measured three times with power cycling the detector in between (Figure 8.6). With higher register value, the stability of resetting the voltage decreases, leading to up to 20 mV shifts (maximum deviation) at register values over 200.

8.2.3 Single channel calibration

Three different calibration strategies and the resulting uncertainties in the set voltage are investigated: First, the most extensive calibration with a separate calibration curve for each single channel j and chip i with 6 points to determine $f_{i,j}(0\dots255)$, equation 8.4 I. The second strategy is to obtain a complete calibration of all channels of one chip. This curve is used for all other chips with one function for each channel $f_j(0\dots255)$, equation 8.4 II. Third, the

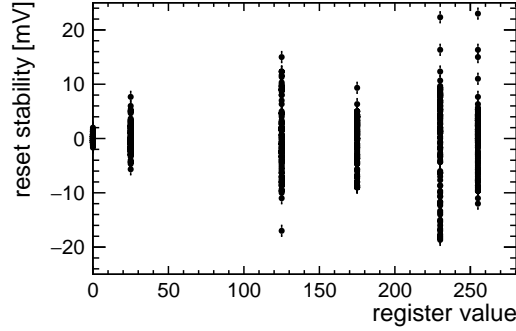


Figure 8.6: Reset stability of the internal voltage adjustment. Six register values (0, 25, 125, 175, 230, 255) where repeatably measured for all 36 channels of one Spiroc2b. The plot shows the deviation from the mean value of each channel.

detailed calibration of one chip extracts a general calibration curve common for all channels and chips, equation 8.4 **III**. For each strategy, the contribution of the internal voltage setting of the Spiroc2b on the resulting errors in setting the voltage are investigated as the absolute difference between the desired voltage and the set one as $\sqrt{(V(0...255) - F(0...255))^2}$.

$$\begin{aligned}
 F(0...255) &\sim V_{min...V_{max}} \\
 &\sim f_{i,j}(0...255) \quad \text{I} \\
 &\sim f_j(0...255) \quad \text{II} \\
 &\sim f(0...255) \quad \text{III}
 \end{aligned}
 \tag{8.4}$$

Different calibration functions

$f_{i,j}(0...255)$ = Curve for each channel j and chip i

$f_j(0...255)$ = Curve for each channel j

$f(0...255)$ = Averaged curve for all channels and chips

I Single channel calibration with $f_{i,j}(0...255)$

A calibration curve for each of the 36 channels of one chip has been obtained measuring the resulting voltage from six (0, 25, 125, 175, 230, 255) register values. The averaged non linearity of all 36 channels is shown in Figure 8.7 leading to deviations under 5 mV. The deviation from linearity shows the same behaviour for all 36 channels and does not average out. Showing no significant non-linearity, the channel calibration curve can be assumed to be linear. Comparing a direct measurement of the voltages including the reset errors from section 8.2.2, the precision with which the voltage can be set on the Spiroc2b is dominated by the reset error, see Figure 8.8. Spiroc2b crashes or single channel upsets made is necessary to measure many channels frequently. This time consuming calibration and the chance to break channels during measurement is not feasible for the internal voltage calibration of a detector with several millions of channels.

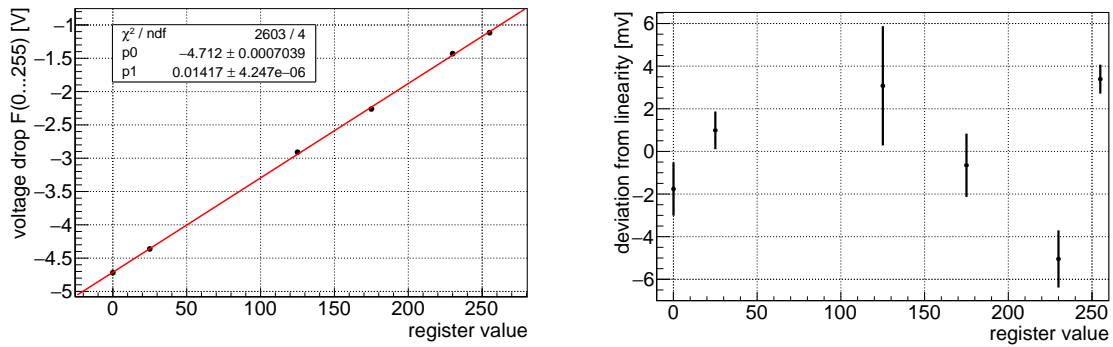


Figure 8.7:

Left: A calibration curve $f_{i,j}(0...255)$ for a single channel.

Right: Deviation from linearity, averaged for all 36 channels of one chip.

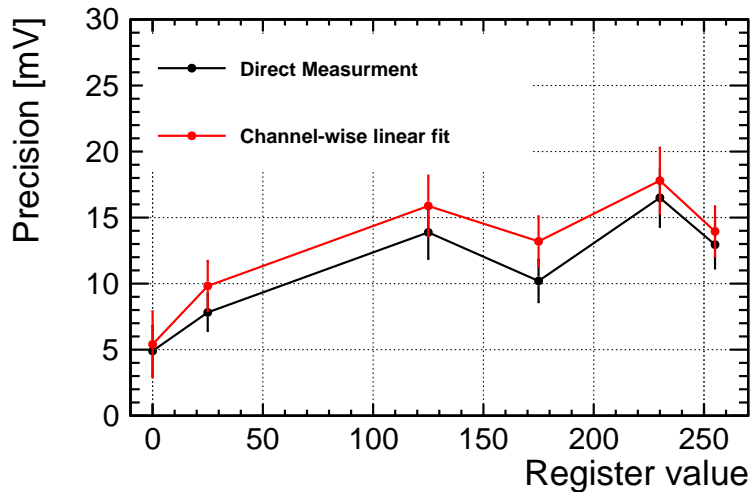


Figure 8.8: Voltage setting precision with single channel calibration. The RMS of the distribution of $\sqrt{(V(0...255) - f_{i,j}(0...255))^2}$ for each channel is shown for channel wise linear calibration in red and actual measured voltage in black. The reset errors are included in this plot as the mean deviation extracted from Figure 8.6. The nonlinearity has a minor influence in worsening the precision and the reset error dominates.

II Channel-wise calibration with $f_j(0...255)$

The detailed calibration $f_j(0...255)$ for each channel from the first Spiroc2b (method **I**) is transported to another Spiroc2b. It is used as calibration curve for the second Spiroc2b used in this analysis. Figure 8.9 in red shows the impact on the setting precision, dominating all other influences by one order of magnitude. Only one chip would need to be calibrated to great extent and the result used for all chips. This calibration strategies would be feasible for an AHCAL detector.

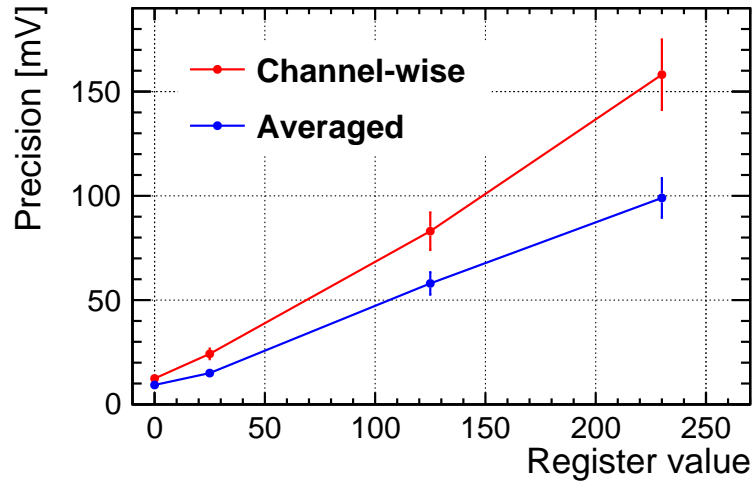


Figure 8.9: Precision of set voltage depending on the register value. The calibration obtained from the first chip was applied to the second one. **I** with $f_j(0\dots255)$ in red and the averaged calibration **II** with $f(0\dots255)$ in blue.

III Averaged calibration with $f(0\dots255)$

The 36 calibration curves from **II** are averaged to obtain one single calibration curve for all channels and Spiroc2bs $f(0\dots255)$. Figure 8.9 in blue shows the impact on the set voltage precision. An averaged calibration shows better precision than the channel wise calibration. The obtained calibration curve could be used for all Spiroc2bs and channels as the best compromise between precision and feasibility.

8.3 Detector calibration and precision

The only realistic calibration method is **III** from equation 8.4 with one common calibration curve ($f(0\dots255)$) for all channels and Spiroc2b ASICs. As a summary, the calibration function 8.5 is obtained. The resulting precision with all possible errors is presented in equation 8.6. One single averaged calibration curve is used for all channels and Spiroc2bs. The register setting 0 provides all SiPMs with the same voltage with a precision of 15.7 mV. A wider voltage range to be able to adjust for outliers, or apply specific voltages for each SiPM will lead, depending on the used range, in a precision degradation to 37 mV when using the full register range. The internal voltage adjustment of the Spiroc2b can be used to correct for outliers, but using the register value 0 as a common voltage for all SiPMs on a Spiroc2b is the most feasible option if the spread of parameters of the SiPMs permit.

$$HV_{SiPM} = HV_{PWB} - (V_{PWB}^{max} - 0.039 V) + 0.015 V \cdot RegV \quad RegV = DAC[0..255] \quad (8.5)$$

$$\begin{aligned} \delta HV_{SiPM} = HV_{Precision}^2 &= (1 \text{ mV})^2 && \text{PWB reset precision} \\ &+ (2 \text{ mV})^2 && \text{PWB stability} \\ &+ (1 \text{ mV})^2 && \text{PWB } V_{PWB}^{max} \text{ stability} \\ &+ (3 \text{ mV})^2 && \text{HBU } V_{drop} \text{ stability} \\ &+ (3 \text{ mV})^2 && \text{Spiroc2b non linearity} \\ &+ (1.2 \text{ mV} + 0.02 \cdot RegV \text{ mV})^2 && \text{Spiroc2b reset stability} \\ &+ (15 \text{ mV} + 0.4 \cdot RegV \text{ mV})^2 && \text{Spiroc2b voltage precision} \end{aligned} \quad (8.6)$$

Chapter 9

Commissioning and Calibration Validation at the DESY II Test Beam

This chapter discusses part of the results of the test beam with the above discussed HBUs and Tiles. The goal was to ensure the overall functionality and reliability of the detector. Also the calibration of chapter 7 and 8 can be validated in a test-beam environment. The main focus of this chapter is the validation of the calibration and the uncertainty encountered in test beam environments. During the test beam campaign in January 2014, eight single HBUs were tested in the DESY II e^- beam. They were arranged in a stack with one HBU per layer without absorbers. The main goal was a complete system test with several layers. Also, all channels were calibrated with the 3 GeV e^- test beam. Different absorbers were placed in front of the stack to generate EM showers. The detector ran asynchronous to the test beam and despite the high rate of the DESY II beam, noise was inflicting the data efficiency. To minimize noise, the coincidence of two plastic scintillators read out via PMTs and placed in front of the detector were used as external validate event signal to the Spiroc2b, see section 6.3.2. Figure 9.1 shows the setup used in the test beam. The four HBUs with tiles from the University of Hamburg were positioned as the two front and the two last layers. One goal was to determine the precision of the lab calibration at the University of Hamburg on a small subset of tiles. Small electromagnetic showers produced in the cassettes in front of a layer shift the MPV to higher values, see figure 9.2 where the deviation from a MIP like spectrum can clearly be seen in the last layer compared to the front layer. To exclude them, only the first two layers were considered. To minimize the contributions from using the internal voltage adjustment of the Spiroc2b, the bias voltage on every single SiPM was remeasured in operating conditions with a high precision voltmeter. Out of equation 8.5, only



Figure 9.1: System test at DESY II test beam.

Eight HBUs were tested in a stack without absorber. The first two and last layers are technology from the University of Hamburg. The setup was mounted on a moving stage to scan each position of the tiles with the 3 GeV electron beam.

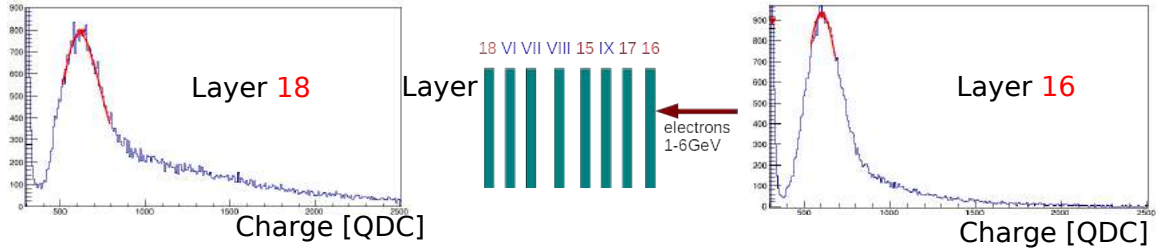


Figure 9.2: Production of small showers throughout the detector setup. As a comparison the RAW data from two channels in the first layer of the setup (layer 16) and the last layer of the setup (layer 18) are shown. The two channels are in the same position inside the layer.

the reset effects and stability contribute to the error of the measured voltage.

$$\begin{aligned}
 HV_{Precision}^2 &= (1 \text{ mV})^2 && \text{PWB reset precision} \\
 &+ (2 \text{ mV})^2 && \text{PWB stability} \\
 &+ (1 \text{ mV})^2 && \text{PWB } V_{PWB}^{max} \text{ stability} \\
 &+ (3 \text{ mV})^2 && \text{HBU } V_{drop} \text{ stability} \\
 &+ (3 \text{ mV})^2 && \text{Spiroc2b non linearity} \\
 &+ (1.2 \text{ mV} + 0.02 \cdot RegV \text{ mV})^2 && \text{Spiroc2b reset stability} \\
 &+ (15 \text{ mV})^2 && \text{Spiroc2b voltage precision}
 \end{aligned} \tag{9.1}$$

The voltage uncertainty is therefore 16.9 mV, since the whole register range of DAC=255 was used to adjust the voltages. A total of 54 channels were remeasured and compared to the laboratory calibration. To compare the lab calibration to the test beam 3 GeV electrons were simulated and deposited an energy with an MPV of 472 keV. During the test beam, no temperature readout from the detector was available. An external PT1000 temperature sensor

attached to the middle of one cassette gave a rough estimation of the detector temperature over time. Variations between 18°C and 30°C , with a mean of around 26°C , were measured during the calibration. This wide temperature range (day, night, weather) had to be taken into account as an error on the calibration correction for the temperature since the laboratory temperature was 22°C . According to table 7.3 the operational voltage on the calibration set was shifted by $+68\text{ mV}$. The complete transformation, including the factor from 3 GeV electrons to the double trigger ($0.88_{(3\text{ GeV}\rightarrow\text{doubletrigger})}$) from section 7.1.2 and the difference between the double and single trigger calibration ($0.92_{(\text{double0}\rightarrow\text{singletrigger})}$) for comparing the lab calibration and the test beam calibration, is given by

$$MPV_{UHH} = MPV_{LAB} \cdot 0.92_{(\text{double}\rightarrow\text{singletrigger})} \cdot 0.88_{(3\text{ GeV}\rightarrow\text{doubletrigger})}. \quad (9.2)$$

To compare the test beam data $MPV_{TestBeam}$ with the MPV_{UHH} calibration, the temperature corrections and uncertainties have been expressed as a shift in the individual operational voltages measured for each tile.

$$\Delta V(T) = \frac{17\text{ mV}}{^{\circ}\text{C}} \cdot 4^{\circ}\text{C} \pm \frac{17\text{ mV}}{^{\circ}\text{C}} \cdot 12^{\circ}\text{C}. \quad (9.3)$$

The gain has been extracted with dedicated LED runs during the test beam. The pedestal has been determined as the peak position of non triggered events directly from the beam data. Figure 9.3 on the left shows the correlation of the test beam data and the lab calibration including voltage uncertainty effects and temperature uncertainty. Figure 9.3 on the right shows the residual with a spread of 3.6% showing the error of 1.5% quoted on the lab calibration is compatible with the test beam data.

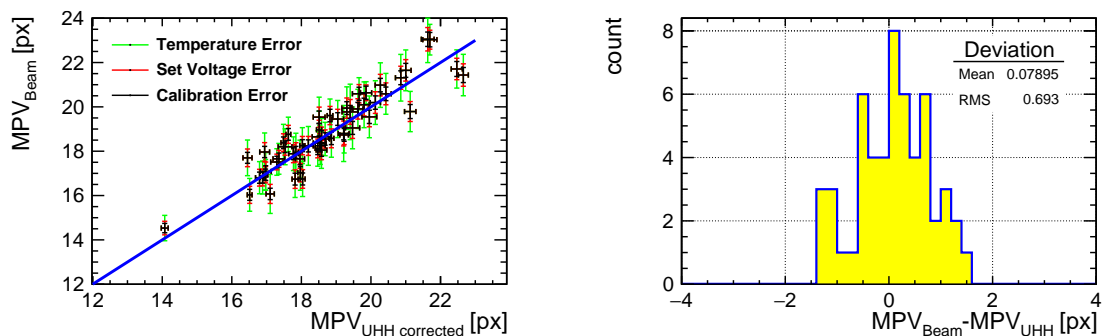


Figure 9.3:

Left: Correlation for all 54 measured channels. MPV_{UHH} has been corrected for the different energy depositions of the setup and the test beam, as well as the temperature. The uncertainty in setting the voltages yields an additional error shown in red. The error resulting from the temperature uncertainty of 4°C is shown in green. As a guide to the eye, the exact correlation is shown in blue.

Right: Deviation from the expected result in pixel for all measured tiles. The RMS of the distribution is 3.6% (0.7 pixel on the mean of 19 pixel)

Chapter 10

Operation Voltage Optimization

A variety of settings of the Spiroc2b enables the adaptation of the detector to the specific operational environment. Among other decisions a voltage needs to be chosen for the operation of the SiPM tile system of the University of Hamburg on the HBUs. This chapter will evaluate the possible modi and their consequences on the overall detector performance. The three batches have been equipped to a set of HBUs each. Batch 3 was not separated into batch 3a and batch 3b. In this chapter is thus only the overall performance of batch 3 reviewed since the operation voltage strategy is set commonly for each layer. Choosing an operation voltage depends first on the physics that the detector is supposed to measure. Secondly, the Spiroc2b imposes a number of restrictions on the measurable signal and the precision of the settings of the chip, e.g. the precision of the operation voltage, see chapter 8. The main figure of merit for the operation of a single detector unit is the energy calibration, the response (see chapter 7.1.2) to MIP particles. A chosen response defines the dynamic range of the photo detector. In figure 6.6 in chapter 6.4, the expected energies per detection unit are shown. A linear response to the deposited energy in the single tiles improves the overall detector precision, as described in [76]. If the saturation of the SiPMs is not taken into account the energy resolution decreases rapidly for higher energies. An exact knowledge of the SiPM saturation curve can counter this effect, but detailed calibration curves for all SiPMs are needed. Figure 10.1 shows as an example the impact of the saturation of SiPMs on the measured energy from a legacy AHCAL prototype for a CERN and FermiLab test beam campaign in 2006 - 2009. The energy per hit is shown with and without the correction factor applied, for 30 GeV electromagnetic showers. Whereas the correction is negligible for low signal amplitudes, it becomes significant at larger amplitudes, resulting in a strong correction for the tail of the distribution. For the maximum energy deposited in one cell for a 30 GeV electron the correction factor is 300%. More results about this analysis of the electromagnetic showers measured by the AHCAL can be found in [14]. A detailed simulation of SiPMs depending on Gain G , dark count rate DCR , correlated noise XT_{corr} , and response R has been developed in [46]. Figure 10.2 shows the simulated saturation curves for a tile-SiPM

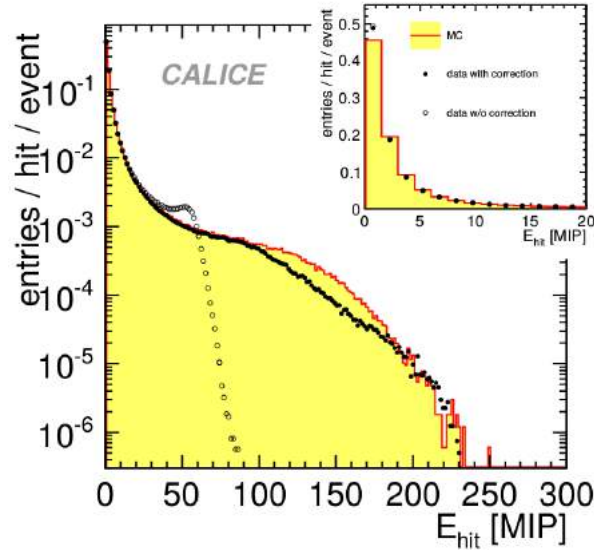


Figure 10.1: Hit energy spectrum for 30 GeV positron showers in the AHCAL. Open circles (dots) show the data before (after) correction for the non-linear response of the SiPM [76].

system with the parameters taken from table 7.3 at different responses. The line depicts the expected maximum energy occurring less than once for one shower in the detector for π^0 of 500 GeV, see figure 6.6. A response between 10 px and 20 px leads to a non-linearity of less than 15% at a signal of 50 MIP.

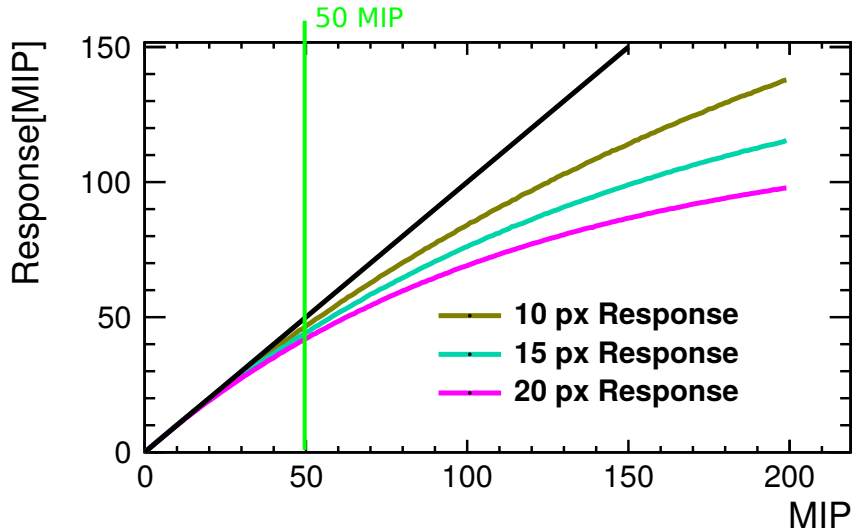


Figure 10.2: Simulated saturation curves for the Ketek PM 1125 for different responses of 10 px, 15 px, and 20 px fired per MIP. As a reference, in black the unsaturated curve ($\text{MIP} = \text{Response}_{\text{MIP}}$). The green line shows the maximum occurring energy once per event in the tiles, according to 6.6

10.1 Spiroc2b restrictions on the operational parameters

The Spiroc2b poses certain restrictions on the minimum and maximum signal per pixel from the SiPM. The lower limit for a detectable single pixel spectrum to determine the gain for calibration of the single cell is $0.2 \times 10^6 e^-$. The signal gain should not exceed $1 \times 10^6 e^-$ to prevent pedestal shifts. The limited resolution for setting the threshold and preamplifier gain in the Spiroc2b also need to be considered for the setting of the operation voltage for the three batches produced that are described in chapter 7.3. The dynamic range of the signal needs to be considered since the Spiroc2b has a fixed ratio of ≈ 10 between the two amplification paths. Depending on the range of the internal voltage adjustment used on the Spiroc2b, the precision of the voltage deteriorates, see chapter 8. Equation 8.6 calculates the uncertainty of the set voltage depending on the used range of the internal voltage adjustment. The considerable differences in response of the three batches, see figure 7.22, demand the optimization to be done separately per batch.

10.2 Methodology of the Optimization

The detailed data from the laboratory calibration is used to predict the behavior of the detector. For the different optimization strategies investigated in this chapter the optimization has been carried out for each single tile SiPM unit separately, that has been characterized in the laboratory setup. Averages and spreads of the results are presented.

10.3 Optimizing strategies for setting the bias voltage

Three optimizing strategies can be applied using the internal voltage adjustment. Every batch can be set to a desired mean response using one of the three optimizing strategies.

I: Fixed Voltage

To minimize the error on the set voltage the register value 0 is used for all SiPMs, providing the same voltage for all units. The spreads in the distributions are only dependent on the uniformity of the SiPMs and light yield tiles.

II: Fixed Over-voltage (OV)

All SiPMs are operated at the same voltage over breakdown to equalize their behavior. The gain will show a spread depicted in figure 7.16. The internal gain adjustment of the Spiroc2b can be avoided. The internal voltage adjustment of the Spiroc2b needs to be used only in a small range, see table 7.2.

III: Response equalization.

To simplify detector calibration and to homogenize the single detection units, all SiPM tile units will give the same response in pixel per MIP. The spread in gain is equalized by the internal gain adjustment. The complete voltage range of the Spiroc2b needs to be used which deteriorates the precision of the voltage.

Each of those optimization strategies is carried out for each detection element separately from the laboratory data.

	$V_{min} - V_{max}$	RegRange	$HV_{Precision}$
I	0 mV	0	16 mV
II	900 mV	60	40 mV
III _{10 px}	4.1 V / 4 V / 3.5 V	255 / 255 / 233	117 mV / 117 mV / 108 mV
III _{15 px}	2.5 V / 3 V / 3.1 V	166 / 200 / 206	82 mV / 95 mV / 98 mV
III _{20 px}	2.4 V / 2.5 V / 4.3 V	160 / 166 / 255	79 mV / 82 mV / 117 mV

Table 10.1: Different operational strategies and the needed voltage range on the Spiroc2b. Optimizing strategies **I**, **II**, **III** (for 10, 15, and 20 pixel) demands the use of different ranges of the internal voltage adjustment. The register range needed are shown and the resulting voltage error from equation 8.6. The three batches in black, red, and green have different ranges if the response is equalized while strategy **I** and **II** focus on SiPM properties that are the same for all batches.

Table 10.1 shows the required range of the internal voltage adjustment. Following equation 8.6, the uncertainty of setting the voltage is shown. In the range of 900 mV for setting the same over-voltage for all SiPMs includes 99 % of all SiPMs. Using Response equalization **III**, each batch needs to be treated separately (see mean response in figure 7.22, chapter 7.3). Figure 10.3 shows the spread of the response for the different operational strategies depending on the targeted mean response. Setting a fixed voltage (**I**) or fixed over-voltage (**II**) shows almost the same spread in response for all three batches. Equalizing the response of all tiles with strategy **III** implies using the whole range of the internal voltage adjustment. This introduces a spread of the order of 5 % up to 10 % in the response. Figure 10.4 shows the resulting gain spread for all three operational strategies. In the blue area more than 2 % of the SiPMs have a gain lower than 200.000. This gain is too low to resolve single pixel spectra with the Spiroc2b and cannot be calibrated. Using strategy **III** the wide spread of the gain for batches 2 and 3 make the use of the internal amplifier adjustment mandatory. The spread in gain of both distributions is under 15 %. Setting a fixed over-voltage should equalize the gain to 1 % but the use of the internal voltage adjustment widens the distribution. The spread in gain of both strategies is compatible with operation and compatible with the spread of the internal amplification of the Spiroc2b when using the internal amplifier adjustment. The spread in gain decreases when setting the same over-voltage (strategy **II**) compared to a fixed

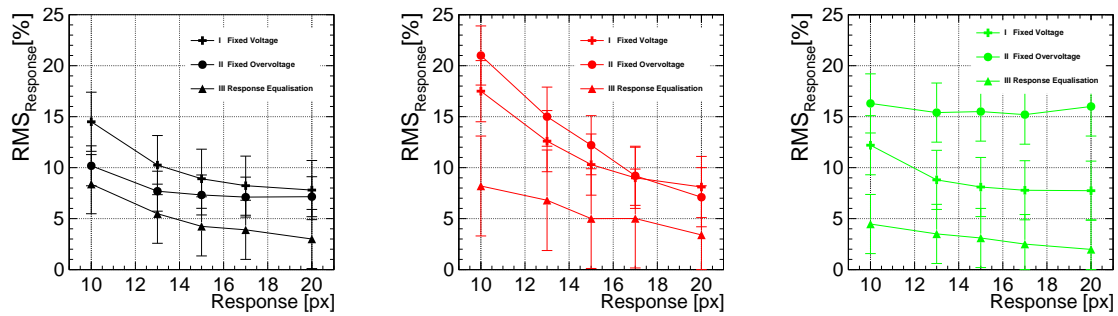


Figure 10.3: Spread of the response for different operational strategies for all three batches, **1** (left) **2** (middle) and **3** (right). The spread of the response including the spread of the set voltage from table 10.1.

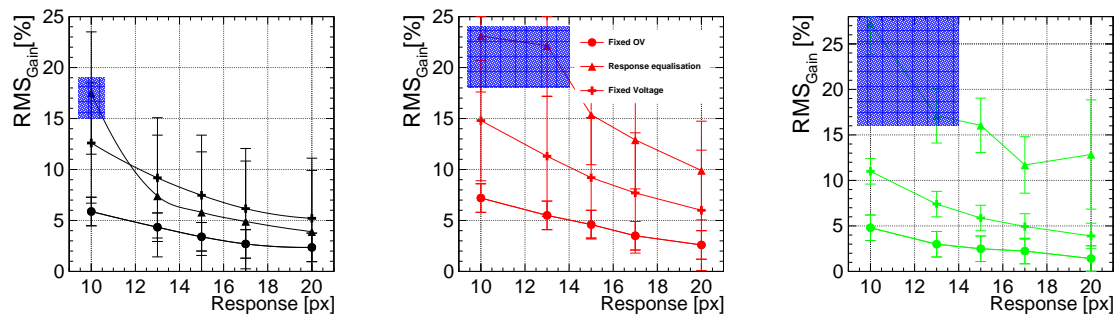


Figure 10.4: Spread of the SiPM gain for different operational strategies for all three batches, **1** (left) **2** (middle) and **3** (right). The spread of the gain including the spread of the set voltage from table 10.1. The blue area depicts data sets with a gain too low to resolve single pixel spectra for over 90% of the channels for operation with the Spiroc2b.

voltage (strategy **I**) for all SiPMs as can be seen in figure 10.4. The improvement does not justify the complex effort of measuring and setting the voltage for each SiPM individually. Because of the large spread in gain, strategy **III** demands the use of the single channel gain equalization with the internal amplification adjustment of the Spiroc2b. This leads to two additional parameters per channel that need to be set for operation. By comparing all three strategies that set the voltage for a given design response by setting all SiPM at the same voltages, strategy **I** is the most feasible option.

10.4 Optimization with fixed voltage (I)

Figure 10.5 shows the mean response of all three batches for strategy **I** with one fixed voltage for all SiPMs of one batch. Apparent is the degradation after heating the SiPMs to prevent the popcorn effect from batch 2 to batch 3.

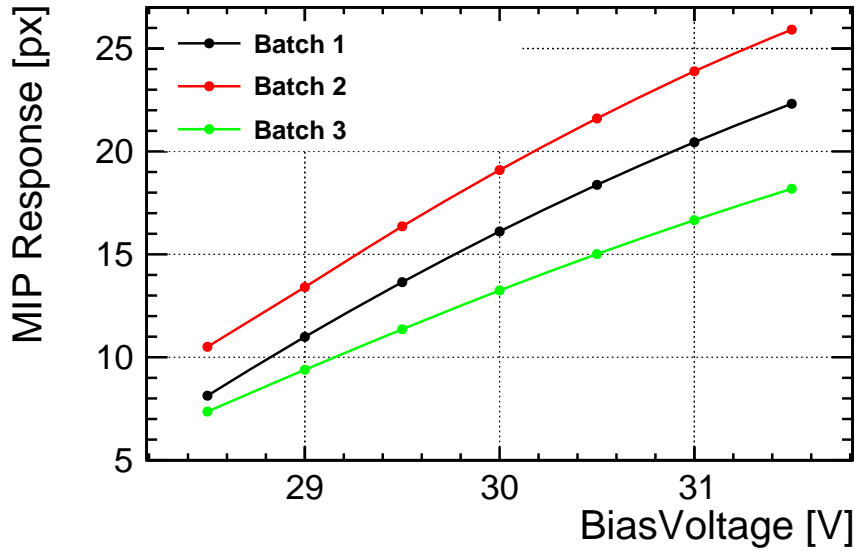


Figure 10.5: Mean response in pixel per MIP for different voltages using operational strategy **I** (fixed voltage/RegVal=0) for all three batches.

10.4.1 MIP efficiency

Detection efficiency is defined as the ratio of the total number of counts in the energy spectrum recorded by the detector by the number of MIP particles emitted by the detector. In this case the geometric efficiency is disregarded and only particles passing the detector count. As the trigger of the setup, see section 7.1.2 is independent of the signal in the TuT the efficiency of the trigger does not have to be taken into account. The particles that the setup triggered on are particles as simulated in figure 7.9. (Apart from noise hits from the setup that will be treated accordingly, see below). In this work, the MIP efficiency for a certain threshold t is thus defined as the portion of all triggered hits F to the amount of hits N_t that the TuT itself would have triggered upon for a threshold t ,

$$\epsilon_{MIP} = \frac{N_t}{F}. \quad (10.1)$$

A standard characterization measurement is seen in figure 10.6. The measurement has been rescaled to the MPV as 1 MIP. The data in blue would include the noise and zero counts as described in 7.1.2 and figure 7.12. Using the data to calculate the integrals would turn out a worse efficiency than the actual tile system provides. This method still underestimates the efficiency since the actual shape of a MIP signal, see figure 7.9 is narrower than the measurement. Using the Landau-Gaussian fit described in chapter 7.1.2 the efficiency is

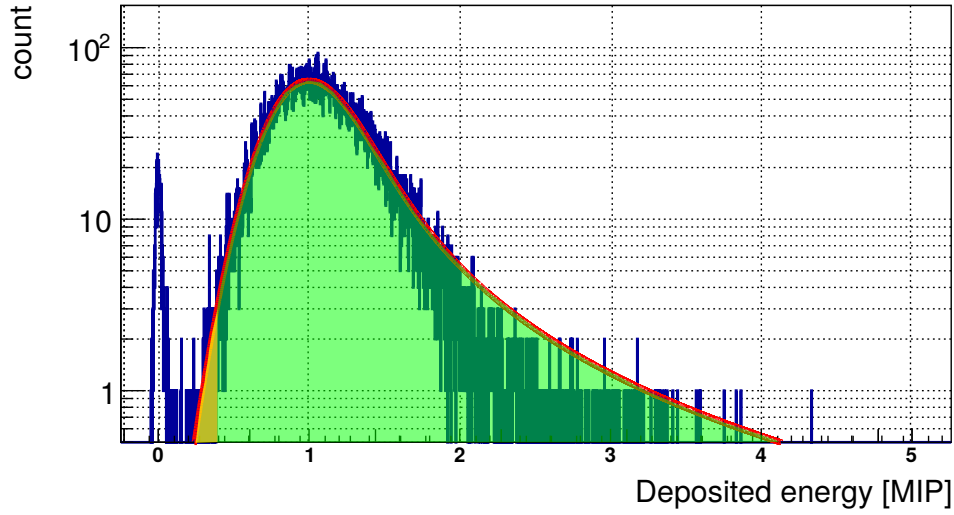


Figure 10.6: Sample measurement of tile 604. The efficiency is calculated as the ratio of signals below and above threshold, in this case 0.3 MIP. In blue the data. The green area depicts the signals over threshold while the yellow are is the part of the signal that is lost with this threshold setting. The measurement has been rescaled to the MPV as 1 MIP.

calculated. In figure 10.8 was extracted using

$$\epsilon_{MIP} = \frac{\int_t^{\infty} F_{(fit)}(x)dx}{\int_0^{\infty} F_{(fit)}(x)dx}. \quad (10.2)$$

$F_{(fit)}(x)$ is the fit to the response function in section 7.1.2 expressed in MIP. The corresponding threshold t is also expressed in MIP. This excludes the zero and partial counts from the measurement and approximates the tail of a true Landau-Gaussian function as will be seen in a true MIP signal compared to the actual laboratory measurement. With an actual MIP distribution being narrower than the distribution from a ^{90}Sr source the efficiency is greatly underestimated in this measurement.

10.4.2 Noise over threshold

Following equation 7.5 the noise over threshold can be defined as

$$DCR^t = - \frac{\ln(1 - P_t^n(t_{gate}^{eff}))}{t_{gate}^{eff}} \quad (10.3)$$

for a gate length t_{gate}^{eff} . P_t^n is the normalized fraction of events with pulse charges corresponding to t or more pixel fired. Figure 10.7 is a time consuming high statistic pedestal with five million entries. Due to the low noise of the SiPMs investigated here the amount of entries over a few pixel threshold is not representing the true noise distribution anymore. Furthermore even in a measurement with more entries the noise over threshold will be in the same or smaller as

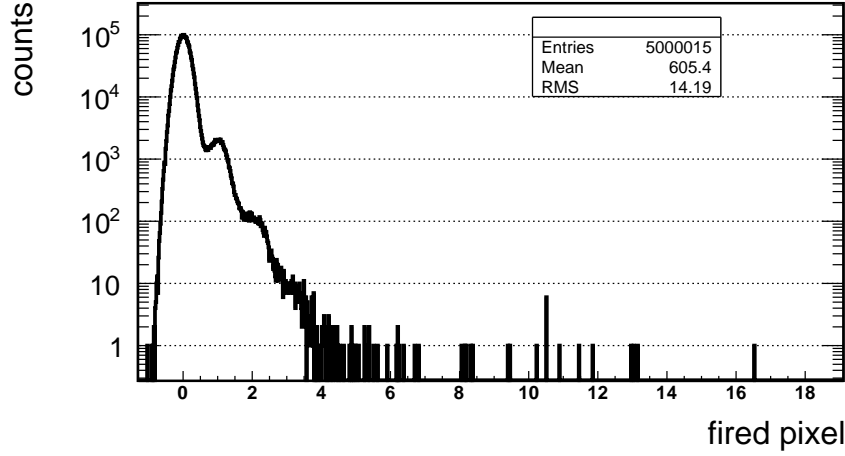


Figure 10.7: Sample measurement of tile 604 with $5 \cdot 10^6$ entries. Even a time consuming measurement with million of data points does not yield more than a few entries over a threshold of several pixel. The higher energy signals are also dominated by cosmic Muons rather than SiPM noise.

cosmic muon signals (0.15 s^{-1} , see [23], in a tile of $3 \times 3 \times 0.3 \text{ cm}^3$). To estimate the SiPM noise over threshold it is (wrongly) assumed that the correlated noise caused by any pixel is, following equation 7.6,

$$XT_{corr} = \frac{\sum_{k=2}^{\text{inf}} P_k^n}{P_1^n} = \frac{\sum_{k=t}^{\text{inf}} P_k^n}{P_{t-1}^n} \quad \forall t \in \mathbb{N} \ t > 2 \quad (10.4)$$

This does not take into account the geometrical occupancy of the SiPM pixels since neighboring pixels that are already fired do not contribute to the signal anymore. For a more detailed view on this topic see [77]. For a low occupancy of a few pixels in a SiPM this assumption is feasible. Following chapter 7.1.1

$$XT_{corr} = \frac{1 - (P_0^n + P_1^n)}{P_1^n} = \frac{1 - (P_0^n + P_1^n + \sum_{k=2}^t P_k^n)}{P_t^n} \quad \forall t \in \mathbb{N} \ t > 2 \quad (10.5)$$

From here the probability P_t^n is

$$P_t^n = \frac{1 - (P_0^n + P_1^n + \sum_{k=2}^{t-1} P_k^n)}{XT_{corr} + 1} \quad \forall t \in \mathbb{N} \ t > 2 \quad (10.6)$$

. With equation 10.3 the noise over threshold DCR^t can incrementally be calculated as

$$DCR_t = -\frac{\ln(1 - \frac{1 - (P_0^n + P_1^n + \sum_{k=2}^{t-1} P_k^n)}{XT_{corr} + 1})}{t_{gate}^{eff}} \quad \forall t \in \mathbb{N} \ t > 2 \quad (10.7)$$

. Figure 10.8 on the right shows the resulting approximated and overestimated noise for a single SiPM Tile system. The data used to extract XT_{corr} as mentioned in chapter 7.2,

table 7.3 was taken from batch 3. The response of batch three at the same operating voltages is lowest compared to the other batches. The efficiency for the other batches is higher while the noise over threshold will be lower. A MIP efficiency over 95% can be reached with a threshold of 0.5 MIP by choosing a target response roughly over 15 px. With a threshold of 0.3 MIP, the efficiency lies always above 97%. The rough estimate of the noise over threshold with either 0.3 or 0.5 MIP shows practically no noise that would enter data taking. The hardware threshold in the Spiroc2b can only be set roughly since a detailed calibration of the setting would require a channel wise calibration of the threshold. For setting a safe threshold, ensuring that all channels are below 0.5 MIP threshold, an actual threshold of 0.3 MIP is realistic. This increases the noise over threshold, which will not enter the data after an off-line cut but will affect the data taking and readout rate especially for low rate test beams. For the beam rates expected at ILC, a noise free operation of the SiPMs is expected. A target response of 18 pixel per MIP was chosen as the operational point. This ensures all channels have a gain safe to calibrate the single SiPMs while maintaining a virtually non-existent noise over threshold. The preamplifier and threshold settings of the Spiroc2b at this voltages are several steps from the maximum settings to ensure some flexibility during test beam operation.

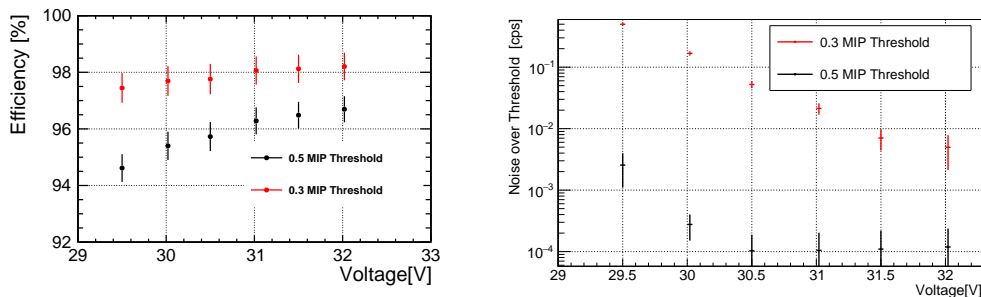


Figure 10.8: The extended calibration data taken for batch 3 enables an estimate of efficiency and noise over threshold.

Left: Estimated mean efficiency for threshold of 0.5 and 0.3 MIP following equation 10.2

Right: Estimated noise over threshold. The noise over threshold is overestimated.

10.5 Operational parameters for 18 px per MIP response

A voltage of 30.4 V for batch 1, 29.8 V for batch 2, and 31.2 V for batch 3 have been chosen to result in a mean of 18 px per MIP. Figure 10.9 on the left shows the resulting distribution in the response for all three batches. Due to the different response behavior, the resulting gain, as seen in figure 10.9 on the right, is different for each batch while the batch-wise distributions are very narrow. Three different preamplifier settings have to be used, one for each batch. Table 10.2 shows the figures of merit for the operation at the chosen voltages.

The spread in response, if not calibrated channel wise will enter the constant term of the calorimeter resolution, see equation 3.7. In the AHCAL detector in ILD a typical hadronic shower extends over 1m^3 . Table 10.2 on the right shows the estimated overall noise in a 1m^3 ILC AHCAL under ILC conditions (bunch length of 200 ns per event), with 28800 SiPM tile detection units. The resulting error entering the calorimeter resolution will be under 1%. The gain spread is in the order of the amplifier spread of the Spiroc2b and one preamplifier setting suffices for operation. The noise over threshold for 0.5 MIP is virtually non-existent.

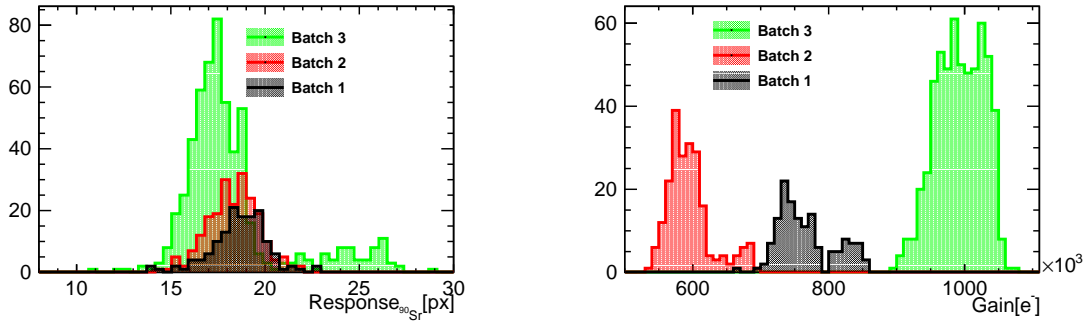


Figure 10.9: gain and response for all measured tiles with a design response of 18 px that use a fixed voltage per batch, see table 10.2

Left: All three batches are optimized to have the same mean response. The additional spread in batch 3 induced by the popcorn effect, see chapter 7.3, widens the distribution.

Right: gain distribution for all three batches at operation voltages.

Batch	Bias	Response	RMS	Gain	RMS	DCR	RMS	Efficiency	1m^3 noise events, 0.5 MIP threshold
1	30.4 V	18.6 px	7.9 %	766×10^3	5.4 %	20×10^4 cps	17 %	98.5 %	0.14
2	29.8 V	18.4 px	7.4 %	595×10^3	5.5 %	19×10^4 cps	19 %	99.2 %	0.15
3	31.2 V	18.2 px	15 %	993×10^3	3.5 %	30×10^4 cps	10 %	98.0 %	0.22

Table 10.2: Operational parameters for design response of 18 px and 0.5 MIP threshold

Uncertainty of setting the voltage according to equation 8.6 with $\text{RegVal}=0$ are included

Efficiency and noise over 0.5 MIP threshold are extrapolated using the detailed available data from batch 3 scaling the response

Operating the tile and SiPM system of the University of Hamburg on the HBU equipped with Spiroc2b requires only one voltage common to all SiPMs. At a target mean response of 18 px per MIP, the spread in operational parameters requires no further channel or chip wise adjustment of the Spiroc2b. The MIP efficiency is above 98%. Using one common response calibration for all channels will result in an error of 8% for a single channel. The negligible noise per event guarantees an effective shower separation.

Chapter 11

Time measurement with the Spiroc2b

Hadronic showers show a complex time structure in hadronic calorimeters, see the detailed description in Chapter 3.1.5. The time structure extends from instantaneous signals of ionization by relativistic hadrons and electromagnetic showers to slow delayed signals from slow neutrons and nuclear de-excitation following neutron capture or spallation. Especially in high repetition rate and high background environments, the knowledge and measurement of the time evolution of hadronic showers in the calorimeter is advantageous for detector operation. In a future ILC, hadronic mini-jet events will cause a significant pile-up of hadronic background, which deposits more energy than a real physics event [78]. Hadronic background is also produced via photo-nuclear interaction in the forward instrumentation of the ILC [79]. This background can be substantially reduced by the use of time resolved particle flow reconstruction [80] with timing cuts on the ns level. A detailed and precise simulation model in GEANT 4 is needed for the development and prediction of the behavior of an ILC calorimeter. The detailed investigation of the spatial development of hadronic showers with the first series of test beams of a full cubic meter AHCAL [62] operated at test beam 2006-2012 gave a deep insight into the precision of GEANT 4 physics models. The CALICE collaboration conducts an ongoing investigation of the time development of hadronic showers with a dedicated setup, the T3B (Tungsten Timing in Test beam) experiment. T3B is a precision measurement experiment with a small amount of channels that has been specifically developed for test beam campaigns [31]. The time evolution of hadronic showers in calorimeters with different absorbers and detection media has been investigated in detail [81]. This work focuses on one layer of the engineering prototype program of the CALICE collaboration ([82], calibration and more details in [64]) with the Spiroc2b commissioned in 2012. One layer of a now older obsolete tile design (details in the following sections) with 576 channels on four HBUs had been commissioned to serve as one layer of an hadronic calorimeter in test beam scenarios inside other full scale prototypes of the CALICE collaboration. The detector took data in 2012

in the SPS test beam at CERN in a combined setup with the one cubic meter DHCAL [83] calorimeter prototype with tungsten absorber. In the following the detailed calibration of the time measurement with the Spiroc2b chip is explained. The calibration as carried out here is not intended as a blueprint for a calibration of a full scale ILC AHCAL. The goal is to determine the best possible time resolution with the Spiroc2b for test beam use to validate GEANT 4 physics lists and to provide a detailed full data set for future investigations of simpler calibration strategies. All this work is only done in test beam mode with reduced clock cycle speed of 250 kHz leading to a ramp of 4 μ s. This reduces the theoretical time resolution from 50 ps (in ILC mode) to 1 ns. In 2012 a single calorimeter layer (shown in Figure 11.1 on

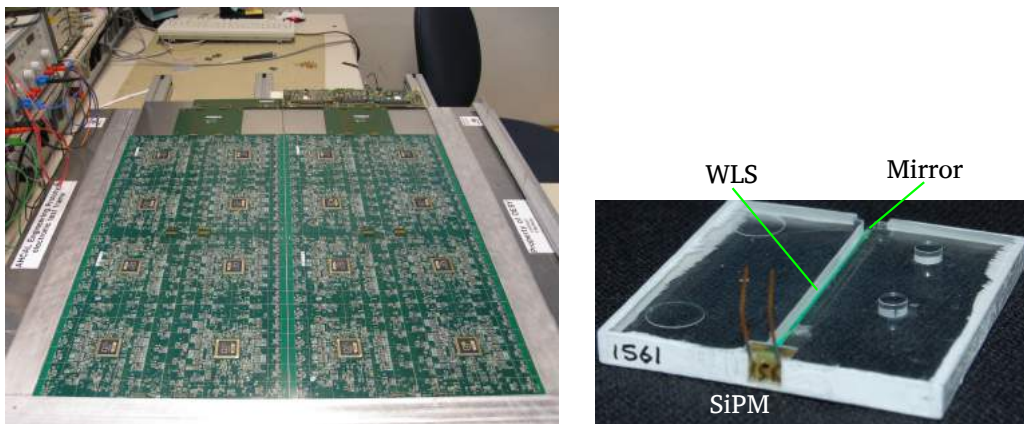


Figure 11.1:

Left: One layer engineering prototype in cassette used for test beam. 576 channels on 4 HBUs with 16 chips. To fit the absorber structure of the test beams two extender boards and one side interface board (SIB) have been used to interconnect the HBUs.

Right: ITEP tile used in this setup with wavelength shifting fiber (WLS) and mirror to convert and direct the blue scintillation light to the green sensitive CPTA SiPM. For more details on the tile design see [84].

the left) with 4 HBUs and 576 channels was commissioned. The tile and SiPM technology used consisted of a now (with the possibility of blue sensitive SiPMs) obsolete design with green sensitive SiPMs. The SiPMs were designed and build by CPTA SiPM [85] with 796 pixels with 40 μ m pitch. The tiles in Figure 11.1 on the right consisted of a plastic scintillator (poly-terphenyle plus POPOP dissolved in polystyrene, BASF130) manufactured by UNIPLAST with an embedded wavelength shifting fiber (Y11) to transform the blue scintillation light into green. A mirror on the opposite site of the SiPM guided the light back on the SiPM. The SiPMs showed a big spread in operational parameters. They were optimized at SSC RF ITEP in Moscow to have a response of 15 px per MIP at 22°C and an operating voltage was defined. Table 11.1 shows the mean voltage and the spread of the resulting parameters. Using the internal voltage adjustment of the Spiroc2b, a channel-wise voltage calibration was necessary. As discussed in Chapter 8, the method was error prone due to frequent crashes. Therefore a mean value was chosen for many channels where the calibration failed, widening the spread of parameters. The wavelength shifting fiber could not be placed exactly on top of

the sensitive area of the SiPM resulting in a strong variation in maximum number of pixels for saturation per SiPM as shown in table 11.1. The channel-wise sensor-gain adjustment was used to operate the detector despite the varying SiPM-gain. The next sections describe

	Op. Voltage	$V_{min} - V_{max}$	Gain	DCR	noise above 0.5 MIP	pixel _{max}
Mean	36 V	6.5 V	900×10^3	645×10^3 cps	10 cps	851 pixel
RMS	2.3 V	-	26 %	60 %	45 %	10 %

Table 11.1: CPTA 2012 SiPM Figures of Merit and spread at 22 °C as provided by manufacturer. For more details on the measurement and SiPMs [85].

the TDC calibration of this prototype in detail and evaluate the best possible time resolution with this setup.

11.1 Hit timing measurement in the Spiroc2b

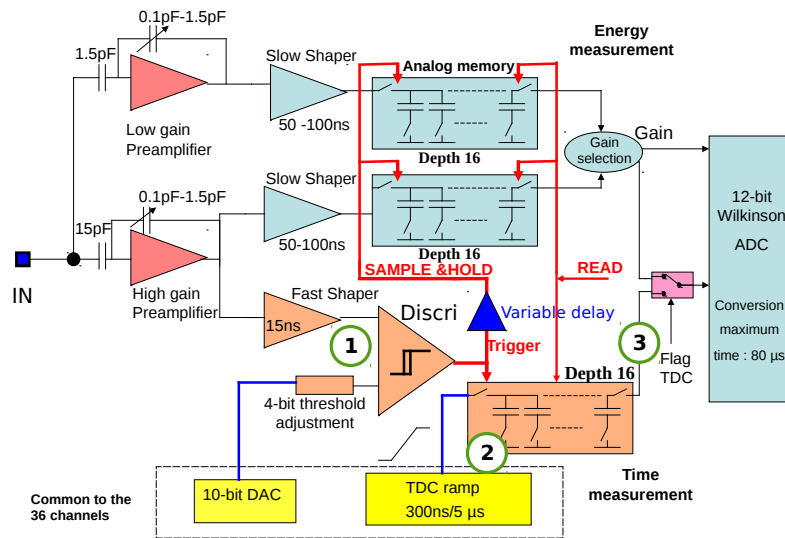


Figure 11.2: Time measurement with the Spiroc2b. The input signal after amplification is passed through a 15 ns fast shaper with a much shorter shaping time than the ones used for the analogue signal generation.

- 1 A programmable threshold discriminator triggers on this signal.
- 2 Two analogue voltage ramps are alternated between the chip cycles. On a trigger, the actual voltage is transferred with a sample and hold to the analogue memory-cells.
- 3 After a readout is triggered by a full chip or timeout, the charge of the memory-cells is transferred and converted via the Wilkinson ADC with 12 bit resolution.

Following section 6.3.4, the principle of the time measurement of the Spiroc2b is laid out

in more detail. In Figure 11.2 at point **1**, the signal after amplification is split and passed to a shaper with 15 ns characteristic shaping time. An adjustable discriminator determines a trigger if the voltage exceeds the set threshold. Due to the non-zero raise time of the shaper, a time slew corresponding to the voltage of the signal is expected to take place. Signals with higher amplitudes pass the threshold earlier than those with low amplitudes though the signals are produced at the same time. This correction is discussed in section 11.2.3. It is worth noting that the signal of the fast shaper is not accessible with the current chip design. Only the signal passed through a different shaper with much longer shaping time (50 ns-100 ns) is saved as the energy measurement. This signal does not correspond directly to the triggered one either because of electronic effects or consecutive physics signals after a hit. This can lead to triggered signals with a lower ADC value than expected or no trigger on a channel with high ADC value. The time of hit is determined by sampling an analogue voltage ramp. For each cycle of the Spiroc2b, a voltage is ramped up. Two voltage ramps with different characteristics are produced to avoid dead time in a new cycle and switched between cycles as described in Figure 11.3 on the left. The two voltage ramps show distinct different characteristics in slope as can be seen in Figure 11.3 on the right for a sample chip. The

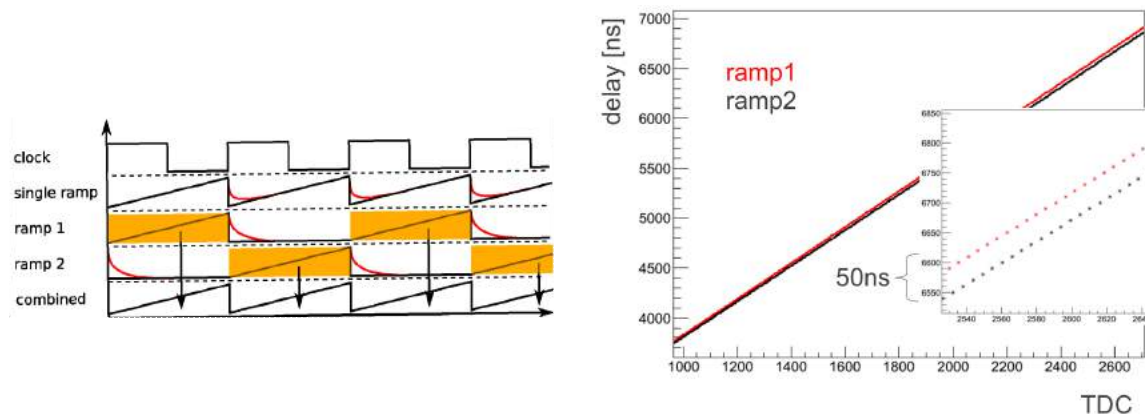


Figure 11.3:

Left: Ramp production principle of the Spiroc2b. To avoid dead time during the return to 0 V, two ramps are alternated with each clock cycle [86].

Right: The two ramps from the same channel. The difference between the ramps can clearly be seen and accumulates for higher TDC bins to over 50 ns (details in section 11.2.1)

difference between the slopes would result in more than 50 ns difference. A simple conversion from ADC units to time is not possible and each unique ramp (two per chip) needs to be separately calibrated. The trigger from the discriminator starts a sample and hold circuit (**2, above orange box** in Figure 11.2) and the value is transferred to the analogue memory cells. Each of the memory-cells has a unique offset value and behavior which is discussed in section 11.2.2. Storage over a prolonged period of time (100 μ s) leads to non-negligible loss of stored charge, which render the stored information useless. After a readout is triggered by a

full memory or an external timeout, the values in the memory-cell register are consecutively converted via the same Wilkinson ADC as the energy amplitudes. A channel triggers only on the first hit over threshold produced during the 15 ns shaping time of the fast shaper. Consecutive hits during the delay of the slow shaper are added up for the energy information. The energy measured in a triggered channel is thus the sum of all hits that occurred during the hold time. With the 12 bit ADC, the theoretical resolution is $50 \frac{\text{ps}}{\text{bin}}$. In order to use all features of the ASIC and accommodate for low events rates like CERN and DESY test beams, the clock is reduced from 5 MHz to 250 kHz. This reduces the theoretical time resolution to 1 ns. For an ILC AHCAL, the detector will run in sync with the beam at high rates and a fixed time reference frame is given. In most test beam scenarios, the detector runs asynchronous with the beam at low test beam rates e.g. the PS or SPS test beam facilities at CERN. A fixed time reference is needed if the detector runs asynchronous, e.g. time of the first hit in a detector with several layers or an external time reference that triggers a channel inside the detector. Figure 11.4 shows the setup used for all test beams. The coincidence of two

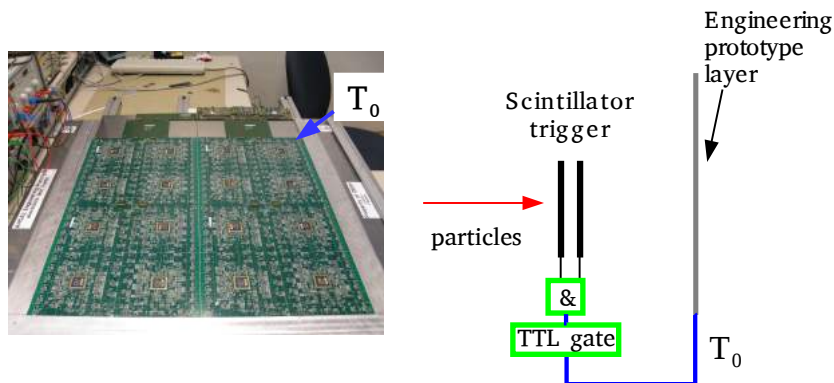


Figure 11.4: Trigger setup for the AHCAL Layer.

The detector clock is running independently of the test beam cycles. The coincidence of two scintillator plates read out with PMTs is used as an external time reference.

scintillator plates read out with PMTs and threshold discriminators provide an external time reference. The coincidence window is 10 ns and produces an attenuated TTL signal that is capacitively coupled directly into a single channel on one Spiroc2b (channel 35 of chip 137). The trigger channels are not corrected for time slew effects and a jitter naturally occurs with the $30 \times 30 \text{ cm}^2$ plates. This worsens the time resolution to determine the time of hit in the detector further. The time reference provided has an offset in time around 300 ns due to the processing speed of the electronics and cable delays. The details of the data treatment are discussed in section 11.2.2.

11.2 TDC calibration

This section is a detailed investigation of the effects of the Spiroc2b time measurement. The hit time is reconstructed from the TDC time-stamp with all effects of the Spiroc2b chip that have a major impact on the time resolutions are approximated as

$$\begin{aligned}
 t[ns] = f_{i,j}(A_{i,j,k}^{TDC} - P_S^{TDC}(N)) + P_{i,j,k}^{off} + Ts(A_{i,j,k}^{ADC} - P_{i,j,k}^{ADC}) - T_0[ns] \\
 i = \text{chip [129..145]} \\
 j = \text{channel [0..35]} \\
 k = \text{Memorycell [0..15]}
 \end{aligned}
 \tag{11.1}$$

The different contributions are:

$P_S^{TDC}(N)$ is a baseline shift of the TDC measurement caused by the occupancy of the chip. Depending on the number of triggers above threshold N , the TDC time measurement shifts to lower values.

$f_{i,j}$ Each chip produces two unique analogue voltage ramps that are alternated per $cycle = 1/0$. 32 ramps for 16 chips need to be measured. The calibration transforms the amplitude $A_{i,j,k}^{TDC}$ of the time measurement into absolute time in ns. In this work $f_{chip,cycle}$ are lookup tables interpolating the laboratory calibration data.

$P_{i,j,k}^{off}$ The analogue memory-cells of each channel show a unique offset in ns for hits that occur at the same time. 9216 offsets need to be calibrated. Some cells also show a non reproducible behavior and need to be identified and excluded from the analysis.

$Ts(A_{i,j,k}^{ADC} - P_{i,j,k}^{ADC})$ The timeslew (T_s) effect occurs if the occurrence in time of a signal is determined by a threshold discriminator. A signal with non-zero raise time passes the threshold faster depending on the amplitude ($A^{ADC} - P^{ADC}$) although the occurrence of the signal is the same in time.

T_0 is an external time reference in ns for the asynchronously running detector. For this work, a separate channel of one chip (137,35) was fed with a TTL signal from a trigger unit representing an absolute time reference for events. This channel is fed with a fixed amplitude signal so only $f_{137,35}(A_{137,35,k}^{TDC} - P_{137,35}^{TDC})$ and $P_{137,35,k}^{off}$ are relevant to it.

The next sections provide detailed investigation of each term and the calibration strategy used in this work.

11.2.1 Ramp extraction $f_{i,j}$

A NI-DG456 digital pulse generator with four channels was used for the chip-wise ramp extraction. Each channel provided a negative 0.2 ns long TTL pulse attenuated with 40 dB and soldered via a decoupling capacitor on one channel 35 for four chips at a time, three for calibration and chip 129 for time reference. The pulse generator was externally triggered by the DIF board and the Spiroc2b in auto-trigger mode, so each hit over threshold carries a Hit-Bit flag in the data stream. The ramps are sampled by varying the delay of the channels with respect to the DIF signal. Triggering the pulse generator externally generated a delay of several 100 ns so only the following two DIF cycles can be scanned: one even and one odd BXid. Using a fixed pulse height prohibits time walk effects and pedestal shifts. Memory cell-wise effects are averaged out due to the equal distribution of the pulses when externally triggered. Only one channel per chip is triggered. All effects in equation 11.1 are excluded, apart from $f_{i,j}(A_{i,j,k}^{TDC} - P_{i,j}^{TDC})$. Equation 11.1 simplifies to

$$t[ns] = f_{i,j}(A_{i,j,k}^{TDC} - P_{i,j}^{TDC}). \quad (11.2)$$

The Spiroc2b threshold is set high and the pre-amplification low. Figure 11.5 shows the resulting ADC spectrum for all chips. The first memory-cell ADC readout is always 0 due to a error in the chip design and needs to be discarded. The capacitive coupling also triggers on the falling edge under threshold which is removed with a cut $ADC > 500$ in the data. The raw data extracted from the fit is shown in the left side of Figure 11.6 for one channel. The broad main distribution shows the effect of the memory-cell offset. The ramp switching timing on the Spiroc2b has a time jitter, randomly moving the switching point as can be seen in Figure 11.3. The ramp calibration data is extracted using the mean TDC value for each time bin. Outliers would have a substantial impact on the calculation of the mean. Arbitrary TDC cuts following the main sensible data entries, see equation 11.3, have been introduced to cleanse the data from those outliers. The right side of Figure 11.6 shows the cleaned data selection for one ramp.

$$\begin{aligned} ADC &> 500 \\ 3500 &< Delay < 7420 \\ (Delay/2 - 1700) &< TDC < (Delay/1.9) \end{aligned} \quad (11.3)$$

For each sampling point the mean is taken as a data point, extracting two ramps per chip, see Figure 11.6. Figure 11.7 shows the residual on an independent data set with 1 ns step size for a linear fit and a point-wise interpolation from 100 ns step sampled ramps. The point wise interpolation was chosen for this work to achieve the best possible time resolution. A total of 72 data points have to be stored for each chip (100 ns step size for the ramp), 1216 in total for the whole detector. A feasible calibration scheme for a full ILD detector would

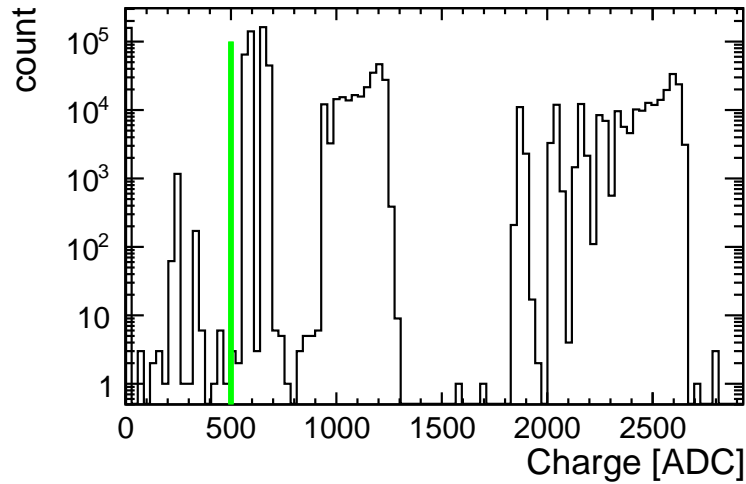


Figure 11.5: ADC spectrum for four channels of four chips. All ADC values are in one histogram. The four areas (two close to 500, 1000, and 2000-2500) are the trigger signals of the four channels. Due to the capacitive coupling of the generated pulse, the Spiroc2b also triggers on the falling edge of the calibration pulse leading to low ADC values. A cut of 500 ADC channels removes most of the unwanted triggers.

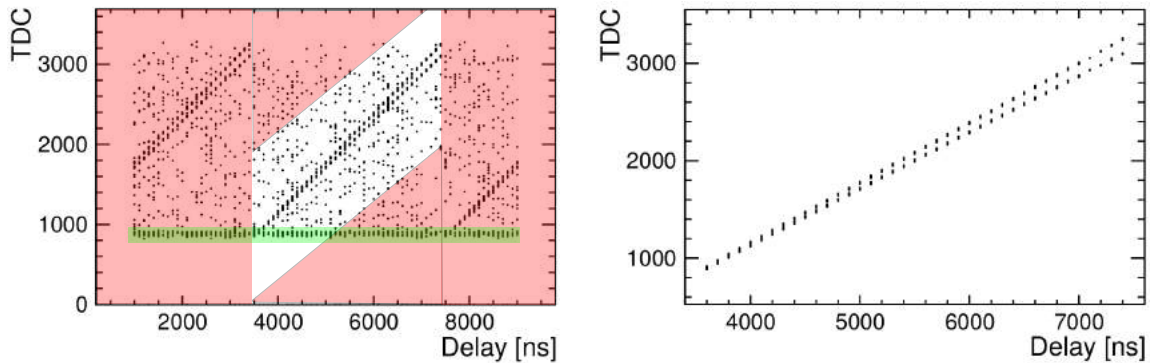


Figure 11.6:

Left: Raw calibration data using the pulse generator on one channel of the Spiroc2b. The light red area are the cuts from equation 11.3. The light green area is cut by the $ADC > 500$ cut on the energy amplitude.

Right: Cleaned data using the cuts from equation 11.3. The difference for the two different ramps for the cycles can be seen.

(chip 129, channel 35)

have two linear ramps per chip, worsening the linearity of the calibration. Especially for the use in test beams and validation of physics lists, the detector runs independent of the beam cycle. In the current setup, any time measurement can only be referred to the measurement of another channel. Figure 11.8 shows the time difference after calibration of two channels that are triggered with the pulse generator at the same time with all calibrations applied. Only the first memory-cells are considered, removing the individual memory-cell offset. Figure 11.8 represents the highest achievable electronics only time resolution of 1.7 ns, with the Spiroc2b

measuring the time difference between two digital signals.

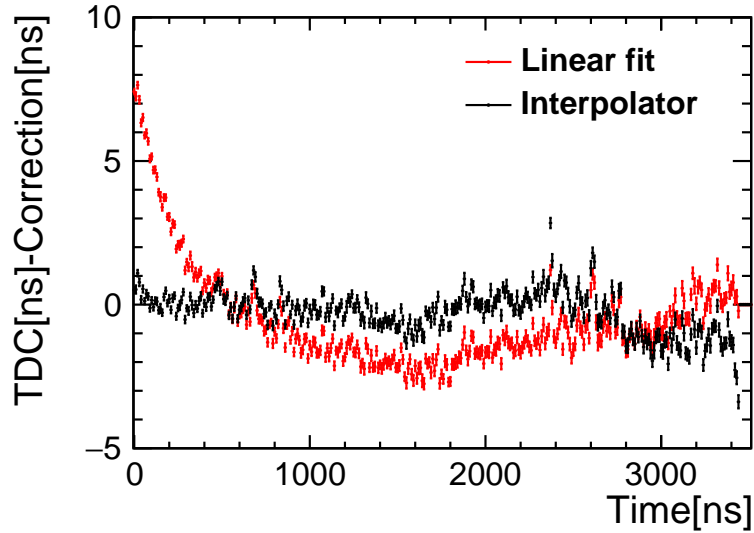


Figure 11.7: Comparison of different TDC ramp calibrations. A 100 ns spaced data set is used for calibration. An independent data set with 10 ns spacing was used to produce the deviation plots.

In red: A linear fit performed on the 100 ns spaced data is used for the ramp calibration. The data taken in the first 1 μ s of the ramp would need to be excluded from the analysis.

In black: A point to point interpolation is used as a calibration. Applying the calibration the independent data set shows instabilities of a few ns.

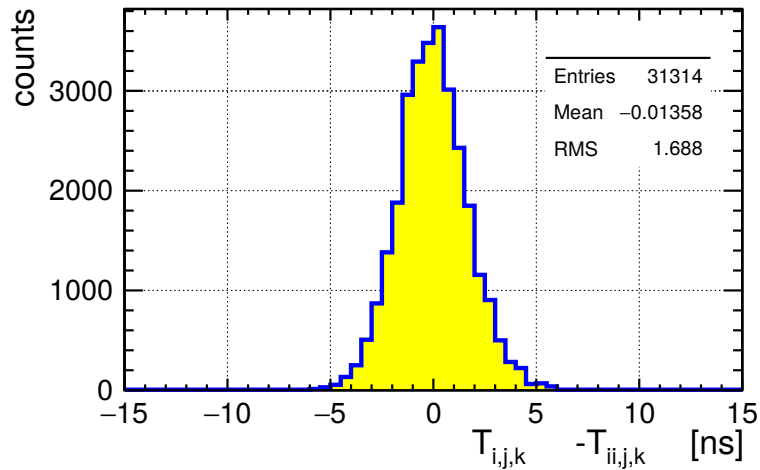


Figure 11.8: Electronics time resolution of the Spiroc2b.

With $i=129, ii=137$ being two different chips and $j=35, k=1$ indicating same channel and same memory-cell for both chips triggered at the same time with a digital pulse generator. The time difference after calibration is shown.

11.2.2 Memory-cell Offset $P_{i,j,k}^{off}$

9216 memory-cell offsets need to be calibrated. It is not a feasible option to check each channel separately with a pulse generator. Each memory-cell should have at least a few thousands hits to be able to extract the memory-cell offset and validate its proper operation. The signal should be generated by passing particles to include all effects of the SiPMs and tiles. Producing electromagnetic showers from an electron test beam just before the prototype layers will yield hundred of instantaneous particles and subsequent hits in the detector. During a test beam campaign in 2012 at the DESY II test beam facility to validate the function of the prototype beam time was allocated for the calibration of the TDC of the 16 Spiroc2b. Figure 11.9 on the left shows the setup. A aluminum block of 30 cm length ($3.3 X_0$) was placed in front of the detector to produce prompt electromagnetic showers from 3 GeV electrons. Figure 11.9 in the middle shows a sample shower produced by one electron. The detector was moved to get sufficient statistics over the whole area to five positions. Figure 11.9 on the right shows the accumulated hit map on the whole layer. Figure 11.10 shows the spectra

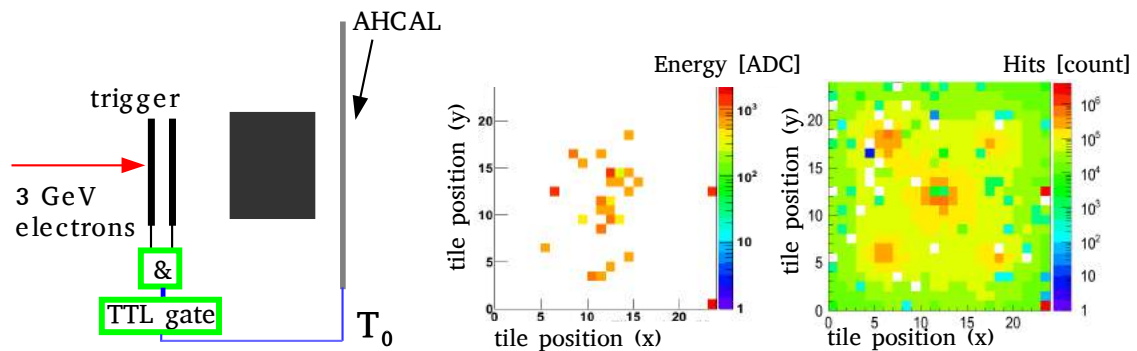


Figure 11.9:

Left: Setup for memory-cell calibration at the DESY II test beam. A 30 cm aluminum block is placed at five different positions in front of the detector. The coincidence of two trigger scintillators in front of the block is used as time reference signal and fed into two channels that can be seen in the hit map as the red channels to the right.

Middle: Hit map of a single shower produced. The two red channels to the right are the trigger channels. The color indicates the hit energy in ADC bins.

Right: Accumulated hit map for all runs. The five positions (middle and the four corners) where the aluminum block was placed are visible. The two red channels are again the trigger channels.

of the energy and time bin treatment for the offset analysis. To avoid the time slew effect a narrow 100 bin window has been chosen around the main ADC peak position. This way a maximum amount of statistics could be obtained while minimizing the time slew effect. An arbitrary offset depending on the MPV of the distribution is introduced. This offset is later compensated by shifting the time of hit according to the time slew correction. As can be seen in Figure 11.6 entries with TDC bins lower than 1000 bins are meaningless. A first analysis showed a delay of around 140 ns on the trigger channels. A cut of 500 TDC bins before the last

possible trigger hit (3000 bins) prevents noise from a validation gap at the end of the ramps. The resulting TDC spectra is homogeneously distributed over the range of 1000-2000 TDC bins. Figure 11.12 shows an obtained hit time spectrum after the ramp correction and the cuts discussed above for one cell. The mean is taken as the offset for this specific memory-cell around ± 100 ns of the main peak. An even distribution over all TDC bins ensures that any effects of non-linearity are evened out over the whole range of the TDC. Due to the nature of an electromagnetic shower, it is not possible to cut on the number of triggers per chip to exclude the pedestal shift effect in 11.2.4. For the extraction of the memory-cell offset, this effect is ignored and is later corrected. Following cuts on the trigger channel have been

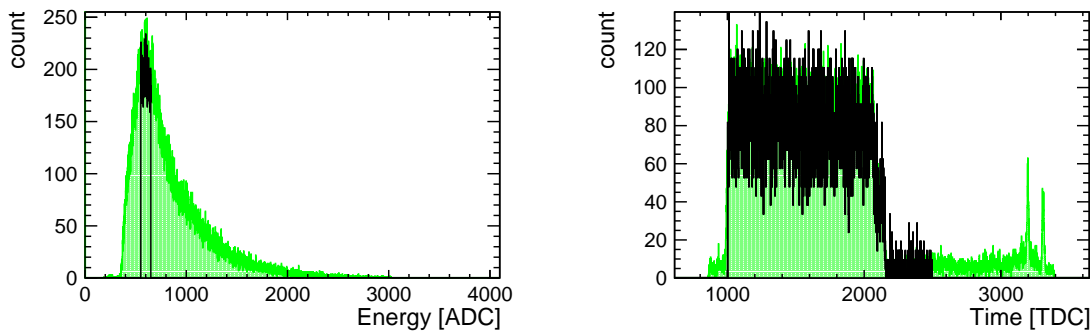


Figure 11.10: Cuts on the ADC and TDC spectra of one channel. All trigger cuts for the trigger used in equation 11.4 already implemented in the green curves. Full cuts on the channel data from equation 11.5 result in the black curves.

Left: The ADC spectra is cut in a narrow 100 bin window around the main peak of the energy contributions to excluded any time walk effects.

Right: TDC spectra in green with trigger cuts only. The SiPM noise in the validate event dead time is visible as the peaks at the right end of the spectra. In black the TDC spectra with the cuts from equation 11.4 and 11.5 to excluded noise and hits that can not have a corresponding trigger in the same cycle. The histogram is scaled 6 times higher to demonstrate the difference.

(chip 141, channel 9)

implemented. The cut on the ADC value of the trigger as shown in Figure 11.5. Only the middle part of the TDC ramp is considered to avoid non linearities and effects at the end of the ramp

Trigger channel:

$$ADC > 500 \quad (11.4)$$

$$1500 < TDC < 3000$$

To avoid the time walk effect only a small range in the ADC of the data channels are considered. Also the same TDC cuts apply as for the trigger channel. Because of the delay time of the trigger electronics (Figure 11.9 on the left) no data is expected after a TDC value of

2500.

Data channel:

$$MPV - 100 < ADC < MPV + 100 \quad (11.5)$$

$$1500 < TDC < 2500$$

574 channels (two already calibrated trigger channels) with 9184 memory-cells (16 each) need

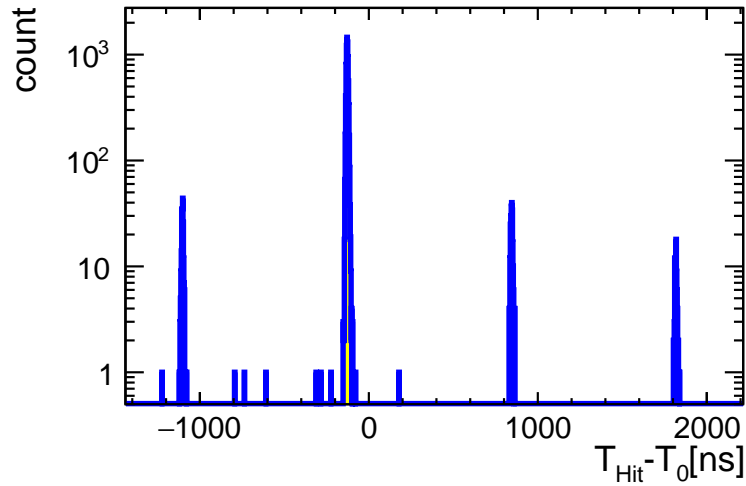


Figure 11.11: Time difference to the trigger for one memory-cell (3) of one channel (141/5). The time difference for one memory-cell with all cuts from equation 11.3 applied is shown in a broad range. Apart from the main peak the revolution frequency of the DESY II test beam of 1 MHz (1 μ s) is visible.

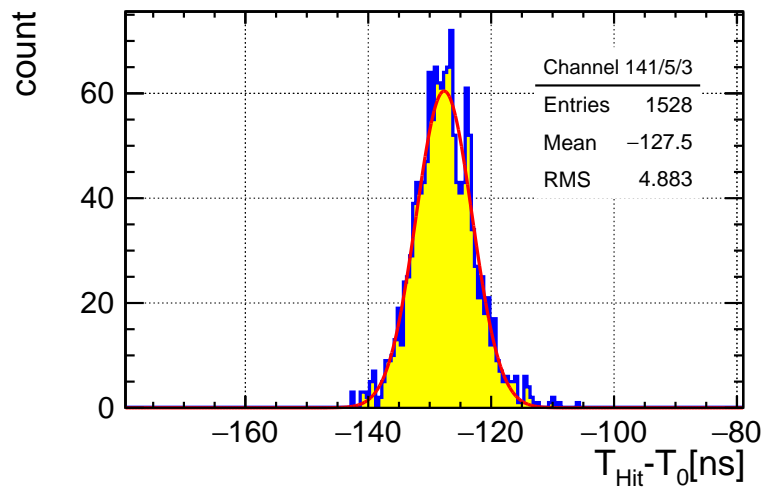


Figure 11.12: Zoom into Figure 11.11 in the range close to the time reference. A Gaussian fit in red underlines the even distribution in time. The mean is written into a database as the memory-cell offset for this specific cell.

an individual calibration offset. The first memory-cell has no ADC information and is ignored,

leaving 8610 constants. Several channels were broken or had to be deactivated during the test beam campaign due to high noise. Remaining high noise channels can prohibit the last memory-cells to be filled with any event. Data for 7994 memory-cells was available. All hit times after ramp correction are plotted per memory-cell (9216 in total) into a histogram and the mean is taken as the memory-cell offset correction. Memory cells with a RMS over 10 ns are regarded as broken and excluded from the analysis. Figure 11.13 shows the memory-cell offset over the TDC range and one broken cell (129/35/5) that is excluded from the analysis. The amount of entries obtained per cell is in Figure 11.14 on the left. Memory cells with less than 100 entries were excluded from calibration to avoid deterioration of the time resolution of the whole detector due to the error on the offset of a few cells. On the right is the distribution of RMS for all memory-cells. Cells with an RMS value over 10 ns are considered to behave non typical and broken. 7519 Memory cells (87 % of all possible cells) passed all criteria and were calibrated.

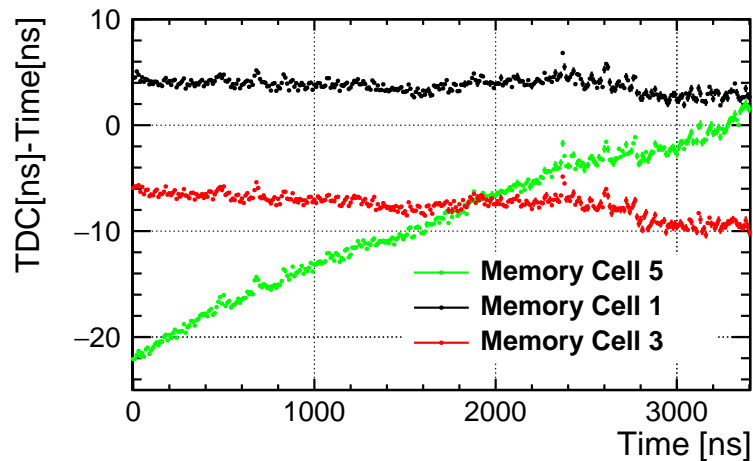


Figure 11.13: Example of a broken memory-cell. This plot is produced with the data of the previous section on one of the electronically calibrated channels (129/35). Memory cell five is clearly broken not showing a constant offset but a slope. If $TDC[ns] - Time[ns]$ is histogrammed it will result in a larger RMS than non broken channels (Cell 1:1.74 ns, cell 3:1.73, cell 5:3.38 ns).

All offsets can be seen in Figure 11.15. The external time reference signal shows a mean offset of 142 ns from the signals of the SiPMs. Differences of 100 ns exist between memory-cells with a RMS of 14.8 ns. Not correcting the memory-cell offset would lead to a resolution worsened by 15 ns.

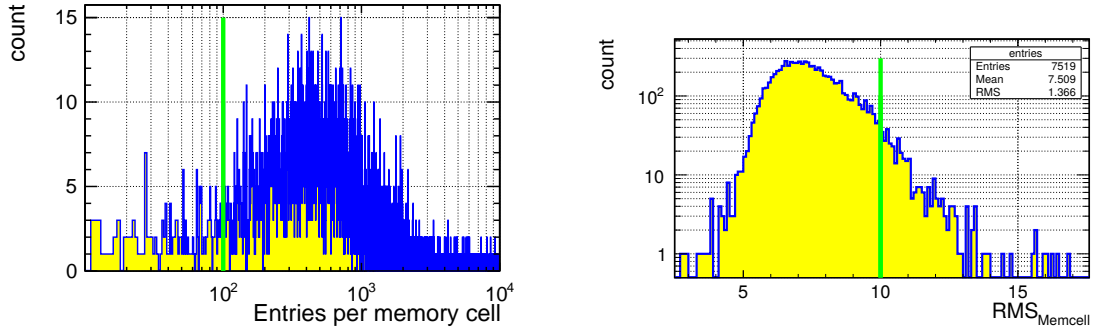


Figure 11.14:

Left: Available entries per memory-cell for calibration. Cells with less than 100 entries are discharged as indicated by the green line.

Right: RMS for each memory-cell. As seen in Figure 11.13, some memory-cells show a non-constant behavior over the TDC range and result in a larger RMS of T_{Hit} . Cells with an RMS over 10 ns are discharged. Green lines indicate the cuts.

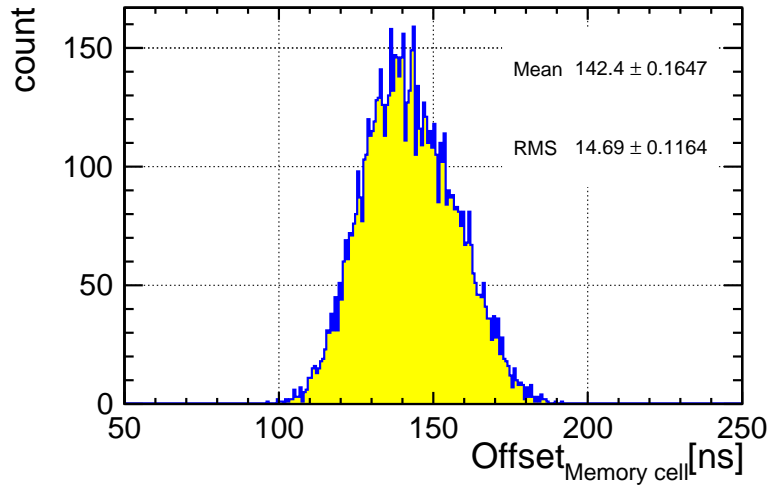


Figure 11.15: Calibration offsets for all memory-cells. The mean of the offset of each memory-cell from the electron test beam data is taken. The mean offset of 142 ns is the trigger delay due to the trigger electronics.

11.2.3 Time slew correction

Signals with the same signal shape but different amplitudes pass a threshold at different times although they originate from the same point in time. This effect shown in Figure 11.16 in the left is called time slew and needs to be corrected for in the Spiroc2b. As can be seen in Figure 11.16, the time of hit in the electron test beam data depends on the pedestal subtracted ADC amplitude. A simple fit function given by

$$Ts(A_{i,j,k}^{ADC} - P_{i,j,k}^{ADC}) = -2.4 + e^{2.78 - 0.00064 \cdot (A_{i,j,k}^{ADC} - P_{i,j,k}^{ADC})} \quad (11.6)$$

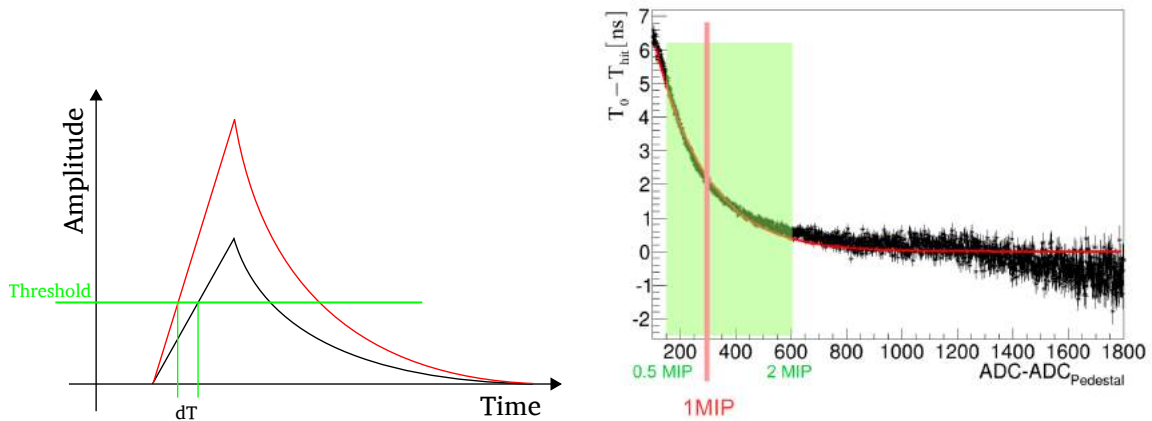


Figure 11.16:

Left: Time slew effect. The same signal with different amplitudes produced at the same time in red and black. The black signal passes a given threshold (green) earlier than the red signal. The time difference $dT(\text{Amplitude})$ is the time slew.

Right: Time slew in the electron test beam data in black. The red line indicates the fit function 11.6 to correct for this effect. Due to low statistics, the effect deviating from the fit function at high amplitudes can not be investigated. The pink line at around 300 ADC ticks is roughly the energy comparing to one MIP. The interesting energy range for the late components in hadronic showers range from 0.5 MIP to ≈ 2 MIP, and the analysis is constrained to those energies, see Figure 3.8 in Chapter 3.1.5

corrects approximately this effect for small energies to 4 MIP. For the purpose of this study of the time distribution of particles in hadronic showers, the late components are of interest. Those physics processes like neutron capture show small energy depositions of around 1 MIP, see Figure 3.8 in Chapter 3.1.5. The MIP value is roughly around 300 ADC bins. High energies show a not understood behavior shifting away from the fit function, but are of no particular interest for the investigation of late components in hadronic showers.

11.2.4 Trigger per chip dependency $P_S^{TDC}(N)$

The pedestal of the time measurement (TDC) is not directly accessible in the Spiroc2b. It is not saved in the memory-cells of non triggered events. As opposed to the $P_{i,j,k}^{ADC}$ pedestal of the energy measurement, the TDC information is a random number on readout of non-triggered channels. $P_S^{TDC}(N)$ is a shift of time measurement caused by the occupancy of the chip in which the hit was measured. The shift depends on the amount of trigger signals in one chip and is independent of the saved amplitude. Figure 11.17 on the left shows the data from three different test beam campaigns. For each hit, the number of trigger signals in a chip is calculated. This data is corrected for the time slew and memory-cell offsets. In blue, the electromagnetic shower data with the aluminum absorber is used to calibrate the memory-cell offset, see section 11.2.2. In red, a dedicated short run with an iron absorber of 5 cm thickness directly in front of the the detector. This test beam investigated the behavior of the chip in dense electromagnetic showers in one chip only. In green, the data from the

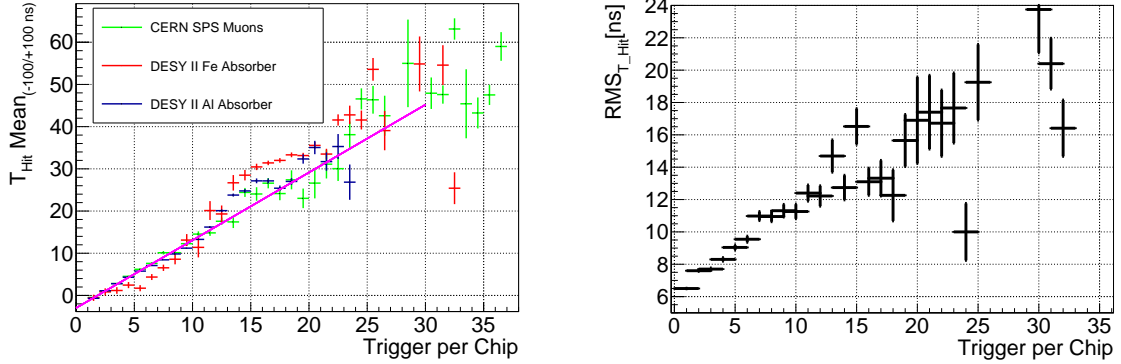


Figure 11.17:

Left: T_{Hit} shifts with the amount of triggered channels per Chip. Data from three different test beams are shown. In blue and red electromagnetic showers produced at the DESY II test beam with aluminum and iron absorber. In green, muon data from the test beam at the CERN SPS described in Chapter 12.3. All three data sets show a similar behavior and are corrected for with equation 11.7 in purple.

Right: The RMS of T_{Hit} worsens with the amount of triggers in the chip. The data shown is from the first test beam only.

test beam at the CERN SPS that is described in Chapter 12.3. In this data set entries exist with a high number of triggers per chip. Those can be caused by the trigger surge described in section 11.2.5 or accounted to delta electron showers as described in section 3.1.3, Figure 3.5. A simple linear function,

$$P_{i,j,k}^{TDC}(N)[ns] = -2.97 + 1.606 \cdot N \quad N = \text{Trigger signal in chip} \quad (11.7)$$

is used to correct for this effect to approximate the behavior of all 16 chips. Figure 11.17 on the right shows the RMS of the collected data per triggers in one chip. The RMS and thus the time resolution worsens with the amount of triggers in one chip. This is a non-correctable effect and impacts especially in the time resolution of dense electromagnetic and hadronic showers and can be seen later in the analysis. To reflect this behavior in simulations the RMS spreads is quantified as

$$RMS_{T_{Hit}}(N)[ns] = 6.4 + 0.51 \cdot N \quad N = \text{Trigger signal in chip} \quad (11.8)$$

.

11.2.5 Trigger surge

As described in section 6.3.4 the trigger of the Spiroc2b is not directly related to the energy measurement with a different shaper. In some events the readout is triggered by events with energies below the threshold or by electronic random effects in the chip. For the further work the amount of triggers in the chip and the actual physics hits in the detector are assumed to

be uncorrelated. This has consequences for the simulation data comparison in Chapter 12. Those hits are easily discarded with an off-line energy cut and will not enter the analysis. Figure 11.18 on the left shows one of those events obtained from the electron test beam at DESY II. Figure 11.18 on the right shows the difference between triggers and actual hits from particles in the detector for a run with a 3 cm iron absorber to produce dense EM showers in part of the detector. In yellow, the triggers per event and in green the amount of triggered hits per event that pass the physics selection. The amount of triggers N in the chip still

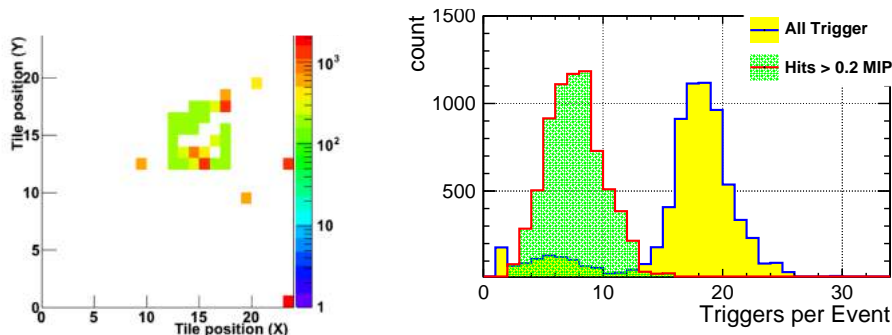


Figure 11.18:

Left: A trigger surge in one chip. The green hits are energy depositions the Spiroc2b trigger on although the signal is lower than the expected trigger threshold. They clearly show part of the outline of the chip 144. The two time reference channels are visible on the right.

Right: In blue/yellow the amount of trigger per event. After proper selection of actual hits over 0.3 MIP threshold, the amount of hits per event decreases to the red/green distribution. Data from a DESY II electron test beam run with a 5 cm iron absorber to produce dense energetic EM showers.

enters $P_{Pedestal}^{TDC}(N)$. The reason for this chip behavior is not clear. The time resolution still worsens according to Figure 11.17.

11.2.6 Summary TDC calibration

Figure 11.19 shows T_{Hit} of all hits in the data taken during the test beam with electromagnetic showers from the aluminum absorber. All corrections are applied and the full energy range is used for triggered hits. A mean number of 9.6 hits per event and 2.7 triggered channels per chip per event worsens the resolution and 6.7 ns could be achieved. For 567 channels, a data base with a blacklist of cells, 8640 memory-cell offsets, two correction functions (time slew and $P_{Pedestal}^{TDC}(N)$), and 76 data points for each ramp correction for 16 chips (1216 points) are needed to achieve the best possible time resolution. A calibration to this extent is unfeasible for a full scale ILD detector. Studies are being conducted with test beam data from 2014 to simplify this calibration without losing time resolution. The 2014 prototype is equipped with technology from Chapter 6 and the new SiPM technology used will result in a better time resolution. Operation of the Spiroc2b is better understood with the detailed knowledge now obtained about the behavior of the chip. A new version of the Spiroc [87] is being developed

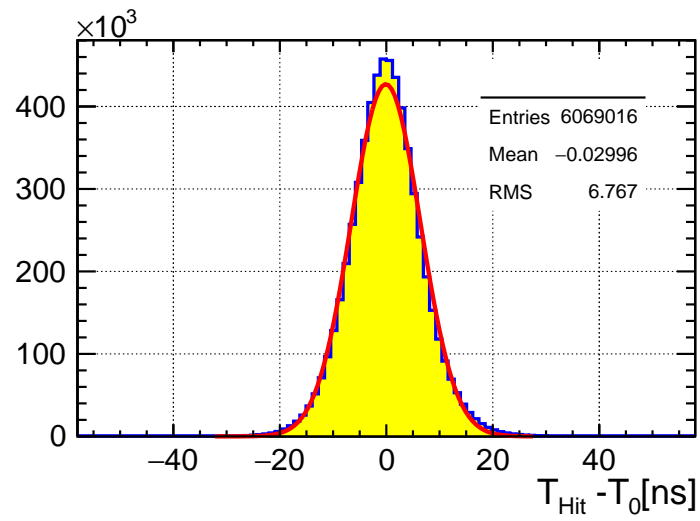


Figure 11.19:

Time resolution on an independent data set from the electron test beam with aluminum absorber. All corrections mentioned in this Chapter are applied. To reduce outliers the data is restricted to ± 100 ns around 0 ns.

with a redesigned time measurement section, improving on the shortcomings of the current version.

Chapter 12

Hit time measurement in a Hadron Test Beam

In November 2012, the one layer AHCAL prototype was placed in a joint test beam campaign at the SPS accelerator at CERN. The AHCAL served as a one layer addition behind the DHCAL prototype and before the tail catcher, see setup in figure 12.1. 120 GB of raw data was taken in 78 runs. LED calibration data and dedicated externally triggered pedestal runs were taken at the beginning and end of the test beam campaign. In the test beam, the calibration from chapter 11 is validated with muons and a first data-taking with pions (π^-) at different energies is carried out. The goal is not only to acquire experience operating the Spiroc2b timing feature, but also to collect data to validate and improve Geant4 simulations. For this, a detailed simulation has been carried out by other members of the collaboration [88] to compare data.

12.1 Setup of the Detector in the SPS Area

The test beam area H8 [89] at CERN was used. Running in secondary beam mode, it can provide electrons and hadrons with up to 200 GeV per particle. The primary 450 GeV proton beam is directed onto targets producing a secondary beam mainly of pions and photons from π^0 decays. The electron contamination is under 1.4% [90]. The spill structure is a 9 s spill every 45 s. The one layer AHCAL prototype has been placed directly behind the DHCAL with tungsten absorber (W-DHCAL) inside a temperature controlled cooling tent.

12.1.1 The W-DHCAL main detector

The DHCAL is a CALICE prototype sampling calorimeter optimized for very high spacial resolution. The principle behind the DHCAL is to establish a proportionality between the energy of a particle and the number of hits the shower generates in the sensitive medium.



Figure 12.1: W-DHCAL in tungsten stack with the tail catcher during installation of the AHCAL layer at the H8 SPS beam line at CERN.

Therefore, the energy information per cell is disregarded and only the passing of a threshold is saved. The DHCAL prototype used in this test beam consisted of 39 layers instrumented with resistive plate chambers (RPC, see [91]) interleaved with tungsten absorber plates of 1 cm thickness. The 3 RPC layers have 48 chips with 64 channels of $1 \times 1 \text{ cm}^2$ each. This sums up to 497664 individual channels. Distance between the plates for the active cassettes is 15 mm. Each cassette consists in term of material of 2 mm copper and 2 mm steel. This sums up to $3.3 X_0$ and $0.14 \lambda_i$. A tail catcher consisting of RPC interleaved with steel layers was located behind the calorimeter. Details about the machine and analysis of the test beam data can be found at [92] and the CALICE note CAN-039.

12.1.2 One layer setup and data taking

In the following, the setup for the one layer prototype is addressed and operating conditions are investigated.

Beam Trigger Setup

The trigger logic used is the same as described in section 11.2.2 and is fed into channel 35 of chip 137 and 129. Two different sets of scintillators were available. For the narrow pion beam, two $10 \times 10 \text{ cm}^2$ scintillators were placed directly in front of the DHCAL, while for

the muon calibration, two $30 \times 30 \text{ cm}^2$ scintillators read out with PMTs were used at both ends of the setup. This caused an arbitrary offset on the data. For each scintillator pair, the position of the main peak of the hit times were defined as 0 ns.

Temperature variations during Test Beam

Despite the temperature controlled tent the variations in operating temperature range over $\approx 3^\circ\text{C}$, as can be seen in figure 12.2, where the temperature variations over the whole data taking period is shown.

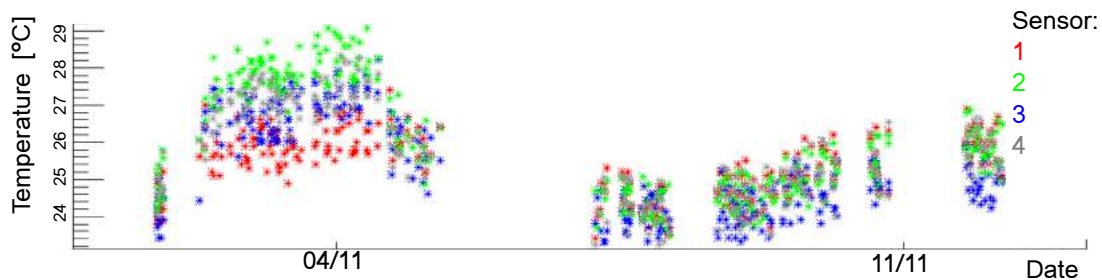


Figure 12.2: Temperature variations over the test beam period. 4 sensors on different positions on the one layer prototype were read out every 1000 readout cycles of the detector. The sensor offset has been calibrated to a precision of 2° while the variations have a 0.1° precision.

Beam Rate during Data Taking

During the running with the DHCAL a low beam rate had to be maintained. Due to the Spiroc2b design for the ILC beam structure, the data taking was very inefficient. The readout of the chip cannot be synchronized with the beam structure and can take up to $600 \mu\text{s}$ with USB 1.0 connection, missing several bunches. The bunch train counter flips every 4096 events. To avoid wrongly assigned events, a readout would have been dictated by the detector. The optimal period for a readout would have been 15 ms to avoid wrongly assigned events, but 60 ms were chosen as a time out for the readout as a compromise, minimizing the possibility of wrongly assigned events to 10^{-6} and avoiding signal degradation from long storage time in the memory cells as described in [86]. Of the taken data, 16% had to be discarded because of missing ADC information. Due to an error in the Spiroc2b, the first memory cell read out always returns a value of $ADC = 0$. Of the remaining data, 0.1% showed an unrelated TDC zero value. The $TDC = 0$ readout is not related to the $ADC = 0$ bug and could not be explained yet. 7% of the channels had to be disabled: despite the external validate trigger (see section 6.3.2), the noise of those channels overwhelmed the beam rate of the SPS. Muon run collected a total of 270000 triggered μ^- events. After data selection, 99754 usable events were left. The synchronous running at low rate (0.5 Hz- 20 Hz) for pions with the DHCAL yielded in a low data efficiency rate. Following the DHCAL pion run plan limited

the amount of usable data for most energy points except the high statistic runs at 50 GeV which collected 207000 events, of which 14313 were left after event selection. A dedicated high rate run at 180 GeV (1200 Hz) produced 430000 events from which 80674 usable events could be extracted.

12.2 Geant4 Simulations of the Test Beam

The complete detector has been simulated for 50 GeV and 180 GeV pion (π^-) and 180 GeV muon μ^- events [88]. The experimental setup has been simulated using GEANT4 and the CALICE Mokka framework [93]. The simulated detector was composed of a 39 layer structure (38 layers for the DHCAL, plus one additional AHCAL layer), 1 m wide and 1 m high, each layer formed by tungsten absorber and sensitive material. The exact gas mixture filling the RPCs has not been simulated, and the corresponding sensitive layers have been replaced with air for simplicity. Plastic scintillator was used as sensitive material for the final AHCAL layer. The TMCT following the AHCAL has not been simulated. It is expected that this simplification underestimates the back scattered neutrons (Albedo) and thus late components of hadron showers. Late components in the shower are mostly caused by late neutron evaporation, see chapter 3.1.5. Tungsten as absorber material provides a rich time structure by producing more slow neutrons than the iron absorber. The difference between simulation packages from Geant4 become more apparent for this absorber. In Geant4, physics simulations are driven by look up tables for processes and different simulation packages in different energy regimes, see figure 12.3 above. Most packages split the simulation process and cross section table use depending on the energy of the simulated process. Explanation of the different physics lists can be found in [94]. The QGSP_BERT package has been proven to be the most successful package in describing the shower behavior, as seen in [81]. The QGSP_BERT and QGSP_BERT_HP package differ in the treatment of neutrons in material. Figure 12.3 below shows the difference between the two packages in simulations for the time of hit in the simulated calorimeter compared to the QBBC list and data from the T3B experiment [31]. This work focuses on the differences between QGSP_BERT and QGSP_BERT_HP that uses a high precision model for thermal neutron capture below 20 MeV. In order to simulate the triggering behavior of the Spiroc2b, a sliding window technique was applied. First, the hits in a cell are ordered in time. The energy is summed up in a sliding window of 15 ns, imitating the fast shaper in the Spiroc2b. Once trigger threshold is passed within that sliding window, the chip is triggered and a 150 ns window is integrated. This simulated the slow shaper used for the energy signal production in the Spiroc2b. A schematic description of the algorithm can be seen in figure 12.4. The sub-hits $tag_{1...4}$ are ordered in time. tag_1 does not yet pass the threshold but the sum of $tag_1 + tag_2$ occurring within a 15 ns window passes the threshold. tag_2 is the time of hit saved. E_{sum} in blue in figure 12.4 is the 150 ns sliding window that

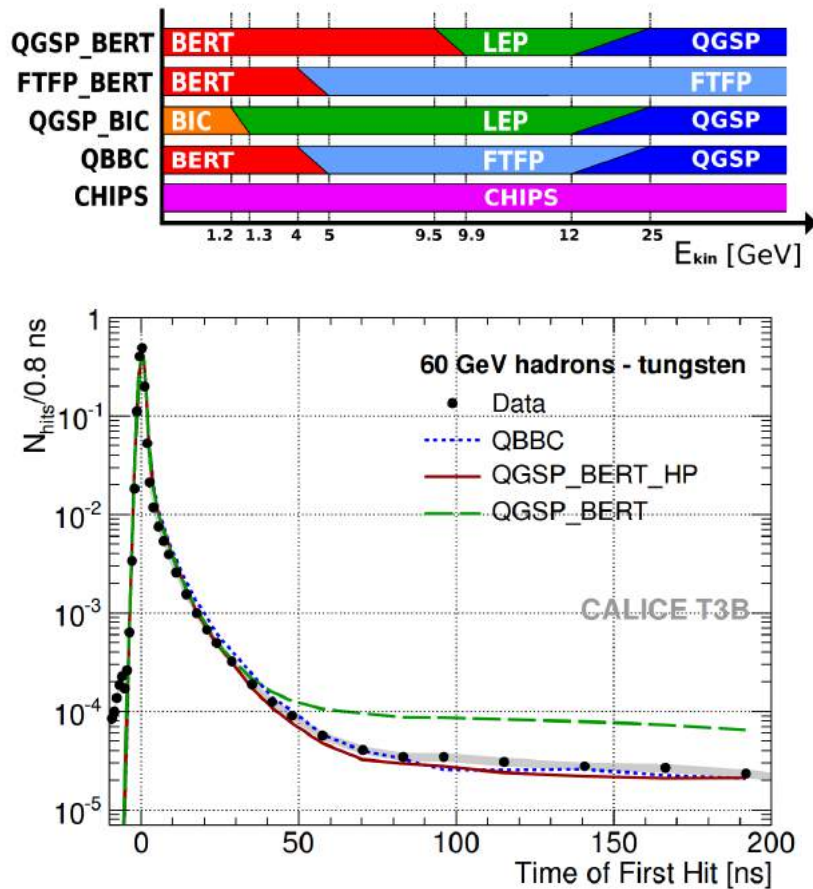


Figure 12.3:

Above: Schematic representation of different physics lists used by the Geant4 simulation package. The choice of physics lists depends on the energy of the process, in the overlap regions a list is chosen randomly [94].

Below: Comparison of the time of first hit in the T3B experiment and in the according simulations with different physics lists as shown in [81].

is saved, including consequent sub-hits tag_3 and tag_4 . Disabled channels in the detector are also disabled in the simulations. Figure 12.17 shows the detector with all disabled channels, summing up to 7% of all channels. The channels are either excluded from the analysis because of the faulty behavior during calibration in the DESY II test beam (see chapter 11.2.2), or disabled during data taking because their high noise would overwhelm the beam rate at the SPS. The simulation is convoluted with the time resolution according to the amount of triggered channels in the real data to compare simulations to data. Figure 11.17 on the right in chapter 11.2.4 shows the resolution according to the number of triggered channels used to distort the simulations. The noise can be estimated by taking the number of hits in a specific time interval before the main trigger arrives. This has been used as a constant offset c for the simulation and was determined for each data set.

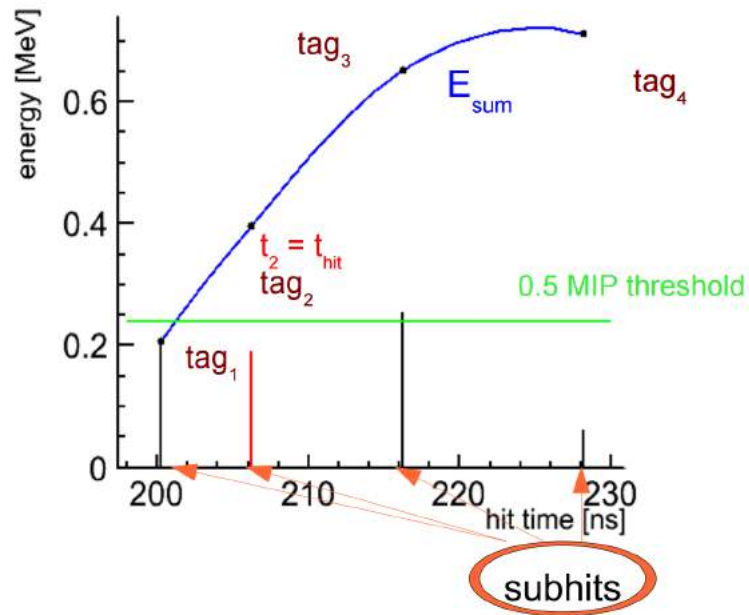


Figure 12.4: Determination of the time of hit for simulations. In the Spiroc2b the SiPM signal is fed through a 15 ns shaper to a threshold discriminator. The time of hit is saved once the threshold is overstepped. The actual energy signal is integrated through a 150 ns shaper. In the simulation hit energies are added within a sliding 15 ns window. The time stamp of the hit is saved when the summed up energy reaches the threshold. The energy information is summed over 150 ns starting with $T_{Hit} - 15$ ns. [95]

12.2.1 Energy calibration

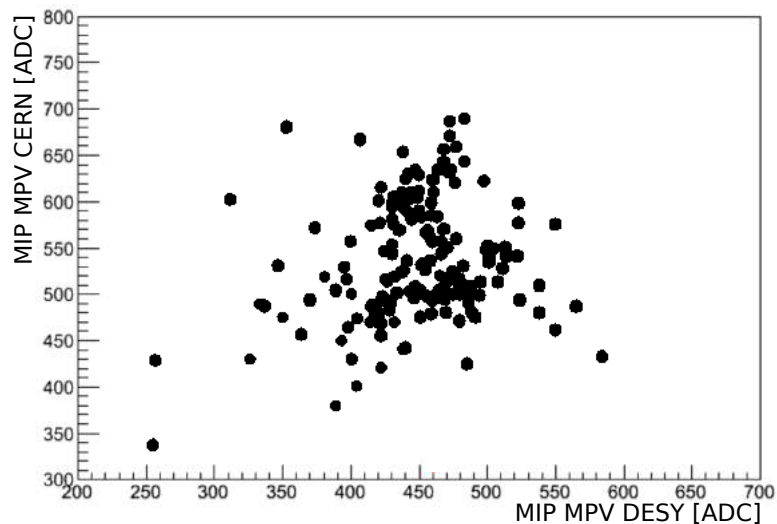


Figure 12.5: MPV found for the MIP calibration in the SPS versus the calibration at the DESY II test beam. The eight chips with sufficient entries are shown channel-wise. The difference can be explained due to the temperature difference and mismatching voltages, see chapter 8

A total of 99700 usable muon events unevenly distributed over all channels do not provide

enough entries for a complete energy calibration. A MIP calibration was carried out at the DESY II test beam facility prior to the SPS test beam. The temperature at the DESY II test beam was around 30°C while the SPS operational temperature was around 25°C with variations of 3°C , see figure 12.2. Due to the wide range of operating voltages (table 11.1) and the sensitivity of the CPTA SiPMs of over $50 \frac{\text{mV}}{\text{GeV}}$ a precise ADC calibration proved difficult. The temperature dependency of the MPV is not linear and the DESY II test beam data cannot be used to transfer the calibration to the SPS test beam since the tile SiPM system has not been characterized for temperature changes. Figure 12.5 shows the comparison of the calibration point for a MIP of all channels separated by chips. A precise energy calibration is not necessary for the primary goal of this timing analysis so a chip-wise rough energy calibration has been applied. For each chip all triggered hits from all channels are collected in one histogram. Figure 12.6 shows the resulting histograms for the six chips with the most

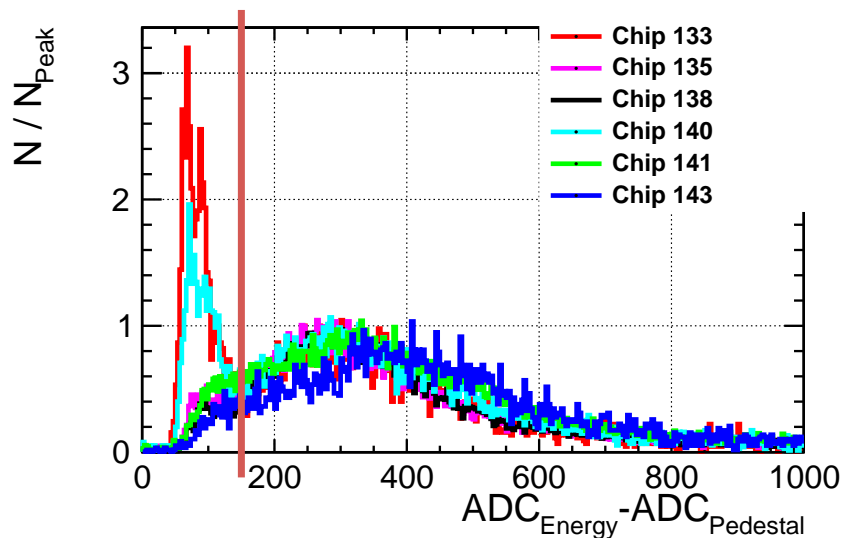


Figure 12.6: MIP calibration and off-line threshold calibration. Data from muon runs at the SPS. 6 ASICs out of the 16 with the most entries are shown for this calibration the pedestal subtracted energy hits from all channels are collected for each chips. The light red line indicates the common threshold applied for the 0.5 MIP cut.

Amount of entries for the different chips 133:737 135:20331 138:24246 140:9676 141:24083 143:6153

entries. For comparison, they have been rescaled to the MIP MPV.

Chips with noisy channels show a peak in the amplitude range close to the threshold cut (see for example chip 133 in red), due to non completely suppressed noise contribution.

The second peak is the MPV of the energy deposition of muons. The MIP position for all chips was assumed to be around 300 ADC and the 0.5 MIP threshold was set to be 150 ADC for all channels in the detector. The impact of a wrong threshold setting for the analysis of the time of hits is shown in figure 12.7 on simulations. To estimate the impact on the analysis if the off line threshold is not correctly set at 0.5 MIP the threshold of every single channel in

the simulation has been varied randomly by 10 %, 20 %, and 50 %. No impact on the result could be seen and the rough energy calibration is justified for this analysis.

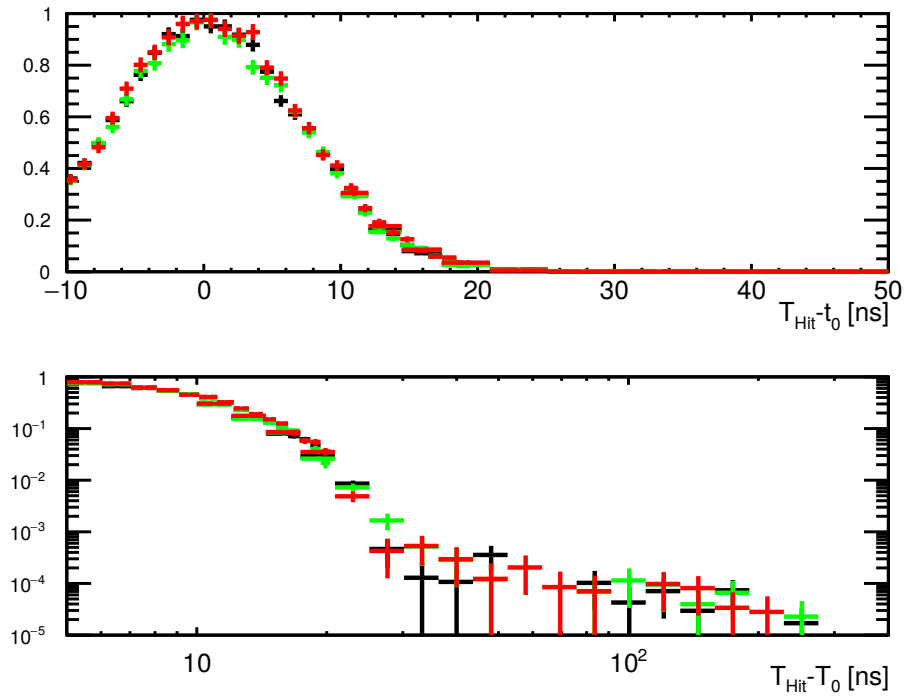


Figure 12.7: 180 GeV π^- have been simulated with the described setup. The threshold on the individual channels have been varied randomly by 10 % (red), 20 % (green), and 50 % (black).

12.3 Validation of Timing Calibration with Muons

With the muon beam the timing calibration described in chapter 11 could be validated. The muon beam at the SPS shows contamination with multiple muon events. Due to the trigger configuration of the experimental setup it was not possible to exclude those events in the data. Therefore an off-line cut had to be applied, requesting that only one channel at the time would be triggered. Figure 12.8 shows the achieved resolution with muon events. $30 \times 30 \text{ cm}^2$ scintillators were used for the muon data. Muons hitting the scintillator away from the readout PMT travel a substantial amount of time towards the PMT. This delays the trigger signal with respect to the real time of hit of a muon. $T_{hit} - T_0$ gets shifted to earlier hit times for delayed trigger signals and the resolution plot, figure 12.8, deviated from a Gaussian distribution in red. Using the RMS as the resolution, a time resolution of 6 ns

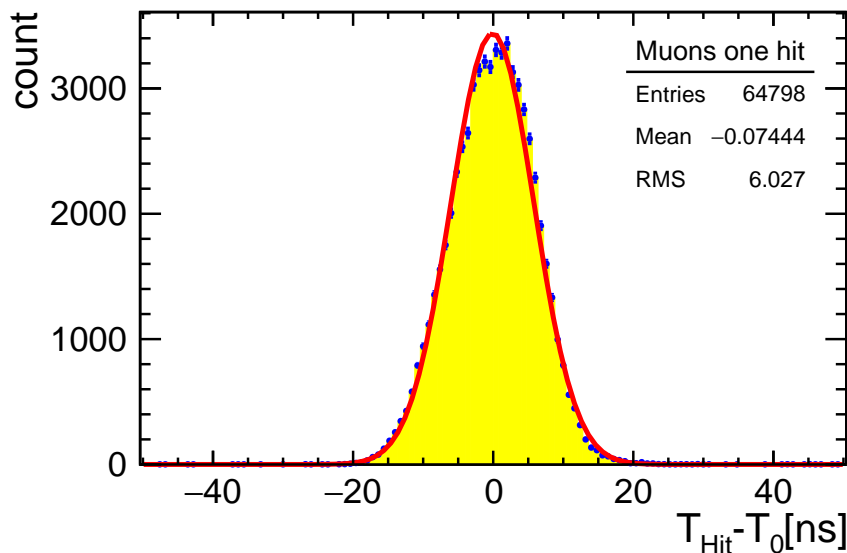


Figure 12.8: Time Resolution with muons. Hits with only one hit in the event has been selected to exclude $P_S^{TDC}(N)$ and particle contamination as well as sub showers. A resolution of 6 ns could be achieved. The impact of the big scintillators can be seen by a distortion of the distribution from a Gaussian shape to earlier hits. $T_{hit} - T_0$ gets shifted to earlier hit times for delayed T_0 .

could be achieved. A constant noise fraction for the muon data of 10^{-3} per event has been found.

12.3.1 Validation of $P_S^{TDC}(N)$

To evaluate the calibration with muons the data has to be compared to simulations and the trigger per chips effect $P_S^{TDC}(N)$, chapter 11.2.4 has to be taken into account. A simulation has been carried out for 180 GeV muons with the QGSP_BERT_HP package. The calibration with the electron test beam has been carried out with small $2 \times 2 \text{ cm}^2$ triggers. The deviation

from the Gaussian shape for instantaneous hits in the muon beam caused by the $30 \times 30 \text{ cm}^2$ triggers is taken into account for the simulations. The histogram in figure 12.8 for one hit and one trigger per chip only is used for a data driven distortion of the simulations. To take into account the worsening of the time resolution with an increasing number of triggers, equation 11.8 reduces to

$$RMS_{T_{Hit}}(n) = 0.51 \cdot n \text{ ns} \quad n = \text{Trigger signal in chip}, \quad (12.1)$$

since the initial spread is now included already by the data driven distortion. For every hit in simulations a random number distributed according to figure 12.9 is produced. The number has to exceed or equal the amount of hits in the simulations. T_{Hit} is smeared with a Gaussian distribution with a sigma according to equation 12.1. Due to the low occurrence of high occupancy in figure 12.9 the effect of the trigger surge (see chapter 11.2.5) becomes visible. The behavior during those trigger surges is not clearly understood and hits with more than 25 triggers per chip are excluded. Figure 12.10 and 12.11 show the comparison

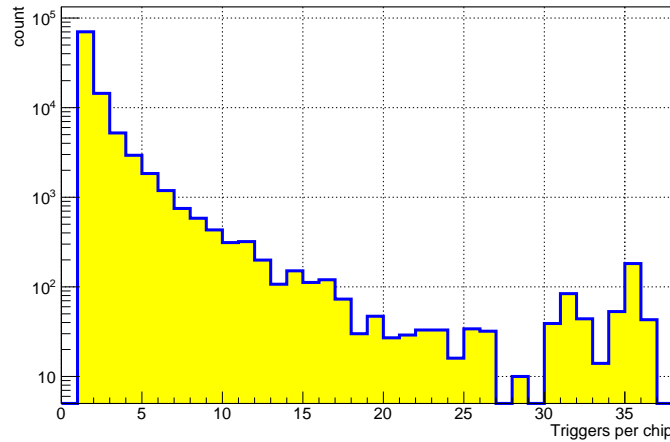


Figure 12.9: Triggers per chip occurrence in the 180 GeV muon data. This histogram is used for data distortion in simulations. Higher occupancy is pointing to trigger surges, see chapter 11.2.5.

of the distorted simulation with the QGSP_BERT_HP simulation package. In total 100,000 muon events have been simulated. Due to the rare occurrence of late hits as mentioned in chapter 3.1.3, the limited statistic in late bins produces large uncertainties. Within those uncertainties the simulations agree with the data, see figure 12.11 for a detailed comparison. The calibration and quantization of effects from chapter 11 has been therefore validated with 180 GeV muon data at the SPS test beam.

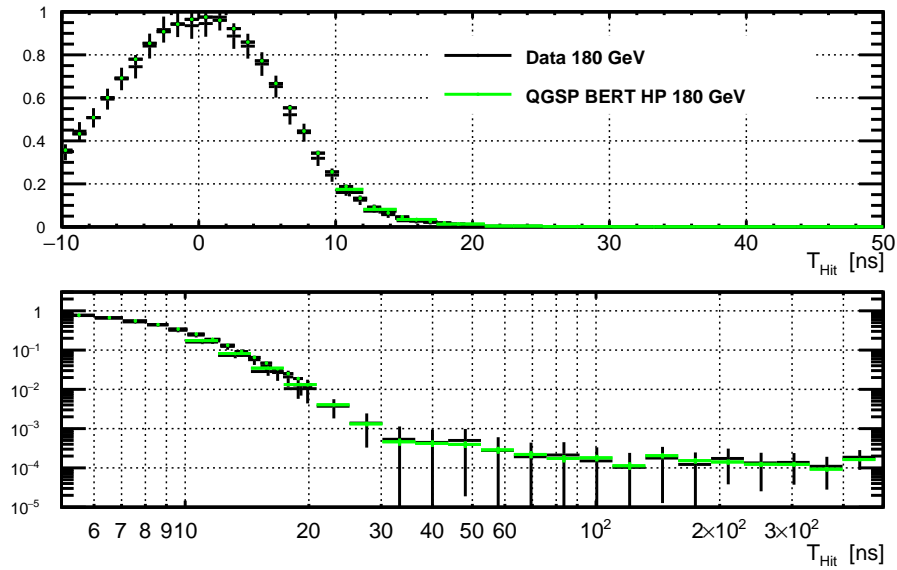


Figure 12.10: The time of the first hit over threshold T_{FHOT} in comparison with simulations for 180 GeV μ^- . In black the dataset from the SPS test beam. In green, the QGSP_BERT_HP package distorted with data. The same data is shown above for -10 ns to 50 ns and below in double logarithmic scale for 0 ns to 500 ns.

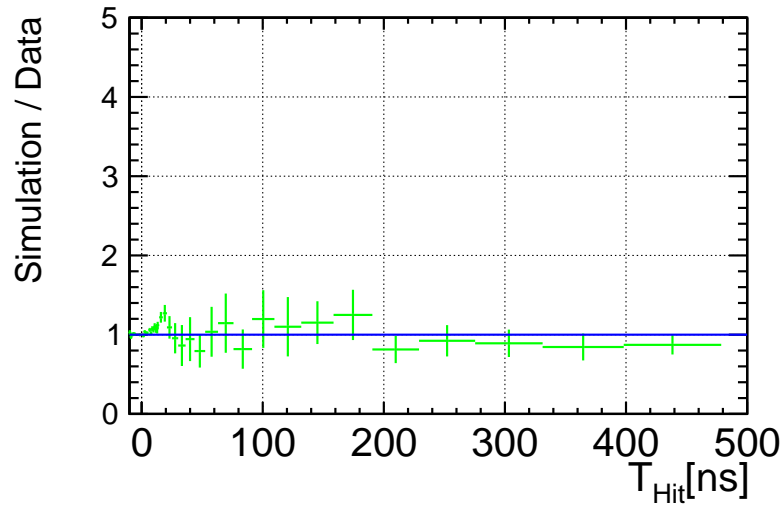


Figure 12.11: Ratio of the data to simulations, green for QGSP_BERT) for 180 GeV muons.

12.4 Response to Pions

Data from pions at 50 GeV and 180 GeV were taken with the AHCAL synchronous with the DHCAL. Several runs in 50 GeV and 180 GeV pions have been taken. There has been one 10 hour long AHCAL dedicated data acquisition for 180 GeV pions with high rate. For the pion runs, two $10 \times 10 \text{ cm}^2$ scintillator triggers were placed in front of the DHCAL detector. The different timing behavior of this trigger compared to the $30 \times 30 \text{ cm}^2$ triggers used for

the muons changes the spread of the distributions of T_{Hit} . A data driven approach with the muon timing data to simulate the behavior of the detector in pion data is therefore not possible. The data is corrected for all known effects discussed in chapter 11.2.4 with the values obtained from the electron beam. The simulations are convoluted with Gaussian distributions according to the values from figure 11.17 on the right. The RMS value is taken as the σ of a Gaussian distribution smearing out the data. The amount of triggers per chip and the amount of hits that pass the threshold per chip is not sharply correlated. To reflect this in the smearing of the simulations, the distribution of triggers per chip of all data runs for 180 GeV and 50 GeV are used respectively. Figure 12.12 shows the distributions applied. The noise in simulations are determined by taking the amount of triggers per bin 30 ns before T_{Hit} in data.

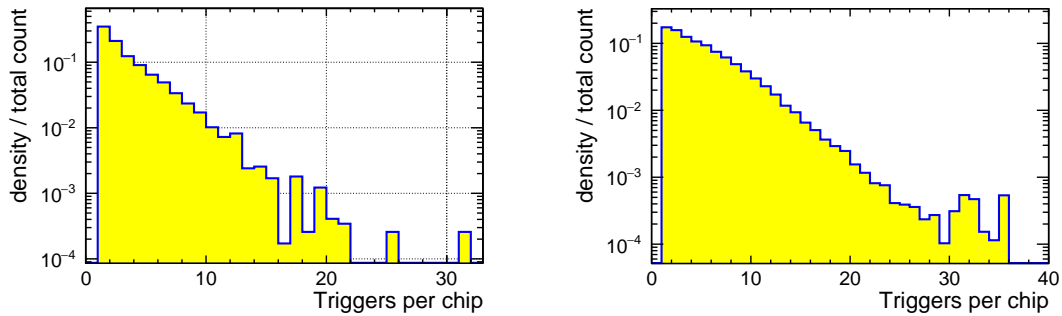


Figure 12.12: Trigger per chip histogram used for data distortion in simulations.

Left: Triggers per chip in the test beam run data for the 50 GeV pions.

Right: 180 GeV pions

12.4.1 180 GeV pions

Figure 12.13 shows the comparison of data and simulations for the 180 GeV pions. The histograms describe the distribution of hit time within a pion shower. Hit times have been renormalized to the time of the first hit of each shower: since the majority of hits are highly relativistic secondaries or EM sub-showers, the MPV of this distribution is 0 ns. The comparison with two Geant4 physics lists is shown, QGSP_BERT_HP and QGSP_BERT. The early components and processes up to ≈ 50 ns are well described by both physics lists and match the data. The difference is seen by the treatment of late neutron components from the HP package. Neutrons in the QGSP_BERT list deposit their energy earlier than in QGSP_BERT_HP which produces more late hits. Figure 12.14 shows the ratio of simulations to the data. The QGSP_BERT_HP list is clearly favored by the data. Both packages overestimated the components around 100 ns although the difference can be explained by the not clearly understood effect of $P_S^{TDC}(N)$ (chapter 11.2.4) that shows a small dependency on the ADC load on the chips.

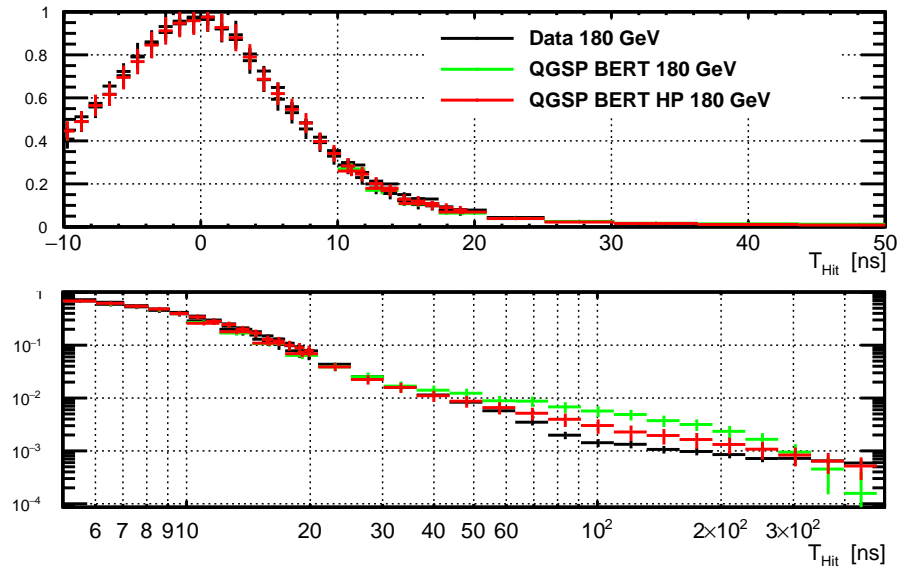


Figure 12.13: The time of T_{FHOT} in comparison with simulations for 180 GeV π^- . In black the dataset from the SPS test beam. In green, the QGSP_BERT package simulations and in red, the QGSP_BERT_HP package with high precision neutron treatment. The same data is shown above for -10 ns to 50 ns and below in double logarithmic scale for 0 ns to 500 ns.

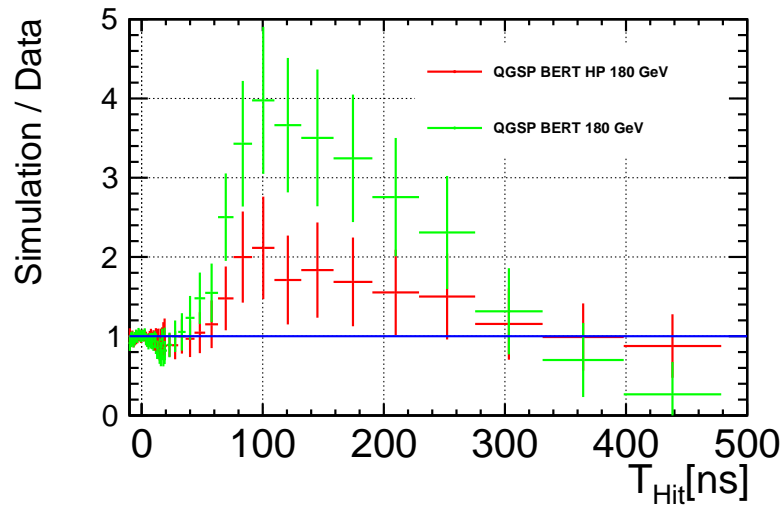


Figure 12.14: Ratio of the data to simulations (red QGSP_BERT_HP, green QGSP_BERT) for 180 GeV pions.

12.4.2 50 GeV pions

50 GeV pions runs have only been taken together with the DHCAL. Less usable data was collected with higher noise to data ratio. The same amount of events were simulated for 50 GeV and 180 GeV but less events deposit energy in the last layer resulting in less statistic. The focus on the analysis is on the 180 GeV data. Figure 12.15 and 12.16 show the simulation and

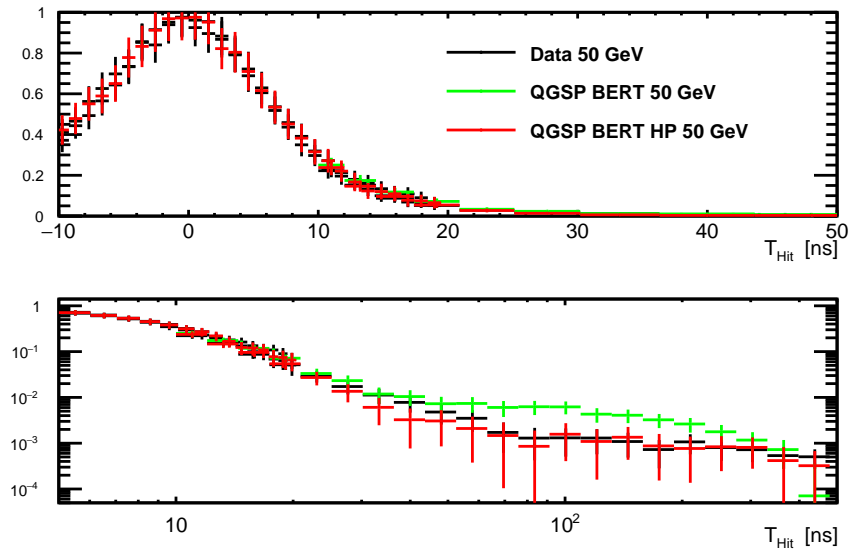


Figure 12.15: The time of T_{FHOT} in comparison with simulations for 50 GeV π^- . In black the dataset from the SPS test beam. In red the QGSP_BERT package simulations and in red, the QGSP_BERT_HP package with high precision neutron treatment.

data comparison like in the previous section. The shower start of 50 GeV pions happens more towards the front layers of the calorimeter with respect to the 180 GeV ones, and therefore less relativistic secondaries could reach the AHCAL placed in the back. The importance of the precise description of slow neutrons that can travel great distances in the detector before interaction becomes more evident in the last layer. The differences between QGSP_BERT_HP and QGSP_BERT are more pronounced for 50 GeV pions. The QGSP_BERT_HP list is clearly favored again by the data and is describing the data well within the errors while QGSP_BERT is overestimating the early components by a large margin.

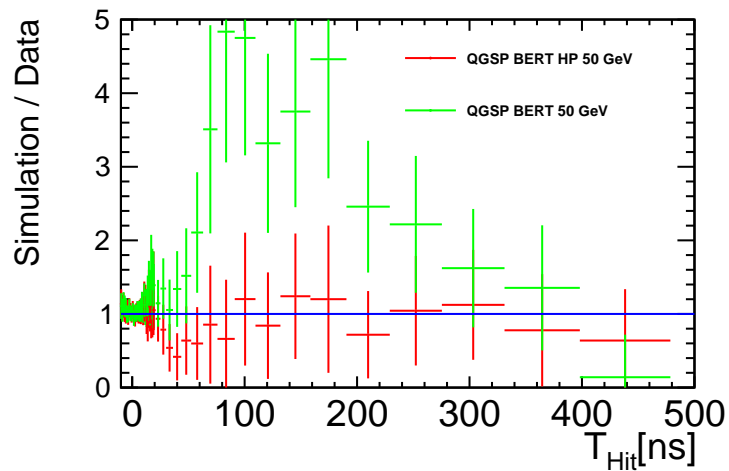


Figure 12.16: Ratio of the data to simulations (red QGSP_BERT_HP, green QGSP_BERT) for 50 GeV pions.

12.4.3 Radial Hit Time Dependency

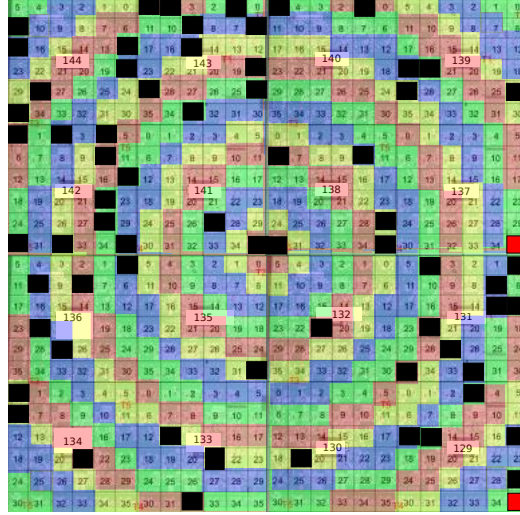


Figure 12.17: Complete map of the one layer prototype. In black, disabled channels due to noise or unclear behavior of memory cells. In red the two trigger channels (35 on chip 129 and 137). The colored rings indicate the bin used for simulation and data in figure 12.18

The topological distribution of T_{Hit} is investigated in this section. Figure 12.17 shows the mapping of the detector and the dead channels also used in simulations. The circles show the radial bins used. The pion beam in simulations has been randomly distributed over the center with a Gaussian function with $\sigma = 13$ mm. Figure 12.18 on the left (50 GeV) and right (180 GeV) show the comparison of the two physics lists with data. To determine the mean, a window of -10 ns to 600 ns for each radial bin is used. At 50 GeV in figure 12.18 on the left, a

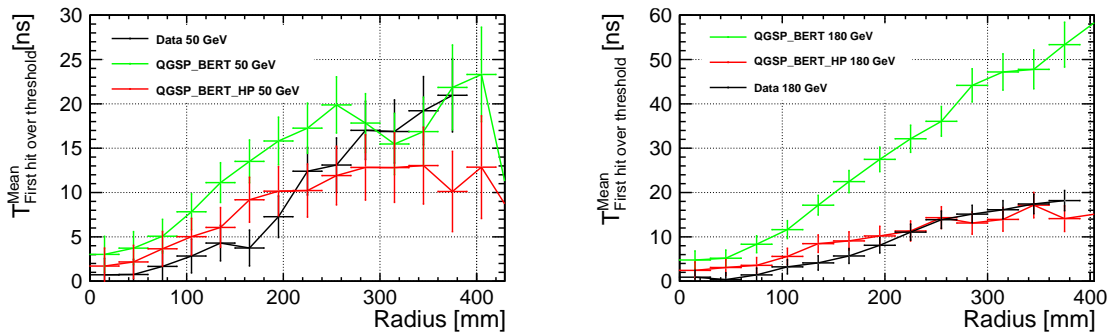


Figure 12.18: Radius dependency for the time of hit of the first hit over threshold T_{FHOT} .

Left: Data and Simulation comparison for 50 GeV pions.

Right: Data and Simulation comparison for 180 GeV pions

the radius for each bin is according to figure 12.17. $-10 \text{ ns} < T_{Hit} < 500 \text{ ns}$ have been considered at the mean calculated.

conclusion cannot be drawn due to the low statistics of the data in the outer radius bin (100

- 10 events over 200 mm). For 180 GeV, as seen in figure 12.18 on the right the difference between QGSP_BERT and QGSP_BERT_HP becomes larger with increasing radius and the data clearly favors QGSP_BERT_HP.

Chapter 13

Conclusion

This work concerns the commissioning and calibration of an analogue hadronic calorimeter based on the concept of particle flow detection. This requires excellent spatial resolution to separate single particles in a jet from their energy deposition in the calorimeter. Such resolution is obtained by segmenting the active layers of a sampling calorimeters in single sensing units with a volume of $3 \times 3 \times 0.3 \text{ cm}^3$. Additionally, this novel prototype includes unprecedented time resolution on the single hit level. The first part of this thesis presents the optimization of the single calorimeter cell. The plastic scintillator tile, its coating with various materials and the coupling to the photo-detector (SiPM) is studied. This leads to an optimized design for the calorimeter cell as discussed in sections 7.2 and 7.3. The Scintillating tile is wrapped with 3M ESR foil. A Ketek PM1125 SMD SiPM is coupled with an adapter to the side of the tile. With this design 1200 calorimeter cells have been produced and characterized through this work. The main figure of merit for the single cell characterization is the amount of light detected for a single MIP traversing the plastic scintillator perpendicular to its larger side (tile response measurement, section 7.1.2). To perform this calibration, a mass testing setup, utilizing ^{90}Sr as MIP like source and UV/blue LED light to obtain the single photon response of the SiPM, has been developed. The calibration of 1200 cells was performed and the response was investigated as function of temperature and voltage. The optimal working point of the single cells in the AHCAL detector is constricted by the requirements of the Spiroc2b readout ASIC with respect to minimum signal strength of the SiPM. The optimization has been done single cell wise with different operating modes of the chip in mind. In Chapter 10, a spread of 8 % on the response was found when operating the SiPM at the optimal working point. As outlook of the single cell characterization studies possible improvements for future measurements have been identified:

- A higher energetic source with an narrower energy spectrum than the ^{90}Sr would provide signals closer to the MIP range with easier external trigger setup.
- The noise over threshold measurement could have also been conducted with greater

precision with the usage of a programmable threshold discriminator and digital counter instead of statistic approximation.

- Despite the good homogeneity of the tile with this SiPM option, the future generations of the detector will have SMD components mounted directly on the HBU during assembly of the board.
- The Eljen scintillator will likely be replaced with one of less response and unit costs.
- The optimization of the working point to achieve minimum response spread requires individual tuning of the SiPM voltage. This operation is performed by an adjustable voltage regulator inside the SiPM readout chip (Spiroc2b). The restrictions on the operating mode are mainly imposed by the Spiroc2b readout chip, especially the uncertainty on the set voltage when using the internal voltage setting.

In Chapter 8 the precision of the voltage setting in the Spiroc2b chip is extensively discussed. The achieved precision ranges from 15 mV to 37 mV, depending on the setting of the internal voltage adjustment register. An alternative to single channel adjustment is to apply an overall common voltage to the SiPM, thereby bypassing the internal chip adjustment. Future generations of the readout chip will provide better voltage precision and stability. The continued development in SiPM production and the consequent high homogeneity of the SiPMs produced will make individual SiPM voltage adjustment unnecessary. After the single cell characterization, four calorimeter layers were assembled and commissioned at the DESY-II electron test beam. The results of the response calibration with MIP like particles of the single cells obtained in the laboratory setup were compared to those from test beam and they resulted in good agreement (with a correlation of 4 %, as discussed in Chapter 9).

The second part of this thesis, starting with Chapter 11, focuses on the time resolution capabilities of the Spiroc2b readout chip to measure the hit time of a signal. The novel calibration procedure was developed using instantaneously generated electron showers as time reference through the calorimeter cells, and taking into account all known features of the readout chip. The obtained procedure is presented (see equation 11.1) and has been validated for the first time with the data collected in this thesis. A time resolution of 6.7 ns could be achieved, which is slightly worse than the 1 ns - 2 ns resolution expected from the chip design. Due to the scintillating fiber in the tiles the photon distribution is smeared in time as well as remaining uncertainties in the chip features worsen the resolution.

Finally, the calibrated prototype calorimeter was exposed to hadronic showers of 50 GeV and 180 GeV pions at the CERN SPS test beam. The results provide insights in to the time structure of hadronic showers and are compared to Geant4 simulations with different physics list. Additionally, muon data has been collected to validate the energy and time calibration procedure developed with electron data. The time calibration with muons agrees

well with the prediction of the simulations including rare production of late showers due to delta electrons. A time resolution of 6 ns is achieved. Pion showers have been analyzed after energy and time calibration. The time resolution and energy measurement precision are high enough to discriminate between the QGSP_BERT and the QGSP_BERT_HP physics lists that have been used to conduct the simulations (see also Chapter 12.2). The QGSP_BERT_HP package is favored by the data with 180 GeV pions, see Figure 12.14. With 50 GeV pions the prompt part of the shower is stopped earlier in the detector and proportionally more late events produced by slow neutrons occur, see Figure 12.10. This data clearly favors the QGSP_BERT_HP package. The limitations of the detector due to many disabled noisy channels, have a large impact on the investigation of the radial dependency of the shower. In the 50 GeV pions measurement the comparison is not conclusive due to low statistics. For 180 GeV pions the showers show a wider extend, see Figure 12.18. Here the data clearly favors the QGSP_BERT_HP model. Qualitatively, the data are in agreement with the results obtained with a dedicated experiment to measure the time structure of hadronic showers, the T3b experiment [31], which had only a one dimensional coverage of the radial shower extension. Currently, a full 1m³ AHCAL prototype with high time and spatial resolution is being commissioned which will allow full 3D coverage of the hadronic showers. It will extend the work presented in this thesis and provide valuable insight into the topological time structure of hadronic showers for comparison and improvement of simulation models.

Bibliography

- [1] A. Salam, “Elementary particles,” *Contemporary Physics*, vol. 1, no. 5, pp. 337–354, 1960.
- [2] S. L. Glashow, “Partial Symmetries of Weak Interactions,” *Nucl. Phys.*, vol. 22, pp. 579–588, 1961.
- [3] S. Weinberg, “A model of leptons,” *Phys. Rev. Lett.*, vol. 19, pp. 1264–1266, Nov 1967.
- [4] G. Bertone and D. Hooper, “A History of Dark Matter,” *Submitted to: Rev. Mod. Phys.*, 2016.
- [5] F. Zwicky, “Die Rotverschiebung von extragalaktischen Nebeln,” *Helv. Phys. Acta*, vol. 6, pp. 110–127, 1933. [Gen. Rel. Grav.41,207(2009)].
- [6] E. Komatsu *et al.*, “Seven-year wilkinson microwave anisotropy probe (wmap) observations: Cosmological interpretation,” *The Astrophysical Journal Supplement Series*, vol. 192, no. 2, p. 18, 2011.
- [7] P. A. R. Ade *et al.*, “Planck 2015 results. XIII. Cosmological parameters,” *Astron. Astrophys.*, vol. 594, p. A13, 2016.
- [8] E. Wigner, “On unitary representations of the inhomogeneous lorentz group,” *Annals of Mathematics*, vol. 40, no. 1, pp. 149–204, 1939.
- [9] The ATLAS Collaboration, “Observation of a new particle in the search for the standard model higgs boson with the atlas detector at the lhc,” *Physics Letters B*, vol. 716, no. 1, pp. 1 – 29, 2012.
- [10] The CMS Collaboration, “Observation of a new boson at a mass of 125 gev with the cms experiment at the lhc,” *Physics Letters B*, vol. 716, no. 1, pp. 30 – 61, 2012.
- [11] P. W. Higgs, “Broken symmetries and the masses of gauge bosons,” *Phys. Rev. Lett.*, vol. 13, pp. 508–509, Oct 1964.
- [12] M. Krammer, “The update of the european strategy for particle physics,” *Physica Scripta*, vol. 2013, no. T158, p. 014019, 2013.

-
- [13] A. Arbey *et al.*, “Physics at the e^+e^- Linear Collider,” *Eur. Phys. J.*, vol. C75, no. 8, p. 371, 2015.
- [14] C. Adloff *et al.*, “Calorimetry for Lepton Collider Experiments - CALICE results and activities,” 2012.
- [15] H. Abramowicz *et al.*, “The International Linear Collider Technical Design Report - Volume 4: Detectors,” 2013.
- [16] D. Brandt, H. Burkhardt, M. Lamont, S. Myers, and J. Wenninger, “Accelerator physics at lep,” *Reports on Progress in Physics*, vol. 63, no. 6, p. 939, 2000.
- [17] J. Goldstone, A. Salam, and S. Weinberg, “Broken Symmetries,” *Phys. Rev.*, vol. 127, pp. 965–970, 1962.
- [18] H. Yukawa, “On the Interaction of Elementary Particles I,” *Proc. Phys. Math. Soc. Jap.*, vol. 17, pp. 48–57, 1935. [Prog. Theor. Phys. Suppl.1,1(1935)].
- [19] J. Tian and K. Fujii, “Measurement of Higgs couplings and self-coupling at the ILC,” *PoS*, vol. EPS-HEP2013, p. 316, 2013.
- [20] D. M. Asner *et al.*, “ILC Higgs White Paper,” in *Proceedings, Community Summer Study 2013: Snowmass on the Mississippi (CSS2013): Minneapolis, MN, USA, July 29-August 6, 2013*, 2013.
- [21] “Projected Performance of an Upgraded CMS Detector at the LHC and HL-LHC: Contribution to the Snowmass Process,” in *Proceedings, Community Summer Study 2013: Snowmass on the Mississippi (CSS2013): Minneapolis, MN, USA, July 29-August 6, 2013*, 2013.
- [22] K. Fujii *et al.*, “Physics Case for the International Linear Collider,” 2015.
- [23] K. A. Olive *et al.*, “Review of Particle Physics,” *Chin. Phys.*, vol. C38, p. 090001, 2014.
- [24] O. Hahn, “Über ein neues radioaktives zerfallsprodukt im uran,” *Naturwissenschaften*, vol. 9, no. 5, pp. 84–84, 1921.
- [25] N. Feege, *Low-Energetic Hadron Interactions in a Highly Granular Calorimeter*. PhD thesis, Universität Hamburg, 2011.
- [26] R. Wigmans, *Calorimetry in High Energy Physics*, pp. 325–379. Boston, MA: Springer US, 1991.
- [27] L. S. Waters, “Summary of the 2006 hadronic shower simulation workshop,” *AIP Conference Proceedings*, vol. 896, no. 1, pp. 235–249, 2007.

- [28] J. D. Jackson, R. G. Barton, R. Donaldson, and D. K. Savage, “Conceptual Design of the Superconducting Super Collider,” 1986.
- [29] R. Desalvo, F. Hartjes, A. Henriques, B. Ong, H. Paar, C. Scheel, P. Sonderegger, R. Wigmans, and A. Zichichi, “A novel way of electron identification in calorimeters,” *Nuclear Instruments and Methods in Physics Research Section A: Accelerators, Spectrometers, Detectors and Associated Equipment*, vol. 279, no. 3, pp. 467 – 472, 1989.
- [30] A. Caldwell, L. Hervs, J. Parsons, F. Sciulli, W. Sippach, and L. Wai, “Measurement of the time development of particle showers in a uranium scintillator calorimeter,” *Nuclear Instruments and Methods in Physics Research Section A: Accelerators, Spectrometers, Detectors and Associated Equipment*, vol. 330, no. 3, pp. 389 – 404, 1993.
- [31] F. Simon, C. Soldner, and L. Weuste, “T3b an experiment to measure the time structure of hadronic showers,” *Journal of Instrumentation*, vol. 8, no. 12, p. P12001, 2013.
- [32] C. Soldner, *The time development of hadronic showers and the T3B experiment*. PhD thesis, Munich U., 2013.
- [33] F. Simon and the CALICE Collaboration, “Particle showers in a highly granular hadron calorimeter,” *Journal of Physics: Conference Series*, vol. 293, no. 1, p. 012073, 2011.
- [34] S. Chatrchyan *et al.*, “The CMS experiment at the CERN LHC,” *JINST*, vol. 3, p. S08004, 2008.
- [35] J. Ocariz, “The NA48 liquid krypton calorimeter description and performances,” 1999.
- [36] A. Peryshkin and R. Raja, “On sampling fractions and electron shower shapes,” 2011.
- [37] M. Derrick, D. Gacek, N. Hill, B. Musgrave, R. Noland, E. Petereit, J. Repond, R. Stanek, and K. Sugano, “Design and construction of the ZEUS barrel calorimeter.,” *Nucl. Instrum. Meth.*, vol. A309, pp. 77–100, 1991.
- [38] T. Gys, “Micro-channel plates and vacuum detectors,” *Nuclear Instruments and Methods in Physics Research Section A: Accelerators, Spectrometers, Detectors and Associated Equipment*, vol. 787, pp. 254 – 260, 2015. New Developments in Photodetection NDIP14.
- [39] P. Buzhan *et al.*, “An advanced study of silicon photomultiplier,” *ICFA Instrum. Bull.*, vol. 23, pp. 28–41, 2001.
- [40] D. Renker and E. Lorenz, “Advances in solid state photon detectors,” *Journal of Instrumentation*, vol. 4, no. 04, p. P04004, 2009.
- [41] T. Frster, “Zwischenmolekulare energiewanderung und fluoreszenz,” *Annalen der Physik*, vol. 437, no. 1-2, pp. 55–75, 1948.

- [42] R. WORLD, “P-I-N diode vs Schottky Barrier Photodiode vs Avalanche Photodiode-Difference between P-I-N diode,Schottky Barrier Photodiode,Avalanche Photodiode.” <http://www.rfwireless-world.com/Terminology/P-I-N-diode-vs-Schottky-Barrier-Photodiode-vs-Avalanche-Photodiode.html>, 2015. Visited January 2018.
- [43] F. Zappa, A. Lacaita, S. Cova, and P. Lovati, “Solid-state single-photon detectors,” *Optical Engineering*, vol. 35, pp. 938–945, 1996.
- [44] M. Stipčević, “Active quenching circuit for single-photon detection with geiger mode avalanche photodiodes,” *Appl. Opt.*, vol. 48, pp. 1705–1714, Mar 2009.
- [45] W. H. Geiger, “Das Elektronenrohr,” 1928.
- [46] C. Xu, “Study of the silicon photomultipliers and their applications in positron emission tomography,” 2014.
- [47] T. Price, P. Roloff, J. Strube, and T. Tanabe, “Full simulation study of the top yukawa coupling at the ilc at 1 tev,” *The European Physical Journal C*, vol. 75, no. 7, p. 309, 2015.
- [48] N. Akchurin, K. Carrell, J. Hauptman, H. Kim, H. Paar, A. Penzo, R. Thomas, and R. Wigmans, “Hadron and jet detection with a dual-readout calorimeter,” *Nuclear Instruments and Methods in Physics Research Section A: Accelerators, Spectrometers, Detectors and Associated Equipment*, vol. 537, no. 3, pp. 537 – 561, 2005.
- [49] R. Asfandiyarov, “A totally active scintillator calorimeter for the muon ionization cooling experiment (mice). design and construction,” *Nuclear Instruments and Methods in Physics Research Section A: Accelerators, Spectrometers, Detectors and Associated Equipment*, vol. 732, pp. 451 – 456, 2013. Vienna Conference on Instrumentation 2013.
- [50] M. Thomson, “Particle flow calorimetry and the pandorapfa algorithm,” *Nuclear Instruments and Methods in Physics Research Section A: Accelerators, Spectrometers, Detectors and Associated Equipment*, vol. 611, no. 1, pp. 25 – 40, 2009.
- [51] M. A. Thomson, “Particle flow calorimetry at the international linear collider,” *Pramana*, vol. 69, no. 6, pp. 1101–1107, 2007.
- [52] The ALEPH Collaboration, “Performance of the aleph detector at lep,” *Nuclear Instruments and Methods in Physics Research Section A: Accelerators, Spectrometers, Detectors and Associated Equipment*, vol. 360, no. 3, pp. 481 – 506, 1995.
- [53] “Particle-Flow Event Reconstruction in CMS and Performance for Jets, Taus, and MET,” 2009.

- [54] Christine Hu-Guo on behalf of the IPHC and IRFU Collaboration, “Development of Fast and High Precision CMOS Pixel Sensors for an ILC Vertex Detector,” *Arxiv preprint hep-th*, 2010.
- [55] P. Schade and J. Kaminski, “A large {TPC} prototype for a linear collider detector,” *Nuclear Instruments and Methods in Physics Research Section A: Accelerators, Spectrometers, Detectors and Associated Equipment*, vol. 628, no. 1, pp. 128 – 132, 2011. {VCI} 2010Proceedings of the 12th International Vienna Conference on Instrumentation.
- [56] J. Alme *et al.*, “The alice tpc, a large 3-dimensional tracking device with fast readout for ultra-high multiplicity events,” *Nuclear Instruments and Methods in Physics Research Section A: Accelerators, Spectrometers, Detectors and Associated Equipment*, vol. 622, no. 1, pp. 316 – 367, 2010.
- [57] Abe, Toshinori and others, “The International Large Detector: Letter of Intent,” 2010.
- [58] Tomita, Tatsuhiko and others, “A study of silicon sensor for ILD ECAL,” in *International Workshop on Future Linear Colliders (LCWS13) Tokyo, Japan, November 11-15, 2013*, 2014.
- [59] K. Kotera, “Scintillator Strip ECAL Optimization,” in *International Workshop on Future Linear Colliders (LCWS13) Tokyo, Japan, November 11-15, 2013*, 2014.
- [60] F. Kircher, U. Schneekloth et al., “Conceptual Design of the ILD Detector Magnet System,” 2012.
- [61] Steve Green Cambridge presentation for CLIC workshop, “HCal Simulation Studies.” https://indico.cern.ch/event/336335/session/1/contribution/179/attachments/657796/904374/CLIC_Workshop_28_1_15.pdf, 2015. Visited January 2016.
- [62] The CALICE Collaboration, “Construction and commissioning of the calice analog hadron calorimeter prototype,” *Journal of Instrumentation*, vol. 5, no. 05, p. P05004, 2010.
- [63] S. Conforti Di Lorenzo, S. Callier, J. Fleury, F. Dulucq, C. De la Taille, G. M. Chassard, L. Raux, and N. Seguin-Moreau, “SPIROC: Design and performances of a dedicated very front-end electronics for an ILC Analog Hadronic CALorimeter (AHCAL) prototype with SiPM read-out,” *JINST*, vol. 8, p. C01027, 2013.
- [64] B. Hermberg, *Measuring Hadronic Jets at the ILC - From Particle Flow Calorimetry to the Higgs Self-Coupling - DESY-THESIS-2015-039*. PhD thesis, Universitaet Hamburg, September 2015.

- [65] P. Horowitz and W. Hill, *The art of electronics*. Cambridge, Eng., New York: Cambridge University Press, 1980. Includes index.
- [66] P. W. Nicholson, *Nuclear Electronics*. New York, John Wiley and Sons, 1974.
- [67] C. Neubueser, “Comparison of Energy Reconstruction Schemes and Different Granularities in the CALICE AHCAL,” 2016.
- [68] F. Sefkow and A. Lucaci-Timoce, “Monte Carlo Studies of the CALICE AHCAL Tiles Gaps and Non-uniformities,” in *International Linear Collider Workshop (LCWS10 and ILC10) Beijing, China, March 26-30, 2010*, 2010.
- [69] Eljen Technology, *EJ-200 General Purpose Scintillator*. Similar to BC-408.
- [70] K. Briggel, M. Dorn, R. Hagdorn, T. Harion, H. C. Schultz-Coulon, and W. Shen, “Klaus: an ASIC for silicon photomultiplier readout and its application in a setup for production testing of scintillating tiles,” *Journal of Instrumentation*, vol. 9, no. 02, p. C02013, 2014.
- [71] V. Chmill, E. Garutti, R. Klanner, M. Nitschke, and J. Schwandt, “On the characterization of SiPMs from pulse-height spectra,” 2016.
- [72] F. Simon and C. Soldner, “Uniformity studies of scintillator tiles directly coupled to SiPMs for imaging calorimetry,” *Nuclear Instruments and Methods in Physics Research Section A: Accelerators, Spectrometers, Detectors and Associated Equipment*, vol. 620, no. 23, pp. 196 – 201, 2010.
- [73] A. Roy, “Instrumentation for studying real-time popcorn effect in surface mount packages during solder reflow,” *International Journal of Electrical, Computer, Energetic, Electronic and Communication Engineering*, vol. 7, no. 8, pp. 162 – 166, 2013.
- [74] P. L. Reeder, D. L. Stephens, D. V. Jordan, R. A. Craig, and B. D. Geelhood, “Progress report for the advanced large-area plastic scintillator (alps) project: Fy 2003 final,” *INIS*, vol. 36, 2003.
- [75] A. Dyshkant, D. Beznosko, G. Blazey, D. Chakraborty, K. Francis, D. Kubik, J. G. Lima, M. I. Martin, J. McCormick, V. Rykalin, and V. Zutshi, “Small scintillating cells as the active elements in a digital hadron calorimeter for the $e + e$ linear collider detector,” *Journal of Physics G: Nuclear and Particle Physics*, vol. 30, no. 9, p. N1, 2004.
- [76] Jaroslav Zalesak for the CALICE Collaboration, “Calibration issues for the calice 1m3 ahal.” arXiv:1201.6155, 2012.
- [77] S. Vinogradov, “Analytical models of probability distribution and excess noise factor of solid state photomultiplier signals with crosstalk,” *Nuclear Instruments and Methods*

- in Physics Research Section A: Accelerators, Spectrometers, Detectors and Associated Equipment*, vol. 695, pp. 247 – 251, 2012. New Developments in Photodetection NDIP11.
- [78] Markin, Oleg, “Backgrounds at future linear colliders.” arXiv:1402.2515, 2014.
- [79] Adrian Vogel, “Background Simulations for the International Linear Collider.” <http://www-flc.desy.de/lcnotes/notes/LC-DET-2007-012.pdf>, 2007.
- [80] J. Marshall, A. Muennich, and M. Thomson, “Performance of particle flow calorimetry at clic,” *Nuclear Instruments and Methods in Physics Research Section A: Accelerators, Spectrometers, Detectors and Associated Equipment*, vol. 700, pp. 153 – 162, 2013.
- [81] The CALICE Collaboration, “The time structure of hadronic showers in highly granular calorimeters with tungsten and steel absorbers,” *Journal of Instrumentation*, vol. 9, no. 07, p. P07022, 2014.
- [82] B. Hermsberg, “Commissioning of the Testbeam Prototype of the CALICE Tile Hadron Calorimeter,” in *Proceedings, 2012 IEEE Nuclear Science Symposium and Medical Imaging Conference (NSS/MIC 2012): Anaheim, California, USA, October 29-November 3, 2012*, pp. 1180–1191, 2012.
- [83] B. Bilki, J. Butler, T. Cundiff, G. Drake, W. Haberichter, E. Hazen, J. Hoff, S. Holm, A. Kreps, E. May, G. Mavromanolakis, E. Norbeck, D. Northacker, Y. Onel, J. Repond, D. Underwood, S. Wu, and L. Xia, “Calibration of a digital hadron calorimeter with muons,” *Journal of Instrumentation*, vol. 3, no. 05, p. P05001, 2008.
- [84] F. Simon and the CALICE Collaboration, “Studies of scintillator tiles with sipm readout for imaging calorimeters,” *Journal of Physics: Conference Series*, vol. 293, no. 1, p. 012074, 2011.
- [85] M. Danilov, “Scintillator tile-SiPM system development for CALICE Engineering AH-CAL Prototype,” in *International Workshop on Future Linear Colliders (LCWS10) Beijing, China, 2010*, 2010.
- [86] O. Hartbrich, *Commissioning and LED System Tests of the Engineering Prototype of the Analog Hadronic Calorimeter of the CALICE Collaboration - DESY-THESIS-2012-040*. PhD thesis, Universitaet Wuppertal, September 2012.
- [87] Stephane Callier OMEGA IN2P3-CNRS, “SPIROC2E and SKIROC2A.” https://agenda.linearcollider.org/event/7304/contributions/37375/attachments/30485/45590/SC_Calice_meeting_20160912.pptx, 2016.
- [88] M. Ramilli, “Towards hadronic shower timing with CALICE ANALOG Hadron Calorimeter,” in *Proceedings, International Conference on Calorimetry for the High Energy Frontier (CHEF 2013): Paris, France, April 22-25, 2013*, pp. 152–158, 2013.

-
- [89] Experimental Areas Group SL Division, “Beam Line H8 User Manual.” <http://nahandbook.web.cern.ch/nahandbook/default/h8/H8usermanual.pdf>, 2015. Visited October 2016.
- [90] V. A. Mitsou, “The ATLAS transition radiation tracker,” in *Astroparticle, particle and space physics, detectors and medical physics applications. Proceedings, 8th Conference, ICATPP 2003, Como, Italy, October 6-10, 2003*, pp. 497–501, 2003.
- [91] J. Repond, “Resistive Plate Chambers for Imaging Calorimetry - the DHCAL,” *JINST*, vol. 9, no. 09, p. C09034, 2014.
- [92] B. Bilki, “The CALICE digital hadron calorimeter: calibration and response to pions and positrons,” 2014. [J. Phys. Conf. Ser.587,no.1,012038(2015)].
- [93] T. Behnke and F. Gaede, “Software for the International Linear Collider: Simulation and reconstruction frameworks,” *Pramana*, vol. 69, pp. 1089–1092, 2007.
- [94] C. Guenter, *Comparison of Iron and Tungsten Absorber Structures for an Analog Hadron Calorimeter*. Dr., Universitt Hamburg, Hamburg, 2015. Universitt Hamburg, Diss., 2015.
- [95] M. Ramilli, “Towards hadronic shower timing with CALICE ANALOG Hadron Calorimeter,” in *Proceedings, International Conference on Calorimetry for the High Energy Frontier (CHEF 2013): Paris, France, April 22-25, 2013*, pp. 152–158, 2013.

Acknowledgments

Over the course of the time I spend at the University of Hamburg and DESY I met a lot of wonderful and amazing people. So many people had a positive impact on my life and despite all odds told me to carry on and finish this thesis. This list is for the people that touched me in my life and stuck along for the way. It will and can never be complete.

Valerie for the beautiful time together and the love and passion. Thank you for never giving up and always believing in me. I am so sorry.

Kelly for pushing me always to carry on, and being a great friend although she has still no idea why she does put up with it. Since she deserves to be mentioned here a lot of times: Kelly, Kelly, Kelly.....

Adriana for borrowing me her English language skills for corrections and of course her cat Jack to cuddle in times of need.

Jack for showing me the importance of locking your keyboard on the warm laptop when you are gone for a few seconds.

Black and White for being there when I felt alone. May you rest in peace overlooking the Elbe.

My mother although, she did put me into this horrible world. (I forgive you)

Michael, Milan, Marco, Matteo, Peter, Herr Klanner, and the whole world of building 67b, as well as the whole FLC group and especially Oskar and Katja for all the support and freedom at work. To all of you: I have never met people that dedicated and passionate about their work. I know I will never be able to live up to it but you will always be there as a shining example.

Last not least Erika for her undying patience. Thank you for putting up with me all of this time and (almost) trusting me not to burn down your lab.

And some honorable mentions: The people of Hamburg. To summarize, I finally found home. The Arbeitsamt for enabling me to continue working in peace on this thesis.

Whoever invented sailing thousands of years ago, you gave me meaning in life.

And thanks for all the fish.